Modelling the Slip Effect in High-Speed Centrifugal Compressors

A Comparison Between Reduced-Order Models and CFD

A. Dardor

Technische Universiteit Delft

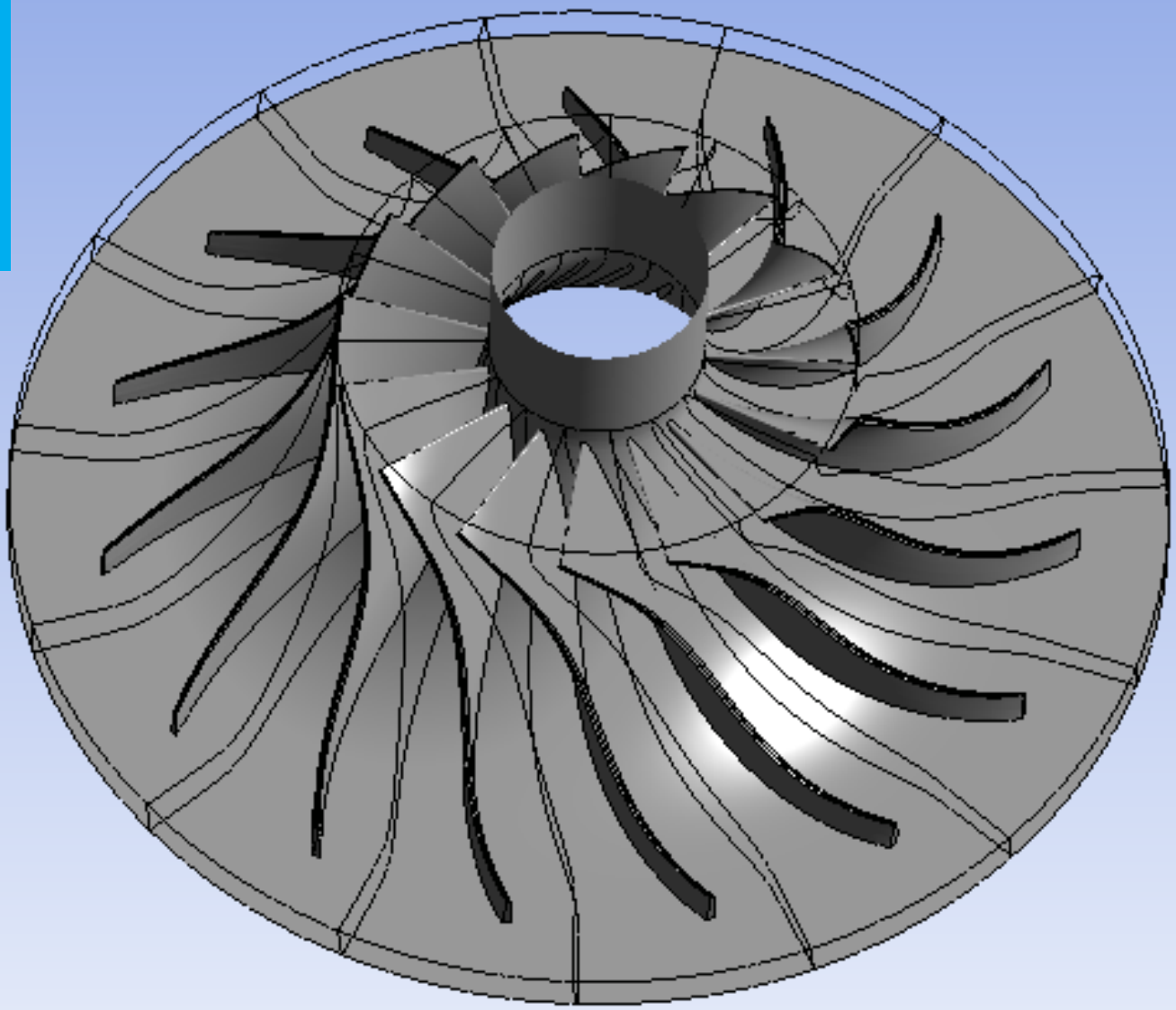

TU Delft Delft University of Technology

Challenge the future

Modelling the Slip Effect in High-Speed Centrifugal Compressors

A Comparison Between Reduced-Order Models and CFD

by

A. Dardor

in partial fulfillment of the requirements for the degree of

Master of Science
in Aerospace Engineering

at the Delft University of Technology,
to be defended publicly on Monday August 28, 2023 at 14:30.

Supervisors:	Dr. M. Pini	Power & Propulsion
	Ir. A. Giuffré	Power & Propulsion
Thesis committee:	Prof. P. Colonna	Chair - Power & Propulsion
	Dr. M. Pini	Supervisor - Power & Propulsion
	Dr. A.H. van Zuijlen	Examiner - Aerodynamics
	Ir. A. Giuffré	Supervisor - Power & Propulsion

The cover image is a render of the Radiver compressor [1][2][3].

An electronic version of this thesis is available at http://repository.tudelft.nl/.

TU Delft Delft University of Technology

Acknowledgments

This has been the most challenging undertaking of my life, and I would never have completed my work without the support of many family, friends, and colleagues.

First, I'd like to thank my supervisors, Dr Matteo Pini and Ir Andrea Giuffré, for their tremendous support and guidance throughout what turned out to be a more complicated project than we expected. Both of them did their utmost to guide me without ever giving me the solutions outright, which meant I could learn and grow more during this project than in any other period of my life. Furthermore, much of the work done in this thesis is based directly on their previous and ongoing work in the field of compressor design; I owe them a lot.

Of course, I would not be at TU Delft if not for my family. My parents, who have always pushed me and my siblings to be the best versions of ourselves and have done the impossible to support us both emotionally and financially. My brother, Ehab, always the model eldest brother that we all count on. And my sister, Dareen, the smartest engineer I know and my inspiration to continue into higher education. Also, a special thank you to my brother-in-law, Elias, for proofreading this report.

Finally, and most importantly, I must thank my amazing fiancée, Alaa, my biggest supporter and motivator and the most patient person in the world with me and my antics. This is for you, for both of us.

A. Dardor
Delft, July 2023

Abstract

This project falls under the overarching goal of developing next-generation environmental control systems for aircraft using electrically powered vapour compression cycles, a core research topic for the Power & Propulsion group. One of the most critical components of such systems is the high-speed centrifugal compressor. To that end, an in-house reduced-order model was developed to optimise the design process. Unsurprisingly, it was found that different slip factor models affected the resulting pressure ratio predictions. Thus, this study aims to investigate the effect of slip on centrifugal compressor performance and determine the most accurate method for estimating slip during the preliminary design stage.

To accomplish this task, the reduced-order model was tested with three established slip factor models: Wiesner, von Backstrom, and Qiu. The results of these tests were compared to data obtained from published experiments and computational fluid dynamics simulations conducted during this project. Two main test cases were chosen for this study: the TU Delft IRIS compressor and the Radiver compressor, openly released by researchers at RWTH Aachen University. High-resolution CFD simulations using Ansys CFX were conducted on both compressors. Further reduced-order model validation was performed on the EPFL Schiffmann compressor and the Eckardt series of compressors.

The Qiu model proved to be the most accurate slip factor model, among those tested, for almost all test cases. This is noted especially for high-speed compressors such as the IRIS compressor, which runs at speeds of 68-95 krpm. The Qiu model achieved an average error percentage of 2% when tested on the Radiver and IRIS compressors. In contrast, the Wiesner and von Backstrom models exhibited average errors of 10% and 5%, respectively. This high accuracy shown by the Qiu model is attributed to its second "turning" term. This term allows the model to adapt to changing flow conditions, unlike the other models, which are constant at all conditions and strictly geometry-dependent. The second important finding of this study is the comparison between the reduced-order model and CFD simulations. For the Radiver compressor, the reduced-order model using the Qiu slip factor model achieved an average error of 3%. For the same machine, CFD simulations exhibited a larger error of 8%. Accordingly, it is proven that the reduced-order model using the Qiu model is the most accurate method for slip factor estimation in the preliminary design phase compared to CFD simulations.

Contents

List of Figures iv

List of Tables viii

Glossary ix

1 Introduction 1
- 1.1 Project Context . . . 1
- 1.2 The Slip Effect . . . 2
- 1.3 Research Questions . . . 4
  - 1.3.1 The Slip Factor Discrepancy . . . 4
  - 1.3.2 Accurate Slip Factor Prediction . . . 4
- 1.4 Original Contribution . . . 4
- 1.5 Adopted Methodology . . . 5
- 1.6 Report Structure . . . 5

2 Literature Review 6
- 2.1 High-Speed Centrifugal Compressors . . . 6
- 2.2 The IRIS Compressor . . . 6
- 2.3 The Reduced-Order Model . . . 7
- 2.4 Slip Factor Models . . . 7
- 2.5 An Updated Slip Factor Model . . . 8
  - 2.5.1 The Radial Term . . . 8
  - 2.5.2 The Turning Term . . . 8
- 2.6 The Impact of Slip Factor on Compressor Performance . . . 9
- 2.7 The Slip Factor in CFD Simulations . . . 10
- 2.8 Summary . . . 11

3 Methodology 12
- 3.1 Reduced-Order Model . . . 12
  - 3.1.1 ROM Overview . . . 12
  - 3.1.2 Implementing the Qiu Model . . . 15
- 3.2 CFD Simulations . . . 16
  - 3.2.1 Compressor Geometries . . . 17
  - 3.2.2 Mesh Generation . . . 19
  - 3.2.3 Simulation Setups . . . 20

4 Results 23
- 4.1 ROM Results . . . 23
- 4.2 CFD Simulation Results . . . 28

5 Conclusions 34

6 Recommendations 35

Bibliography 36

A TurboSim Code Extract 38

B CFD Parametrisation 39

C Additional Results 40
- C.1 ROM Results . . . 40
- C.2 Slip Model Comparisons . . . 46
- C.3 CFD Simulation Results . . . 49

List of Figures

1.1 A flowchart of an aircraft ECS running on a Vapour Compression Cycle. [4] 1
1.2 A simplified Process & Instrumentation Diagram (PID) of the IRIS setup. [8] 2
1.3 An isometric view of the IRIS setup render. [8] 3
1.4 A diagram of the exit velocity triangles for a centrifugal compressor showing the slip effect. 3

2.1 Impeller diagrams according to their exit blade angles. Dotted lines represent the radial axis 9
2.2 Performance map of a compressor using experimental data, constant slip factor (Stanitz SFM), and variable slip factor. Sourced from: [20] 10
2.3 Postprocessing procedure for jet and wake slip factor evaluation. Adapted from: [22] . 10

3.1 Flowchart of the reduced-order model: design, off-design, and optimisation. ϵ refers to the tolerance prescribed in the algorithm. [5] 13
3.2 Compressor operating map as obtained from a ROM validation run. Compressor: Eckardt A, Slip Model: von Backstrom. Solid lines represent ROM predictions. Dashed lines and shaded regions represent ±5% uncertainty bands. Dots represent experimental data [24]. 14
3.3 Compressor operating maps obtained from the ROM for the in-house IRIS compressor using two slip models. Solid lines represent ROM predictions. Dashed lines and shaded regions represent ±5% uncertainty bands. Dots represent computational fluid dynamics data [10]. 15
3.4 Total-to-total isentropic efficiency of the IRIS compressor at the 85krpm speedline as obtained from the reduced-order model using the Wiesner slip model. Dashed lines and shaded regions represent ±5% uncertainty bands. Dots represent computational fluid dynamics data [10]. 15
3.5 Picture of the IRIS compressor geometry as it was generated in Ansys TurboGrid . . . 17
3.6 Ansys picture of the mesh used for the IRIS compressor. 18
3.7 Diagram of the MTU impeller geometry. Left: meridional view (X is axial length, R is radial). Right: three-dimensional view. [3] 18
3.8 Picture of the Radiver compressor geometry as it was generated in Ansys TurboGrid. . 19
3.9 Ansys picture of the mesh used for the Radiver compressor. 20

4.1 Operating map for the Radiver compressor from the reduced-order model. Dot markers represent experimental results [1]. Slip models: solid - Qiu, dashed - von Backstrom, dotted - Wiesner. 23
4.2 Operating map for the IRIS compressor from the reduced-order model. Dot markers represent CFD results [5]. Slip models: solid - Qiu, dashed - von Backstrom, dotted - Wiesner. 24
4.3 Slip factor estimations obtained from the reduced-order model. Slip models: solid - Qiu, dashed - von Backstrom, dotted - Wiesner. 25
4.4 Slip factor estimations for the Radiver and IRIS compressors obtained from the reduced-order model using the Qiu slip model. 25
4.5 Operating maps for the Radiver and IRIS compressors from the reduced-order model. Solid lines represent the reduced-order model predictions using the Qiu slip model. Dashed lines are ±5% uncertainty bands about the ROM predictions. 26
4.6 Total-to-total isentropic efficiency estimation for the Radiver compressor at 28 krpm obtained from the reduced-order model using the Qiu slip model. Dot markers represent experimental results [1] 26

4.7 Total-to-total isentropic efficiency estimates obtained from the reduced-order model for the IRIS compressor at 85krpm using two different slip models. Dot markers represent CFD results [5]. 27
4.8 Operating map for the Eckardt O and Schiffmann compressors from the reduced-order model. Solid lines represent the reduced-order model predictions using the Qiu slip model. Dashed lines are ±5% uncertainty bands about the ROM predictions. Dots represent experimental results. 27
4.9 Velocity streamlines through the blade passage of the Radiver compressor at 28,541 RPM and 1 kg/s. 28
4.10 Velocity streamlines through the blade passage of the IRIS compressor at 85,748 RPM and 0.114 kg/s. 28
4.11 Velocity contours at the impeller exit of the Radiver and IRIS compressors. Radiver conditions: 28,541 RPM and 1 kg/s. IRIS conditions: 85,748 RPM and 0.114 kg/s. . . . 29
4.12 Mach number distribution in the blade-to-blade plane at half-span for the Radiver compressor at 28,541 RPM and 1 kg/s. 29
4.13 Mach number distribution in the blade-to-blade plane at half-span for the IRIS compressor at 85,748 RPM and 0.114 kg/s. 30
4.14 Operating map for the Radiver compressor. Solid lines represent reduced-order model results. Square markers represent CFD results. Dot markers represent experimental results [1]. 30
4.15 A diagram of the exit velocity triangles for a centrifugal compressor showing the slip effect. 31
4.16 Impeller exit velocity diagram for the Radiver compressor at 28,541 RPM and 1 kg/s. . 32
4.17 Impeller exit velocity diagram for the IRIS compressor at 85,748 RPM and 0.114 kg/s. . 32
4.18 Slip factor estimations for the Radiver and IRIS compressors obtained from the reduced-order model using the Qiu slip model compared to CFD simulation results. 32
4.19 Total-to-total isentropic efficiency estimates for the Radiver compressor at 28krpm. Solid lines represent reduced-order model results. Square markers represent CFD results. Dot markers represent experimental results [1]. 33

B.1 Screenshot of the parameter view in Ansys Workbench used in this study. 39

C.1 Total-to-total isentropic efficiency estimates for the MTU compressor at 28krpm. The solid line represents reduced-order model results. Dot markers represent experimental results [1]. 40
C.2 Total-to-total isentropic efficiency estimates for the IRIS compressor at 68krpm. The solid line represents reduced-order model results. Dot markers represent CFD results [5]. 41
C.3 Total-to-total isentropic efficiency estimates for the IRIS compressor at 77krpm. The solid line represents reduced-order model results. Dot markers represent CFD results [5]. 41
C.4 Total-to-total isentropic efficiency estimates for the IRIS compressor at 85krpm. The solid line represents reduced-order model results. Dot markers represent CFD results [5]. 42
C.5 Total-to-total isentropic efficiency estimates for the IRIS compressor at 90krpm. The solid line represents reduced-order model results. Dot markers represent CFD results [5]. 42
C.6 Total-to-total isentropic efficiency estimates for the IRIS compressor at 94krpm. The solid line represents reduced-order model results. Dot markers represent CFD results [5]. 43
C.7 Operating map for the Radiver compressor. The solid line represents reduced-order model results. Dot markers represent experimental results [1]. 43
C.8 Operating map for the IRIS compressor. The solid line represents reduced-order model results. Dot markers represent CFD results [5]. 44
C.9 Operating map for the Eckardt A compressor. The solid line represents reduced-order model results. Dot markers represent Experimental results [24]. 44
C.10 Operating map for the Eckardt B compressor. The solid line represents reduced-order model results. Dot markers represent Experimental results [24]. 45
C.11 Operating map for the Eckardt O compressor. The solid line represents reduced-order model results. Dot markers represent Experimental results [24]. 45
C.12 Operating map for the Schiffmann compressor. The solid line represents reduced-order model results. Dot markers represent Experimental results [26]. 46

C.13 Operating map for the Radiver compressor. The solid line represents reduced-order model results. Dot markers represent experimental results [1]. Slip models: solid - Qiu, dashed - von Backstrom, dotted - Wiesner. 46
C.14 Operating map for the IRIS compressor. The solid line represents reduced-order model results. Dot markers represent CFD results [5]. Slip models: solid - Qiu, dashed - von Backstrom, dotted - Wiesner. 47
C.15 Operating map for the Eckardt A compressor. The solid line represents reduced-order model results. Dot markers represent Experimental results [24][25]. Slip models: solid - Qiu, dashed - von Backstrom, dotted - Wiesner. 47
C.16 Operating map for the Eckardt B compressor. The solid line represents reduced-order model results. Dot markers represent Experimental results [24][25]. Slip models: solid - Qiu, dashed - von Backstrom, dotted - Wiesner. 48
C.17 Operating map for the Eckardt O compressor. The solid line represents reduced-order model results. Dot markers represent Experimental results [24][25]. Slip models: solid - Qiu, dashed - von Backstrom, dotted - Wiesner. 48
C.18 Operating map for the Schiffmann compressor. The solid line represents reduced-order model results. Dot markers represent Experimental results [26]. Slip models: solid - Qiu, dashed - von Backstrom, dotted - Wiesner. 49
C.19 Operating map for the Radiver compressor. The solid line represents reduced-order model results. Dot markers represent experimental results [1]. Square markers represent CFD results. 49
C.20 Operating map for the Radiver compressor. The solid line represents reduced-order model results. Dot markers represent experimental results [1]. Square markers represent CFD results. 50
C.21 Velocity streamlines through the blade passage of the Radiver compressor at 21,406 RPM and 0.83 kg/s. 50
C.22 Velocity streamlines through the blade passage of the Radiver compressor at 24,973 RPM and 1.25 kg/s. 51
C.23 Velocity streamlines through the blade passage of the Radiver compressor at 28,541 RPM and 1 kg/s. 51
C.24 Velocity streamlines through the blade passage of the Radiver compressor at 32,108 RPM and 1.18 kg/s. 52
C.25 Velocity streamlines through the blade passage of the Radiver compressor at 35,676 RPM and 1.4 kg/s. 52
C.26 Velocity streamlines through the blade passage of the IRIS compressor at 68,598 RPM and 0.08 kg/s. 53
C.27 Velocity streamlines through the blade passage of the IRIS compressor at 77,173 RPM and 0.09 kg/s. 53
C.28 Velocity streamlines through the blade passage of the IRIS compressor at 85,748 RPM and 0.114 kg/s. 54
C.29 Velocity streamlines through the blade passage of the IRIS compressor at 90,035 RPM and 0.12 kg/s. 54
C.30 Velocity streamlines through the blade passage of the IRIS compressor at 94,323 RPM and 0.11 kg/s. 55
C.31 Velocity contours at the impeller exit of the Radiver compressor at 21,406 RPM and 0.83 kg/s. 55
C.32 Velocity contours at the impeller exit of the Radiver compressor at 24,973 RPM and 1.25 kg/s. 56
C.33 Velocity contours at the impeller exit of the Radiver compressor at 28,541 RPM and 1 kg/s. 56
C.34 Velocity contours at the impeller exit of the Radiver compressor at 32,108 RPM and 1.18 kg/s. 57
C.35 Velocity contours at the impeller exit of the Radiver compressor at 35,676 RPM and 1.4 kg/s. 57
C.36 Velocity contours at the impeller exit of the IRIS compressor at 68,598 RPM and 0.08 kg/s. 58

C.37 Velocity contours at the impeller exit of the IRIS compressor at 77,173 RPM and 0.09 kg/s. 58
C.38 Velocity contours at the impeller exit of the IRIS compressor at 85,748 RPM and 0.114 kg/s. 59
C.39 Velocity contours at the impeller exit of the IRIS compressor at 90,035 RPM and 0.12 kg/s. 59
C.40 Velocity contours at the impeller exit of the IRIS compressor at 94,323 RPM and 0.11 kg/s. 60
C.41 Mach number distribution in the blade-to-blade plane at half-span for the Radiver compressor at 21,406 RPM and 0.83 kg/s. 60
C.42 Mach number distribution in the blade-to-blade plane at half-span for the Radiver compressor at 24,973 RPM and 1.25 kg/s. 61
C.43 Mach number distribution in the blade-to-blade plane at half-span for the Radiver compressor at 28,541 RPM and 1 kg/s. 61
C.44 Mach number distribution in the blade-to-blade plane at half-span for the Radiver compressor at 32,108 RPM and 1.18 kg/s. 62
C.45 Mach number distribution in the blade-to-blade plane at half-span for the Radiver compressor at 35,676 RPM and 1.4 kg/s. 62
C.46 Mach number distribution in the blade-to-blade plane at half-span for the IRIS compressor at 68,598 RPM and 0.08 kg/s. 63
C.47 Mach number distribution in the blade-to-blade plane at half-span for the IRIS compressor at 77,173 RPM and 0.09 kg/s. 63
C.48 Mach number distribution in the blade-to-blade plane at half-span for the IRIS compressor at 85,748 RPM and 0.114 kg/s. 64
C.49 Mach number distribution in the blade-to-blade plane at half-span for the IRIS compressor at 90,035 RPM and 0.12 kg/s. 64
C.50 Mach number distribution in the blade-to-blade plane at half-span for the IRIS compressor at 94,323 RPM and 0.11 kg/s. 65

List of Tables

2.1 A table summarising the details of the most widely used slip factor models. 11

3.1 A table summarising the basic information of the two test cases used in the CFD analysis. 17
3.2 The mesh analysis limits maintained to ensure mesh quality. 20
3.3 The simulation conditions for the two test cases 21

4.1 A table summarising the average error percentages of each SFM for the Radiver and IRIS compressors. 24
4.2 A table collecting the formulas of the three slip factor models used in the reduced-order model. 25

Glossary

Nomenclature

σ Slip factor: a measure of the deviation between the mean flow angle and the blade metal angle. [-]

V Absolute fluid velocity. [m/s]

U Blade linear velocity. [m/s]

W Relative fluid velocity. [m/s]

β Relative flow angle: the angle between the relative fluid velocity W and the radial direction. [rad]

α Absolute flow angle: the angle between the absolute fluid velocity V and the radial direction. [rad]

Z Number of blades. [-]

s Blade spacing (or pitch): the distance between consecutive blades. [m]

c Blade chord length. [m]

$\frac{c}{s_2}$ Solidity: the ratio of blade chord length to spacing. [-]

F_v Solidity influence coefficient: a factor in the von Backstrom slip model that depends on the blade angle and solidity

F Shape factor: a factor in the Qiu slip model that depends on the compressor geometry. [-]

ϕ Flow coefficient: $\frac{V_m}{U}$ a nondimensional measure of the flow through a turbomachine. [-]

$\frac{d\beta}{dm}$ Blade turning rate: a derivative measuring the rate of change of the blade angle over meridional length. [rad/m]

t Blade thickness. [m]

ϕ_{t1} Swallowing capacity: a different non-dimensional measure of flow similar to ϕ. They are related by $\phi_{t1} = \frac{\rho_2}{\rho_{t1}}\phi_2$. [-]

ψ Work coefficient: a nondimensional measure of the work done in a turbomachine. [-]

γ_{Pv} Isentropic pressure-volume exponent: a measure of the fluid's departure from ideal gas behaviour. Equal to the ratio of specific heats. [-]

Re Reynolds number: the ratio between inertial and viscous forces in a flow. [-]

Subscripts

1 Value at the impeller inlet.

2 Value at the impeller exit / diffuser inlet.

t Tangential component of velocity. Also, the total quantity of temperature or pressure.

tt Total-to-Total: used in pressure ratio and efficiency values to signify the measurement between total quantities at inlet and outlet.

m Meridional component of velocity.

b Theoretical value (based on blade metal angle)

Acronyms

ECS Environmental Control System: the system that controls the air supply, temperature, and pressure of the aircraft cabin.

ACM Air Cycle Machines: a type of ECS that does not use a refrigerant but relies on bleed air from the aircraft engines.

VCC Vapour Compression Cycle: a cycle that includes a compressor, condenser, expansion valve, and evaporator. Used to remove heat from a space and reject it to a heat sink.

ROM Reduced-Order Model: a simplification of high-fidelity, complex models.

SFM Slip Factor Model: a model used to estimate the value of slip factor depending on other known quantities.

IRIS Inverse organic Rankine cycle Integrated System: a test setup at TU Delft made for the performance analysis and validation of VCC systems for aircraft ECS.

CFD Computational Fluid Dynamics: methods that use numerical analysis to analyse fluid flows. Generally used through computer software.

1

Introduction

This first chapter of this report will set up the background needed to contextualise the work done in this thesis project. First, we will explain how this project was envisioned and what made it a necessary exploration. Then, a brief explanation of the slip effect and its historical models will be presented. Finally, a more modern slip factor model will be described as a basis for much of this work.

1.1. Project Context

The Power & Propulsion group at TU Delft is investigating novel designs for aircraft Environment Control Systems (ECS). The ECS is responsible for 3-5% of the total fuel consumed by an aircraft, making it the leading consumer of non-propulsive power. To optimise the ECS, the aim is to replace the current Air Cycle Machines (ACM) technology with electrical Vapor Compression Cycle (VCC) systems, such as that shown in Figure 1.1. The main driving components determining the VCC performance are its heat exchangers and high-speed centrifugal compressors [4]. Thus, the development of highly efficient compressors becomes paramount.

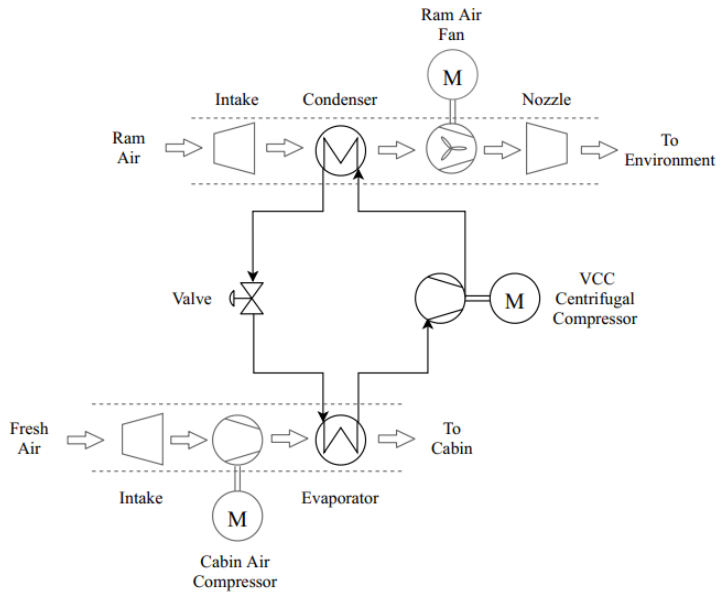

Figure 1.1: A flowchart of an aircraft ECS running on a Vapour Compression Cycle. [4]

A significant part of this development is the in-house compressor design software "TurboSim" and, more importantly, the reduced-order model it is built on. TurboSim is built on Python code that allows users to complete the preliminary design phase of centrifugal compressors[5]. During development, an

important question was raised: "What is the impact of slip factor models on the pressure ratio prediction of this reduced-order model?" Thus this project began to study the slip effect on multiple test cases and produce quantitative answers to the previous question. For clarity in the rest of this paper, TurboSim will be referred to as the Reduced-Order Model (ROM). Slip factor models, also considered reduced-order models, will be referred to exclusively as Slip Factor Models (SFMs).

Briefly, slip is an inviscid effect that occurs in compressors where the mean fluid flow does not follow the blade angle of the compressor, creating a slip angle between the two. This can significantly impact the velocity triangles at the impeller exit, directly influencing the pressure ratio. Due to the difficulty of calculating slip directly, SFMs have been developed that approximate its effect using a variety of other compressor parameters. The slip effect will be explained more thoroughly in Section 1.2.

The ROM this study is based on was created to achieve fast and accurate compressor designs according to the design requirements. A validation mode can be used to compare the ROM results with other sources, such as experiments and CFD simulations. This mode was the most important for this study and presented an ideal environment to test different SFMs on multiple test cases. Before the start of this project, the ROM used the slip factor models developed by Wiesner (1967) [6] and von Backstrom (2006) [7].

Also part of the investigation of novel ECS designs by the Power & Propulsion group is the Inverse organic Rankine cycle Integrated System (IRIS) [8]. This test rig is currently in development at TU Delft for performance analysis and validation of the VCC-based ECS that the P&P group is working towards. The process and instrumentation diagram is shown in Figure 1.2, and the isometric view is shown in Figure 1.3.

The IRIS test rig is relevant to our project due to the high-speed centrifugal compressor designed for use in this cycle, which will be referred to as the IRIS compressor. The final version of this compressor shown in 1.2 is a twin-stage machine, but a single-stage prototype of the same compressor will be considered in this study as one of our test cases.

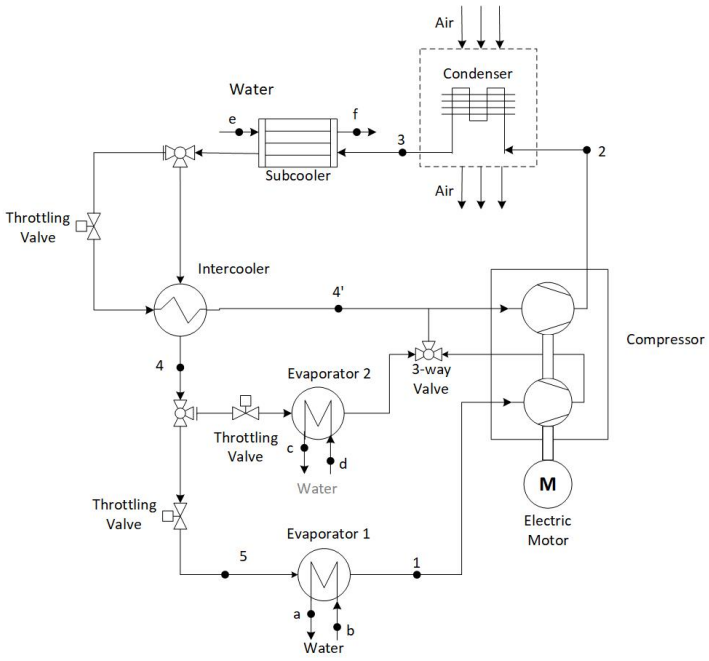

Figure 1.2: A simplified Process & Instrumentation Diagram (PID) of the IRIS setup. [8]

1.2. The Slip Effect

The slip effect is a phenomenon that occurs in all compressors, but it is much more pronounced in centrifugal compressors than in axial ones. Slip occurs when the mean fluid flow does not follow the blade direction causing a slip angle between the fluid flow and the metal blade. This causes a reduction in the compressor's pressure ratio, but it does not affect efficiency as it is an inviscid effect which

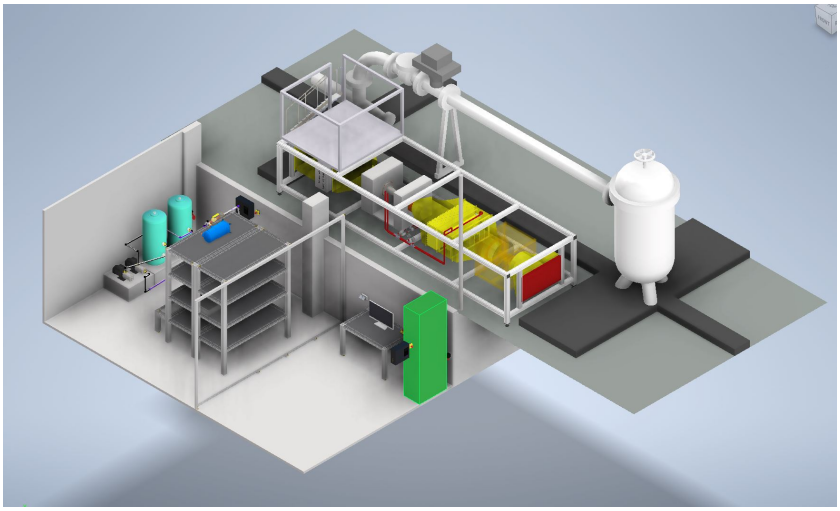

Figure 1.3: An isometric view of the IRIS setup render. [8]

does not result in higher losses. Figure 1.4 presents the velocity triangles at the exit of a centrifugal compressor which shows the slip effect. The velocity triangles are altered in this case. With this change in velocities, the work done by the compressor is lowered. This is why it is critical to account for slip in any centrifugal compressor design, as that allows for a more accurate prediction of actual compressor performance for the given boundary conditions. The basic formula for slip factor calculation using the velocity triangles is presented in Equation 1.1. However, since the actual V_2 is not known a priori, many different modelling approaches have been adopted to estimate the slip factor value. These will be explored further in Section 2.4.

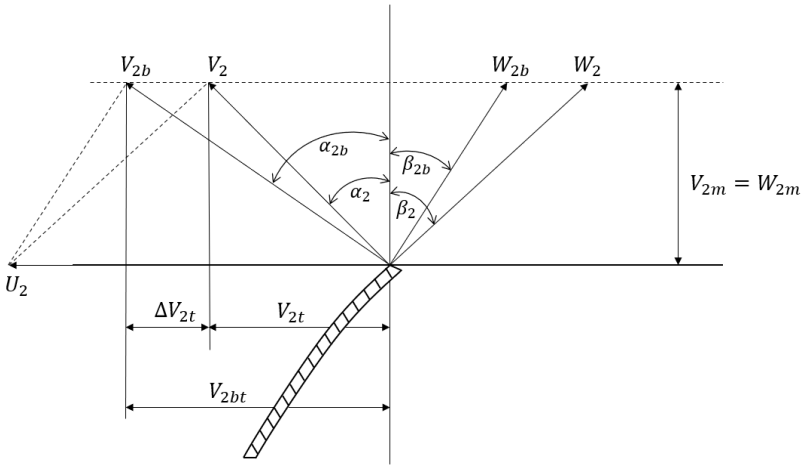

Figure 1.4: A diagram of the exit velocity triangles for a centrifugal compressor showing the slip effect.

$$\sigma = 1 - \frac{\Delta V_{2t}}{U_2} \tag{1.1}$$

Furthermore, it has been found that the error in slip prediction generally scales with the square of the compressor Mach number, making it harder to accurately predict pressure ratios for high-speed compressors [9].

This thesis is primarily concerned with modelling and accurately predicting slip factors such that designers may correct for its effect. The goal is to offer designers precise predictions of pressure ratio as early as possible in the design process. This is important because multiple iterations can

significantly increase the cost and time required, particularly when a specific pressure ratio is necessary. Consequently, improving the slip factor estimation in the ROM may save significant resources in the overall design process.

1.3. Research Questions

This project aims to answer the major questions from the preceding work explained in Section 1.1. These questions are presented as follows:

- What causes the slip factor discrepancy between the reduced-order model and CFD?
  - Which is the correct prediction, if any?
- What is the most accurate method to predict slip factor during the preliminary design process?

1.3.1. The Slip Factor Discrepancy

The first line of research lies in the discrepancy between the results of the ROM and CFD. There can be an underlying assumption of accuracy with CFD simulations, but that is not guaranteed. This brings forward the question of which of these predictions is accurate in the first place, as modifying the ROM to be more similar to the CFD results when they are inaccurate is a dead end. Thus, a three-pronged approach was adopted, using the ROM, CFD, and experimental results where available. Applying this approach to the case studies presented later in this thesis should lead to satisfactory answers to this first question.

However, that alone would not yield clear takeaways. Therefore, it is necessary to analyse the slip factor expressions to understand why the ROM may over or under-predict pressure ratios.

1.3.2. Accurate Slip Factor Prediction

The second consideration is to find an accurate method of predicting the slip factor during the preliminary design phase. Obtaining sufficiently accurate predictions early on dramatically increases the efficiency of the design process and helps reach the optimal design for a given application more reliably.

This can be achieved in several different ways. A new SFM could be used from published literature to bolster the accuracy of the ROM, a first-order model could be developed using empirical or CFD data, or an entirely new SFM should be developed. Of these, using an existing model is the most feasible.

1.4. Original Contribution

This study aims to provide several original contributions. This comes in three aspects:

- Studying high-speed centrifugal compressors and the effect of slip on them.
- Testing the in-house IRIS compressor, which has not yet been tested experimentally.
- Analysing CFD simulations and their reliability in predicting slip.

1.5. Adopted Methodology

After defining the research questions of this study, a plan is made to answer them. The first objective was to perform a literature review and study the history of slip factor models, up to the most modern ones. Thus, creating an overall picture of the general state of slip factor modelling as it currently stands. After this, a study of the current slip prediction methods implemented into the ROM was conducted to find its deficiencies. What follows is the development phase. Changes are to be made to the ROM to improve its capabilities for slip factor prediction.

Following this was the bulk of the work, the validation phase. For this part of the project, two test case compressors were chosen. The first is the well-documented Radiver test case [1]. This compressor uses air as its working fluid and is a good test case as its experimental performance results have been published and are readily available. The second case is the in-house IRIS compressor which uses the refrigerant R1233zd(E) [10]. There is no experimental data for this machine as of writing. The choice of these two test cases was well-informed as they each provide a different context that can help test the slip model predictions. They use different fluids, run at different rotational speeds, and have different ranges of mass flow and pressure ratios. This should allow ample testing opportunities for the presented SFMs.

Upon the completion of the validation phase, the analysis can begin. This analysis has two goals. Firstly, to study the different slip factor estimations used in the ROM and compare their results both to each other and to experimental data for several compressors. The CFD data, however, will be available for the two test cases and will be compared with the ROM results. This informs the analysis further and potentially allows for the modification or further development of the presented slip models. With this, the cause of the slip factor discrepancy would be found, and an accurate prediction can be made based on the available information, answering both of the research questions.

1.6. Report Structure

This thesis report will be divided into six main chapters, of which this introduction is the first. In this chapter, we have presented the context of the project, a brief overview of the slip effect (the main focus of this study), the research questions that underpin this project, the adopted methodology to answer the research questions, and finally, the original contributions that are made in this study. The second chapter will be a literature review of the most important publications that influenced this work, presenting a brief history of high-speed centrifugal compressors and the most common SFMs, followed by an overview of a more modern slip model that could be important for centrifugal compressors. Following that will be a chapter describing the methodology used to study the slip phenomenon in more depth divided into two main sections; the first describes the ROM and its working principles, and the second covers the process used for the CFD simulations discussing both the geometrical concerns and the simulation setups for both of the two test cases. The fourth chapter will cover the results and subsequent analysis based on those results. Again, it is split into two main sections, one dedicated to the ROM and the other to CFD. The final two chapters will present the conclusions and recommendations reached after the completion of this research study.

2

Literature Review

This chapter contains a review of previous work relevant to this study. This will be in 2 main directions, high-speed centrifugal compressors and slip factor models. High-speed centrifugal compressors are a unique subset of centrifugal compressors, so it is crucial to form a basis of knowledge for the rest of the study. SFMs, on the other hand, form the bulk of the work in this thesis, and the literature sources presented in this chapter were essential.

2.1. High-Speed Centrifugal Compressors

High-speed centrifugal compressors are characterised by speeds over 200 krpm. This has only become possible in recent years due to advancements in high-speed permanent magnetic, electric motors [11]. A compressor rotating at such speeds can replace a larger, slower compressor [12]. The size and weight reductions are one of the main goals of such compressors, along with gains in coefficient of performance. This can be inherently useful in applications such as aircraft Environmental Control Systems (ECS), where weight and size are crucial. Still, they can also be used in applications such as automobile turbochargers and industrial compressors. This smaller size can reduce the cost of manufacturing the machine and its supporting structures and positively affect the overall natural frequencies of the system. However, a balance must be found as smaller compressors can struggle with efficiency, pressure ratio requirements, and impeller material limitations [13]. Furthermore, relative quantities such as surface roughness and blade tip clearance are magnified due to the smaller size, enlarging friction and clearance losses, respectively [5]. Thus, a balance must be maintained to extract the best performance from high-speed centrifugal compressors.

This remains a nascent field that is actively being developed. Indeed, a paper published at TU Delft found relevant applications for high-speed centrifugal compressors using different refrigerants than the typical R134a implemented in a vapour compression cycle [14]. However, this was explicitly used in rotorcraft (i.e. helicopter) ECS. Thus, the current study explores high-speed compressors and the slip effect in such machines.

2.2. The IRIS Compressor

Developed at the Delft University of Technology, the Inverse Rankine Integrated System (IRIS) is a new experimental environment that can be used for different testing purposes, but the relevant part for this project is its intended use as a testbed for electrically powered Vapour Compression Cycles (VCC) for use in novel aircraft ECS [10]. Part of this experimental system is a miniature centrifugal high-speed compressor named the IRIS compressor. This compressor, designed at TU Delft, represents a significant part of this project. As described in Section 1.4, testing this compressor is a primary goal of this study. An important consideration is that the final design of the IRIS compressor is a twin-stage machine. However, initially, a single-stage compressor was designed. This will be used in this report as it simplifies the testing process and focuses the analysis on the slip factor specifically. To design this compressor, the ROM described in Section 2.3 was developed and validated [5].

2.3. The Reduced-Order Model

Section 3.1 describes the workflow details of this model. However, a general overview of this model will be presented here. This ROM was developed to use scaling principles and was made to suit high-speed centrifugal compressors with vaneless diffusers and arbitrary fluid choices. This widens the design space in the preliminary phase, which helps reach optimal solutions given the constraints of the design problem. For this to be feasible, compressor size and fluid thermodynamic behaviour must be considered as early as possible [5].

In the case of designing miniature high-speed centrifugal compressors, manufacturability constraints are a significant consideration. Due to the small size of these compressors, the machine tolerances during manufacturing become very tight and unforgiving. Another effect of this small scale is that relative values such as surface roughness and tip gap become even more important than they usually are, as their effects are magnified at such sizes. This ROM seeks to manage all these constraints while optimising the solution space.

The ROM was validated using experimental values from some well-documented centrifugal compressor test cases and CFD simulations conducted on the IRIS compressor described in Section 2.2. These validation studies produced promising results and showed good agreement with the experimental values. However, tying into the objectives of this current study, there were systematic discrepancies found that must be explored further and diagnosed.

2.4. Slip Factor Models

The phenomenon of slip occurring in turbomachinery has been discovered and studied extensively for almost a century. However, we cannot calculate slip using the formula in Equation 1.1, as that information is generally unavailable in the early stages of the compressor design process. So, models were defined to estimate the effect of slip, mainly felt through its lowering of the pressure ratio, reducing the work done by the machine. It is necessary to note that no single model makes all others obsolete. Brennen presents a brief history of the phenomenon [15]. He discusses the first published work that explores slip by Stodola in 1927 [16]. Stodola recognised that the flow through a rotating turbomachine can be split into two components, an irrotational and a rotational term. The rotational component has no through flow and consists exclusively of rotation within the blade passage. This rotational component proved crucial to the machine's pressure ratio and flow characteristics. The Stodola slip equation is presented in Equation 2.1. Busemann continued this work on what he called *"displacement flow"* [17] as he was the first to calculate its effect on flow characteristics for infinitely thin, logarithmic spiral blades. This assumption has proven significant in developing SFMs, as discussed in Section 2.5.2.

$$\sigma = 1 - \frac{2\pi \cos \beta_{2b}}{Zs} \tag{2.1}$$

The development of SFMs continued further with the work of Stanitz [18] (Equation 2.2) and then Wiesner [6] (Equation 2.3), who performed a review of many of the available slip factors at that time and presented a modified model that still sees extensive use today. In 2006, von Backstrom (Equation 2.4) presented a unified slip factor model that combines elements from many of the older models mentioned in this section [7]. The von Backstrom model is widely used and proved to be sufficiently reliable.

$$\sigma = 1 - \frac{0.63\pi}{Z} \tag{2.2}$$

$$\sigma = 1 - \frac{\sqrt{\cos \beta_{2b}}}{Z^{0.7}} \tag{2.3}$$

$$1 - \frac{1}{1 + F_v \left(\frac{c}{s_2}\right)} \tag{2.4}$$

As can be seen from the preceding equations, most SFMs are very similar. Nearly all are heavily dependent on the number of blades Z and the exit blade metal angle β_{2b}. So, the main components of

slip factor modelling are well considered. The differences then lie in the details between these models. But, as discussed in Section 2.5, some effects are not considered with these models.

Limitations of Common Slip Factor Models

An important consideration in terms of slip factor is that many of the most popular models are quite old but continue to be used extensively, including the Stodola (1927), Stanitz (1952), and Wiesner (1967) models. Where they may be perfectly usable for some compressors, they are unreliable for others, making it difficult to decide which model to use when designing a new compressor without prior knowledge of the accuracy of each SFM for that specific compressor architecture. Thus, a more recent model that may apply to a broader range of cases was explored.

2.5. An Updated Slip Factor Model

Qiu et al. present their new SFM, which can be considered a modification of Stodola's model [19]. This model aims to overcome the weaknesses of previous models, which mainly lie in their feasibility when applied to different impellers going so far as being applicable to centrifugal, axial, and mixed-flow impellers. In this thesis, we will only study centrifugal impellers. The equation for the Qiu SFM as it applies to centrifugal compressors is shown in Equation 2.5.

$$\sigma = 1 - \frac{F\pi \cos \beta_{2b}}{Z} - \frac{F s_2 \phi_2}{4 \cos \beta_{2b}} \left(\frac{d\beta}{dm} \right)_2 \tag{2.5}$$

Where F is the shape factor, β_{2b} is the exit blade metal angle, Z is the number of blades, s_2 is the pitch at blade exit, ϕ_2 is the exit flow coefficient, and $\left(\frac{d\beta}{dm}\right)_2$ is the exit blade turning rate.

The model consists of two main terms; The radial term and the turning term. The paper also presents a third term, but it was found not to have a significant effect and will be assumed zero in all the following analyses.

2.5.1. The Radial Term

The first term of the model is named the radial term and is shown in Equation 2.6.

$$\frac{F\pi \cos \beta_{2b}}{Z} \tag{2.6}$$

The radial term is the dominant and more conventional of the two. Excluding the shape factor F (setting it at 1), this resembles Stodola's slip factor model, which consisted of just one term. This term mainly covers the effects of the Coriolis force, which is considered a primary driver of the slip effect in centrifugal compressors. Adding the shape factor F helps account for Stodola's model underpredicting slip, as F is always less than one. Equation 2.7 presents the shape factor formula.

$$F = 1 - 2 \sin\left(\frac{\pi}{Z}\right) \sin\left(\frac{\pi}{Z} + \beta_{2b}\right) \cos\left(\beta_{2b}\right) - \frac{t_2}{s_2 \cos \beta_{2b}} \tag{2.7}$$

Where t_2 is the blade thickness at the trailing edge. All other terms are defined in Section 2.5.

The shape factor then depends on the compressor geometry, number of blades, blade metal angle, pitch, and thickness, all at the impeller exit.

2.5.2. The Turning Term

The second term is the turning term and is shown in Equation 2.8.

$$\frac{F s_2 \phi_2}{4 \cos \beta_{2b}} \left(\frac{d\beta}{dm} \right)_2 \tag{2.8}$$

This is the more novel term. It has less effect on the overall slip factor value but is essential in considering the impact of flow conditions and leading to more accurate predictions. The two main contributing parts of this term are the blade turning rate $\left(\frac{d\beta}{dm}\right)$ and the exit flow coefficient ϕ_2.

In their paper, Qiu et al. claim that a large proportion of the work done on SFMs was done on logarithmic spiral blade impellers, which have a zero blade-turning rate, as this is where Busemann began his work. Many authors since then have followed the same assumption (see Section 2.4). Consequently, this parameter and its effect on slip have not been explored enough. In essence, the blade turning rate measures the change in the blade angle β along the meridional length m. Thus, it is critical to note that the exit blade angle is separate from the turning rate. A compressor with a positive or negative exit blade angle can have a positive, negative, or zero blade-turning rate.

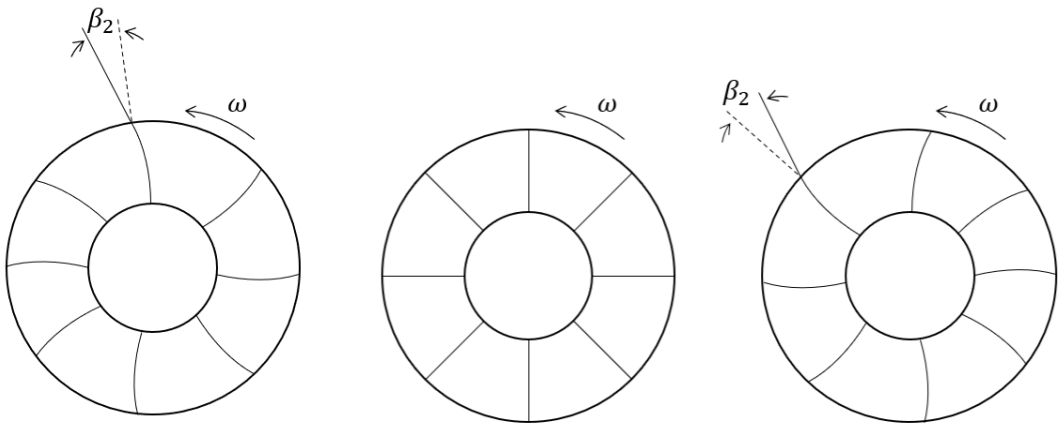

(a) Forward Sweep β_2 is positive. (b) Straight Radial β_2 is zero (c) Back Sweep β_2 is negative

Figure 2.1: Impeller diagrams according to their exit blade angles. Dotted lines represent the radial axis

To take the diagrams in Figure 2.1 as an example, the ”straight radial” impeller in 2.1b has both a zero exit blade angle and a zero blade turning rate because the blade angle is not changing as the meridional path approaches the impeller exit. On the other hand, the other two impellers in 2.1a and 2.1c have non-zero exit blade angles, but they may have zero blade turning rates if their angle is not changing. Finally, it is important to consider that the blade turning rate in the turning term is a derivative taken at the impeller exit. Thus, the blade turning rate may change along the meridional path, but the significant parameter for this formula is the rate at or near the impeller exit.

In addition to the turning rate, this term also considers the exit flow coefficient, a parameter seldom used in SFMs. Thus, most SFMs are constant with changing flow conditions which may be accurate in some cases but is not for many compressors, especially at higher rotation speeds. This gives the Qiu model a marked advantage as it adapts its prediction depending on flow rate and compressor rotational speed.

2.6. The Impact of Slip Factor on Compressor Performance

The slip effect is characterised by the amount of work done on the fluid flow being lowered because the mean flow at the impeller exit does not follow the blade trailing edge [7]. The specific work equation for centrifugal compressors is shown in Equation 2.9. Slip causes the velocities at exit (subscript 2) to be lower than their theoretical values, which lowers the amount of work the compressor does. Thus, reducing the achieved pressure ratio.

$$w = \frac{{V_2}^2 - {V_1}^2}{2} + \frac{{U_2}^2 - {U_1}^2}{2} - \frac{{W_2}^2 - {W_1}^2}{2} \tag{2.9}$$

During the preliminary design phase, the choice of slip factor model significantly impacts the predicted compressor performance [20]. Whitfield argues that a substantial part of this effect is due to flow rate variation. Many of the most prominent slip factor models were built around predicting design point performance. Off-design performance and the impact of flow conditions were rarely considered. In his work, Whitfield derives a ”jet slip factor” which can be used to modify the Stanitz SFM producing a slip factor that varies with flow rate, unlike the original Stanitz formula. Figure 2.2 shows the performance map of a compressor when using a constant slip factor compared to one that varies with flow rate. The choice of the slip factor model and the parameters considered in its calculation have a

tangible impact on the performance prediction. The effect of slip factor on compressor performance is extensively investigated in Chapter 4.

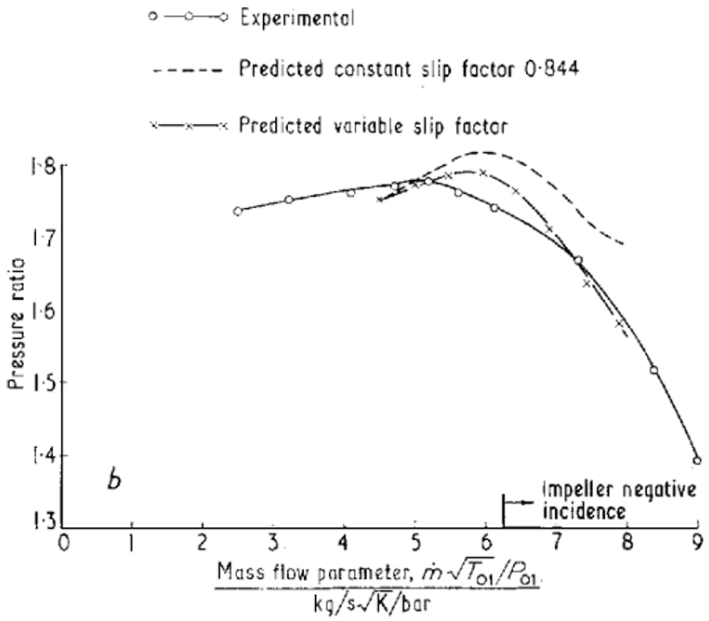

Figure 2.2: Performance map of a compressor using experimental data, constant slip factor (Stanitz SFM), and variable slip factor. Sourced from: [20]

2.7. The Slip Factor in CFD Simulations

Various studies have been conducted on slip factors in CFD. Waesker et al. performed an analysis of several SFMs using CFD simulations of 598 different centrifugal compressor impellers [21]. Of the models they tested, the Wiesner and Qiu SFMs were the closest matching to the CFD results. The methodology chosen for this study was to use low-fidelity simulations first. Then, high-fidelity runs could be initialised using the low-fidelity results. This was found to be faster and more robust than only using high-fidelity runs. The same method was employed in our study as described in Section 3.2.3.

Obtaining the velocity triangle at the impeller exit is necessary to estimate the slip factor using CFD. Stuart et al. explain their version of this procedure as shown in Figure 2.3 [22]. The calculation they employed is more complex than the scope of this study as it divides the active flow region at the impeller exit into jet and wake components. This method will not be employed as it is not feasible for the ROM used in this work. However, the basic approach outlined in Figure 2.3 is relevant. An isoSurface is placed at the blade trailing edge, and the actual average velocities passing through this surface can be extracted. The theoretical velocities are then obtained using knowledge of the impeller geometry and rotation speed. The theoretical and actual velocity triangles can be constructed as shown in Figure 1.4. Finally, Equation 2.10 can be used to calculate slip as obtained from CFD.

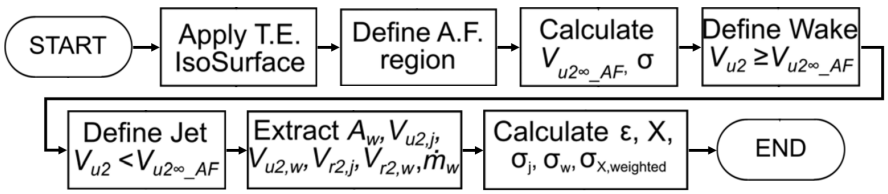

Figure 2.3: Postprocessing procedure for jet and wake slip factor evaluation. Adapted from: [22]

$$\sigma = 1 - \frac{\Delta V_{2t}}{U_2} \tag{2.10}$$

2.8. Summary

The previous sections of this chapter provide a brief overview of the principal published works that influenced this study. The testing, validation, and analysis performed in the following chapters will all be informed by these preceding studies and based on their findings. Finally, an overview of some of the most significant SFMs currently in use is presented in Table 2.1. This includes the year of publishing, the formula, and brief remarks to illustrate their historical context.

Table 2.1: A table summarising the details of the most widely used slip factor models.

Year	Model Name	Formula	Remarks
1927	Stodola	$1 - \frac{2\pi \cos \beta_{2b}}{Z\lambda_{\infty}}$	The oldest widely used model.
1967	Wiesner	$1 - \frac{\sqrt{\cos \beta_{2b}}}{Z^{0.7}}$	One of the most used models to this day.
2006	von Backstrom	$1 - \frac{1}{1+F_v\left(\frac{c}{s_2}\right)}$	A more modern approach that aims to combine several older models.
2011	Qiu	$1 - \frac{F\pi \cos \beta_{2b}}{Z} - \frac{Fs_2\phi_2}{4 \cos \beta_{2b}}\left(\frac{d\beta}{dm}\right)_2$	The newest model covered in this paper and the main focus of the study.

3

Methodology

This third chapter covers the implementation of the work outlined in the introduction. This will be done in two parts, mirroring the flow of the project itself. First, the new slip factor model was implemented into the reduced-order model and tested against Wiesner and von Backstrom's existing SFMs. Then, some of the compressors tested in the ROM will be built for CFD simulations in Ansys CFX. This chapter details the work done to test and validate the ROM.

3.1. Reduced-Order Model

As explained in section 1.1, an ROM was used for the preliminary compressor design employed in this project. It will be described in this section. Note that while the ROM can handle multi-stage compressor designs, for simplicity, it will be used in its single-stage format throughout this work.

3.1.1. ROM Overview

The ROM used in this study was first published by Giuffré et al. [5] Figure 3.1 shows the design flow of the model. First of all, the performance of a centrifugal compressor is considered a function of the parameters in Equation 3.1.

$$y = f(\phi_{t1}, \psi, \alpha_2, \beta, \gamma_{Pv}, Re, \sigma) \tag{3.1}$$

The first three parameters, the swallowing capacity ϕ_{t1}, which replaces the flow coefficient, the work coefficient ψ, and the absolute flow angle at the diffuser inlet α_2, are used to determine the impeller flow angles. The impeller work can then be determined by the pressure ratio β and the isentropic pressure-volume exponent γ_{Pv}, which measures the flow's departure from ideal gas behaviour. Finally, the viscous effects in the machine are quantified by the Reynolds number Re, while the geometric parameters are represented by σ.

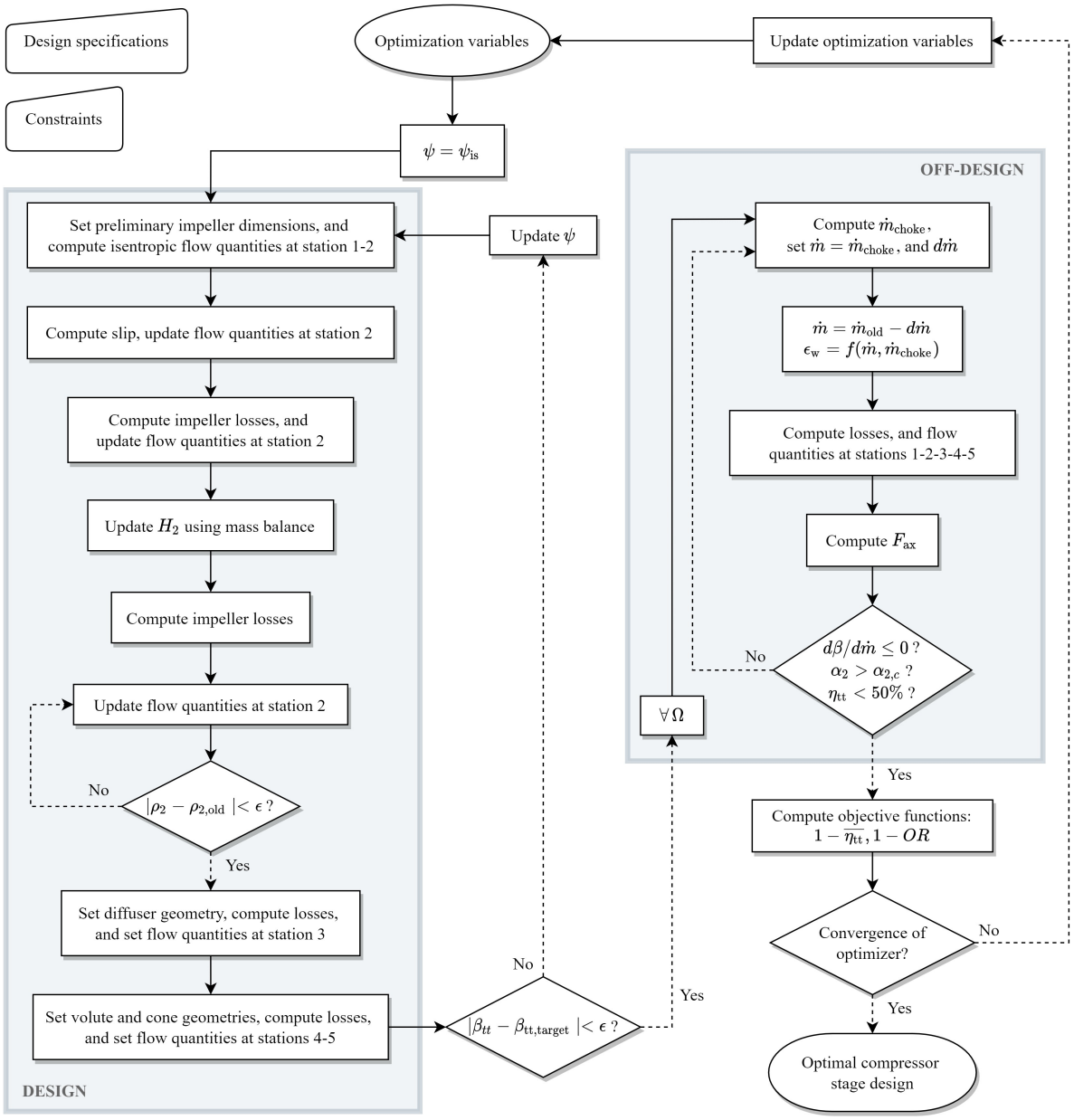

Figure 3.1: Flowchart of the reduced-order model: design, off-design, and optimisation. ϵ refers to the tolerance prescribed in the algorithm. [5]

Design Point

The inlet is assumed to have no guide vanes, and the diffuser is vaneless. This is also why the vaneless case was chosen for the Radiver compressor described in Section 3.2. This means that flow at the inlet is axial and uniform. However, inlet flow quantities are calculated at five spanwise locations (blade root, tip, midspan, and two intermediate points) to capture the free-vortex distribution. Considerations are in place for manufacturability, where the total number of blades is divided into main and splitter blades depending on throat length and variable thresholds set by the designer. Importantly, slip is calculated as part of the design-point computations. At the start of this project, two slip models were implemented, the Wiesner [6] and von Backstrom [7] models, with the choice being at the user's discretion. Fluid properties are referenced from the NIST REFPROP library [23]. The loss modelling used in the ROM is outside the scope of this study, which focuses on the inviscid slip effect. However, it is extensively detailed in the work of Giuffré [5].

Off-Design Performance

After setting the compressor design point and estimating the machine's performance, the off-design performance is evaluated, producing the full compressor map at different speedlines. This starts with calculating the compressor's choking mass flow rate. To do this, it is assumed that choking always occurs at the throat of the main blade passage. Thus, evaluating the Mach number at the throat as mass flow is incrementally increased results in a reasonable estimation of the choking point. Following this, the low end of the mass flow is found by estimating where surge occurs. Due to the difficulty of estimating the complex flow phenomena that result in surge, a semi-empirical correlation is used [5]. Similarly to the choke estimation, the mass flow rate is incrementally decreased until one of three phenomena occurs; surge as described above, rotating stall, or the efficiency drops below 60%.

Validation

The ROM includes a validation run mode which uses a similar process as described with the added input of experimental (or CFD) results enabling a comparative analysis.

As an example, Figure 3.2 presents a compressor operating map generated using the ROM for a well-known compressor, the Eckardt A and the widely used von Backstrom slip model. This shows that the ROM offers a good prediction of experimental results as the pressure ratio results are all within the ±5% uncertainty bands.

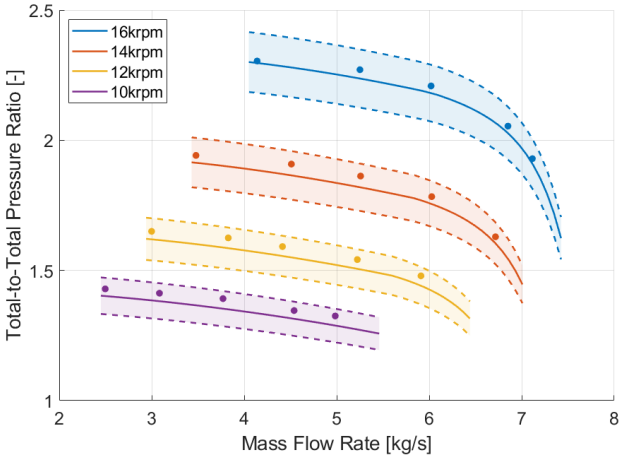

Figure 3.2: Compressor operating map as obtained from a ROM validation run. Compressor: Eckardt A, Slip Model: von Backstrom. Solid lines represent ROM predictions. Dashed lines and shaded regions represent ±5% uncertainty bands. Dots represent experimental data [24].

The primary motivation for the project came from ROM results regarding the in-house IRIS compressor, which ran at significantly higher speeds and resulted in unreliable predictions for pressure ratio when using both the von Backstrom and Wiesner slip models as shown in Figure 3.3.

Figure 3.3a shows a significant overprediction of the pressure ratio, reaching a discrepancy of around 20% at its highest. Notably, the highest differences occur at the fastest rotational speeds. While the

results using the von Backstrom model from 3.3b are more promising, they remain outside the defined uncertainty bands at higher speeds. In this case, the "experimental" results were the results of CFD simulations. It was further noted that while a discrepancy is evident in the pressure ratio estimations, the efficiency estimates were mostly accurate to the CFD results, as evident in Figure 3.4. This is a strong indicator that the model's weakness lies in the slip models used, as slip affects pressure ratios but not necessarily efficiencies.

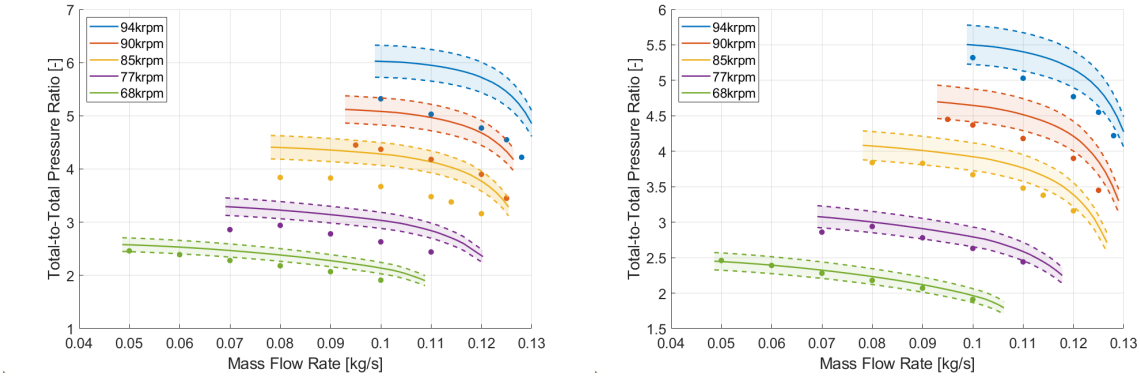

(a) Wiesner slip model

(b) von Backstrom slip model

Figure 3.3: Compressor operating maps obtained from the ROM for the in-house IRIS compressor using two slip models. Solid lines represent ROM predictions. Dashed lines and shaded regions represent ±5% uncertainty bands. Dots represent computational fluid dynamics data [10].

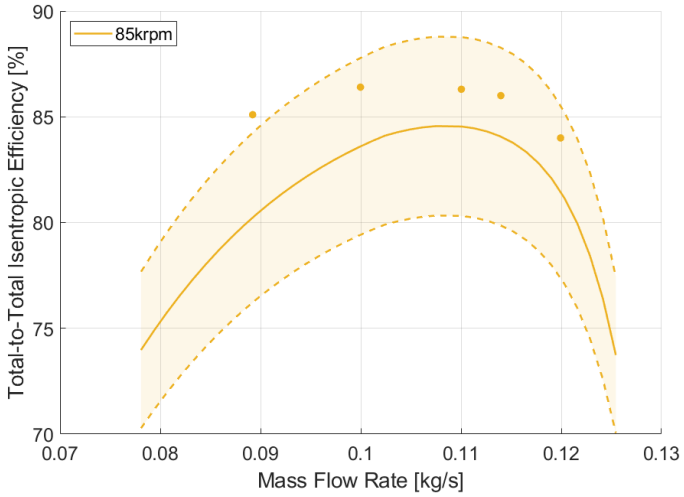

Figure 3.4: Total-to-total isentropic efficiency of the IRIS compressor at the 85krpm speedline as obtained from the reduced-order model using the Wiesner slip model. Dashed lines and shaded regions represent ±5% uncertainty bands. Dots represent computational fluid dynamics data [10].

3.1.2. Implementing the Qiu Model

The data flow is the main obstacle to implementing a new slip factor model in the ROM. This reduced-order model was designed with slip models such as Wiesner in mind. Comparing the Wiesner model in Equation 3.2 and the centrifugal Qiu model in Equation 3.3, it is evident that the Qiu model requires several more parameters that are not needed in the Wiesner model. These include the exit flow coefficient ϕ_2, the pitch at blade exit s_2, and the blade turning rate $(\frac{d\beta}{dm})_2$.

$$\sigma = 1 - \frac{\sqrt{\cos \beta_{2b}}}{Z^{0.7}} \tag{3.2}$$

$$\sigma = 1 - \frac{F\pi \cos \beta_{2b}}{Z} - \frac{Fs_2\phi_2}{4 \cos \beta_{2b}} \left(\frac{d\beta}{dm}\right)_2 \tag{3.3}$$

This means several new variables must be routed to the slip-calculating module. A new variable was created for the blade turning, which was not tracked during the run previously. This required constantly updating the meridional path coordinates m, as well as the blade angle β. Then, a finite difference was taken between the last two stations of the meridional and blade angle vectors. To do this, the entire length of the impeller is divided into one hundred stations, with station 1 being the impeller inlet and 100 being the impeller exit. This produced a value for the blade turning rate at the impeller exit $\left(\frac{dm}{d\beta}\right)_2$.

Also, it was necessary to calculate the shape factor F at every stage where the slip is estimated. Shape factor can be calculated through Equation 3.4. This is the term where the specific geometry of an impeller is taken into account, which is claimed to be a defining parameter of the slip factor estimation [19].

$$F = 1 - 2 \sin\left(\frac{\pi}{Z}\right) \sin\left(\frac{\pi}{Z} + \beta_{2b}\right) \cos\left(\beta_{2b}\right) - \frac{t_2}{s_2 \cos \beta_{2b}} \tag{3.4}$$

In the first iteration of the ROM, blade-turning rate data is not yet available, necessitating a simplified version of the Qiu SFM. So, the formula presented in Equation 3.5 was used when the ROM had no data on the meridional coordinates. This version included only the first radial term and excluded the turning term entirely.

$$1 - \frac{F\pi \cos \beta_{2b}}{Z} \tag{3.5}$$

Both the full and simplified versions of the Qiu model were then implemented into several modules of the ROM, where the slip factor is estimated. Namely, the main slip estimation, choking mass flow, and off-design isentropic flow modules. As can be inferred from Figure 3.1, the slip factor is calculated multiple times even if not explicitly stated in the flowchart. For example, a slip prediction is needed to calculate the meridional Mach number at the impeller outlet when computing the choking mass flow rate in the off-design section. However, the most critical use for the slip calculation is updating the compressor velocity triangles, which are heavily affected by slip and essential to the compressor design process. A sample of the code used for this implementation is presented in Appendix A. The results of this implementation will be presented in section 4.1.

3.2. CFD Simulations

As a basis of comparison with the results of the ROM and experimental data, several Computational Fluid Dynamics (CFD) simulations were conducted on two test cases using the Ansys Inc. Workbench. BladeGen was used to recreate the blade geometry. Then, the mesh was generated using Turbogrid. CFX-pre enabled the simulation setups. The simulations were monitored in the CFX Solver Manager. Finally, CFD-post was used for post-processing.

Test Case Details

Two test cases were used for the CFD simulations. Ansys CFX was chosen as the CFD solver because it is a reliable, well-documented solver and the industry standard for such cases. The first case was the in-house IRIS compressor. This is a high-speed, miniature centrifugal compressor designed at TU Delft that uses refrigerant R1233zd(E) as its fluid. Due to the complexity of this machine, it was decided that no simulations would be run during this study on the IRIS case. The IRIS case is complicated to simulate mainly because of the choice of fluid and the high rotational speeds. This makes the case quite delicate, requiring large amounts of time and computational power, necessitating the use of a computer cluster which is outside the scope of this study. High-resolution simulations had already been completed during the design process by the machine's original designers [5]. Thus, those results will be used in this study for comparison with the other data sources. However, the process of generating this machine's performance map will be described here to present the conditions it was tested under.

The second test case was for the Radiver compressor, a well-documented open test case which uses air as its working fluid. These machines were chosen because they allow various conditions to test the presented SFMs, including different working fluids. The measurements on the test case "Radiver" were carried out at the Institute of Jet Propulsion and Turbomachinery at RWTH Aachen, Germany. Part of the investigations was funded by the Deutsche Forschungsgemeinschaft (DFG) [1] [2] [3].

The original study by Ziegler tested the Radiver compressor with various diffuser configurations, but the vanless version was used here. On the other hand, the IRIS compressor is already a vaneless diffuser machine. The Radiver compressor features 15 main blades and no splitter blades. On the other hand, the IRIS compressor has 7 main blades and 7 splitter blades. The basic details of the two test cases are summarised in Table 3.1.

Table 3.1: A table summarising the basic information of the two test cases used in the CFD analysis.

Parameter	IRIS	Radiver
Fluid	R1233zd(E)	Air
Number of Bladesets	7	15
Inlet Total Pressure [kPa]	47.8	60
Inlet Total Temperature [K]	278	296
Rotation Speeds [krpm]	68 - 94	21 - 35
Mass Flow Rates [kg/s]	0.05 - 0.13	0.5 - 1.5
Impeller Tip Radius [mm]	22.8	135
Blade Tip Gap [mm]	0.1	0.7

3.2.1. Compressor Geometries

Seeing as the IRIS compressor was designed by team members at TU Delft, the data for it was more readily available and essentially ready to simulate [5]. The geometry is shown in Figure 3.5 and the mesh in Figure 3.6.

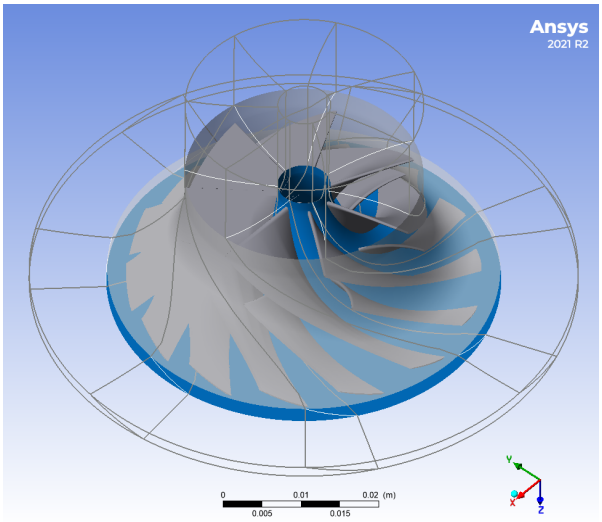

Figure 3.5: Picture of the IRIS compressor geometry as it was generated in Ansys TurboGrid

For the Radiver compressor, however, only blade passage coordinates were supplied, so a more elaborate process was needed to prepare that geometry for simulation. The most challenging part of this process was the first step, the TurboGrid implementation. The plan was originally to use Turbo-

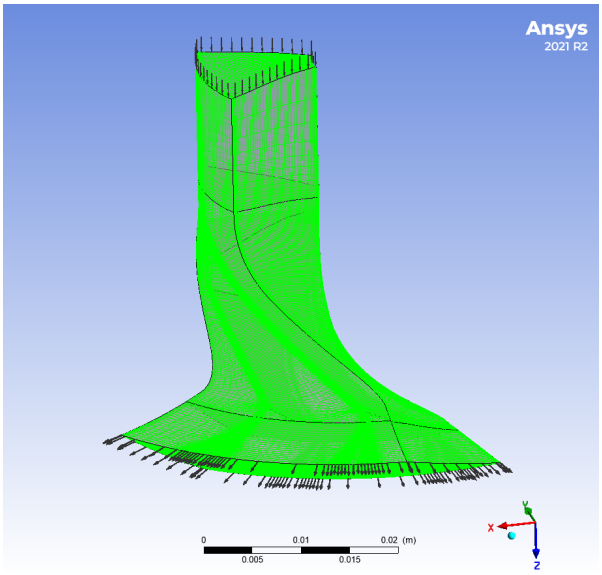

Figure 3.6: Ansys picture of the mesh used for the IRIS compressor.

Grid since the blade passage coordinates were available directly. Unfortunately, that was not feasible. TurboGrid is a powerful software that offers many helpful solutions to streamline turbomachinery simulation. Still, it requires tight control of its inputs, as any deviations can lead to insurmountable errors. Consequently, after significant trial and error, we went one step back to BladeGen, hoping to produce files that TurboGrid would accept from the start. That was indeed a successful line. BladeGen requires the blade coordinates in the form XR to generate a blade geometry successfully. These are axial (X) and radial (R) coordinates in a meridional view of the impeller.

The basis for this information was obtained from Figure 3.7. However, quite a bit of manipulation was still required. First, the coordinates were for the shroud line, so the hub line was calculated using the shroud information and the quantities L and ϵ shown in Figure 3.7. Finally, the angle ϕ was used to calculate the full three-dimensional cartesian coordinates, mainly used for verification.

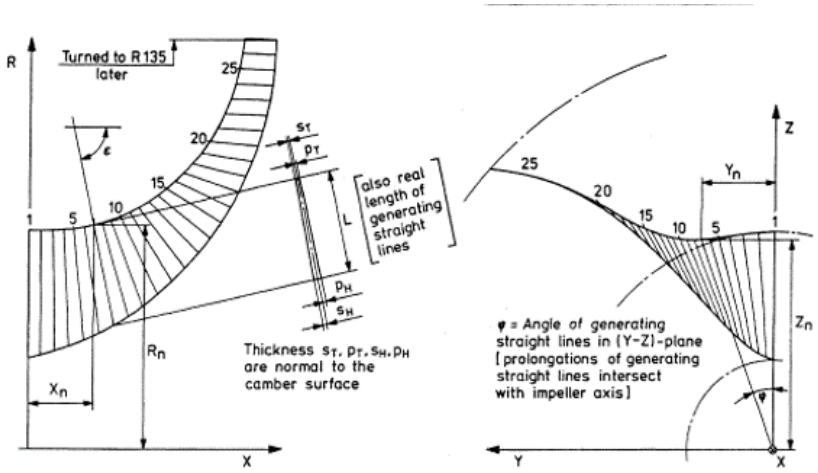

Figure 3.7: Diagram of the MTU impeller geometry. Left: meridional view (X is axial length, R is radial). Right: three-dimensional view. [3]

The BladeGen import function was used to allow the detection of the blade passage geometry. Subsequently, the generated curve files were available for use in TurboGrid. The generated geometry in Turbogrid is shown in Figure 3.8. The blue-shaded region represents the impeller, while the wireframes seen above and below are the inlet and outlet regions, respectively.

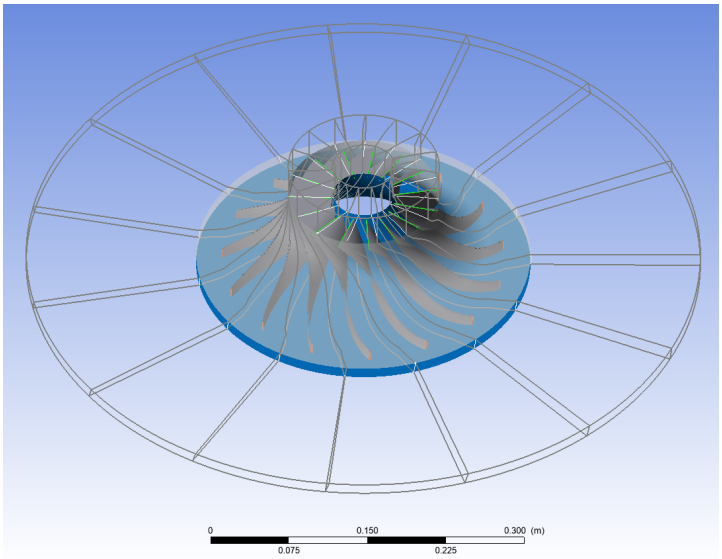

Figure 3.8: Picture of the Radiver compressor geometry as it was generated in Ansys TurboGrid.

3.2.2. Mesh Generation

The next step was the mesh generation done in TurboGrid. As ever, this process included some trial and error. The mesh region was split into three sections: the inlet, passage, and outlet. The mesh density was highest in the main passage, followed by the outlet; seeing as no work was done on the fluid in the inlet section, a higher mesh density would not be helpful. Figure 3.9 shows the final mesh for the Radiver compressor. Due to the flow complexity in these regions, the highest element density is found around the blade and in the blade's wake region.

Mesh Analysis Limits

The mesh was made in such a way as to maintain the mesh analysis variables within their default limits in TurboGrid while also setting the Yplus values to 0.99. These are not definitive quality measures and can vary according to the mesh designer's needs. For this analysis, they were kept to the default values according to the Ansys TurboGrid user's guide and used as a general guideline while also considering other factors. These limits are summarised in Table 3.2 ranked from top to bottom in order of importance to the mesh quality as stated in the TurboGrid user's guide. Minimum volume is a measure of element volume essential to a good-quality mesh, as negative volumes render the mesh unusable. Maximum/minimum face angles are considered measures of skewness as they measure the angle between the two edges of a face that touch a node, so it is vital to keep them within limits to minimise the effect of skewness on the mesh. The edge length ratio can be considered an aspect ratio as it measures the longest edge of a face divided by its shortest. The element volume ratio is calculated as the maximum volume touching a particular node divided by the minimum volume touching that node. Finally, the connectivity number is the number of elements connected to a specific node.

Mesh Settings

While maintaining the mesh analysis variables within acceptable ranges, the mesh generation process could begin. Firstly, the boundary layer refinement control method was chosen as "First Element Offset," where the Yplus value can be selected, and this was set to 0.99, targeting a maximum expansion rate of 1.2. This defines the rate at which elements grow compared to the boundary layer elements. For the blade passage, a boundary layer distribution method was also chosen. This ensures the most critical areas, the boundary layers (hub, shroud, and blade walls), are well resolved while minimising the expansion ratio as much as possible to mitigate the adverse effects. The hub tip settings were unchangeable as there was no tip gap at the hub for this machine. The shroud tip, however, was set to a uniform distribution of 20 elements. This kept the expansion rates down and maintained the Yplus value as well. Then, the inlet and outlet regions were set to H-grid meshes targeting expansion rates of 1 and 1.1, respectively. The last step was the global size factor, a global multiplier that increases or

Table 3.2: The mesh analysis limits maintained to ensure mesh quality.

Mesh Limit	Value
Minimum Volume $[m^3]$	0
Minimum Face Angle [deg]	15
Maximum Face Angle [deg]	165
Maximum Edge Length Ratio	1000
Maximum Element Volume Ratio	20
Maximum Connectivity Number	12

decreases overall mesh density across the entire domain. This was increased incrementally until the mesh limits in Table 3.2 were all satisfied. This occurred at a factor of 1.7. Finally, all of this resulted in a mesh of 2.5 million nodes. This was deemed satisfactory as larger meshes did not produce meaningful improvements, and smaller ones would not meet the TurboGrid mesh limits.

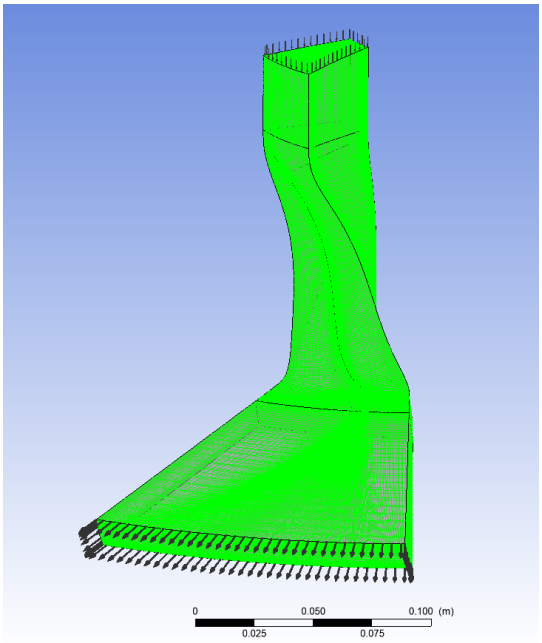

Figure 3.9: Ansys picture of the mesh used for the Radiver compressor.

3.2.3. Simulation Setups

When the mesh is ready, Ansys CFX-Pre sets up the simulation conditions. For all the runs done in the course of this study, the setups were similar. This section will detail that process.

The "Turbo Mode" in CFX-Pre was used as it simplifies the process greatly when simulating turbomachines. The turbulence model was chosen to be k-ω Shear Stress Transport (SST) as it is the recommended model for turbomachinery simulations.

Timescale Calculation

Another important consideration is the simulation timescale. Here, the Ansys user's guide recommendations were used, and a physical timescale calculated according to the rotation speed at each speedline was adopted. Equation 3.6 shows an example calculation for the timescale used at a speed of 28,541 RPM (the 80% speedline of the Radiver compressor). This value was parametrised in Ansys Workbench such that it is automatically calculated for each run depending on the compressor speed.

This was important due to the nature of these turbomachinery simulations, as attempts with smaller timescales could often prevent convergence. A small timescale can help stabilise the solution and avoid oscillations. However, the solver starts picking up transient effects if it is too small. One such effect was the Mach number in the machine, where runs with timescale factors much smaller than they should be, led to rapidly increasing velocities, which caused the solver to display "Mach number is too high" warnings and eventually stop within a few iterations due to numerical overflow errors. Thus, an appropriate timescale is even more critical in high-speed compressor simulations than it usually is.

On the other hand, maintaining the IRIS compressor's stability was difficult. So, a much smaller timescale was necessary. An auto-timescale was used such that the solver itself would choose the appropriate timescale governed by a user-controlled timescale factor. This was a large part of the difficulty of running the IRIS case on a personal computer compared to a server cluster. A small timescale factor would be set initially; once the simulation stabilises, this factor would be increased by factors of two to five. This process would be repeated two to three times until convergence. While this is ostensibly the only way to reach convergence for a rather sensitive simulation, it significantly increases the time commitment. That made it unfeasible for this project.

$$\begin{aligned} N &= 28541\,RPM \times \frac{2\pi}{60} = 2988\,rad/s \\ Timescale &= \frac{0.1}{2988} = 3.35 \times 10^{-5}\,s \end{aligned} \tag{3.6}$$

Simulation Conditions

It was important to manage the boundary conditions for both compressors correctly. The chosen conditions were total temperature and pressure at the inlet and mass flow rate at the outlet. In the case of the Radiver compressor, the inlet conditions, rotation speeds, and mass flow rates were set to match the experimental conditions. However, the conditions reported in the original publication[1] were using corrected values at a reference of $T_{ref} = 288.15\,K$ and $P_{ref} = 101.325\,kPa$, so the conversion was made to obtain the actual rotation speeds and mass flow rates at the actual inlet conditions of $T_t = 296\,K$ and $P_t = 60\,kPa$. The mass flow rates varied between $0.5 - 1.5\,kg/s$ depending on the speedline. There were five speedlines at 60, 70, 80, 90, and 100% of the actual design speed of $35,676\,RPM$.

The choice of conditions was more relaxed for the IRIS compressor as there were no experimental conditions to compare, so the speeds and mass flow rates were taken from the original design data using the ROM. The IRIS inlet conditions were set as $T_t = 278.13\,K$ and $P_t = 47.8\,kPa$. The mass flow rates were varied between $0.05 - 0.13\,kg/s$ while the speedlines were at 80, 90, 100, 105, and 110% of the design speed of $85,748\,RPM$. The simulation conditions are summarised in Table 3.3.

Table 3.3: The simulation conditions for the two test cases

Condition	IRIS	Radiver
Inlet Total Temperature [K]	278	296
Inlet Total Pressure [kPa]	47.8	60
Outlet Mass Flow Rate [kg/s]	0.05 - 0.13	0.5 - 1.5
Speedlines [RPM]	68,598 77,173 85,748 90,035 94,323	21,406 24,973 28,541 32,189 35,676

Working Fluid

Uniquely for the IRIS compressor, the fluid choice is a significant concern. This is simple for the Radiver case, as air is an inherently available material in the Ansys CFX library. The refrigerant used in the IRIS machine, however, is not. So, a method was needed to insert the material properties into Ansys CFX.

This came by way of a Real Gas Properties (RGP) file. This file can be created using a feature in Ansys Fluent and a supplied batch file. An RGP file is similar to the property tables found in various sources but formatted for use in Ansys. These files are generated using the NIST REFPROP fluid database. By defining a range of temperatures and pressures, the saturation and superheated tables for a given material are generated in an RGP file which Ansys then uses throughout the simulation to define the fluid properties at different temperatures and pressures. Thus, an RGP file was generated for R1233zd(E), focusing on the superheated tables as that is the fluid's state during the compression process. The ranges chosen were temperatures of 200 to 800 Kelvin and pressures of 5 kPa to 1 MPa.

Parametrisation

Steady-state simulations were conducted at several performance points to collect as much data as possible for comparison with the other sources, namely experimental data and the ROM. These all started with first-order, upwind advection schemes before using those results as initial conditions to conduct high-resolution simulations, which will be used in section 4.2.

To streamline the simulation process, a parametric approach was adopted. The "Performance Map" component system in Ansys Workbench allows the user to set specific values as input parameters and chosen output parameters at the end of the simulations. For this case, the input parameters were rotation speed and mass flow rate, and the output parameters were pressure ratio and efficiency. For the Radiver compressor, 31 performance points were created with a steady-state simulation for each one to create the performance map of the machine. This method allows the CFD software to automatically complete all simulations in an optimised order such that each point is close to the one following it and can be used as an initial guess for the simulation. A snapshot of this functionality is presented in Appendix B.

4

Results

The results obtained from the reduced-order model and CFD simulations will be documented. The first section will cover the results of the reduced-order model, comparing the capabilities of the different slip factor models used in the design process. Secondly, the CFD simulation results for both test cases will be presented. Note that all values (i.e. mass flow rates, rotational speeds, etc.) are reported as their actual values at the real inlet conditions stated in Section 3.2, not as corrected values at standard conditions. Additional results are presented in Appendix C.

4.1. ROM Results

The reduced order model has been validated and tested using three different slip factor models. Namely, the Wiesner, von Backstrom, and Qiu models. These results are presented in this section.

Pressure Ratios

First of all, the total-to-total pressure ratios of the compressors were estimated, with the only difference between runs being the slip factor model used; this allowed us to obtain the compressor operating maps. Figure 4.1 and Figure 4.2 show these results for the Radiver and IRIS compressors, respectively.

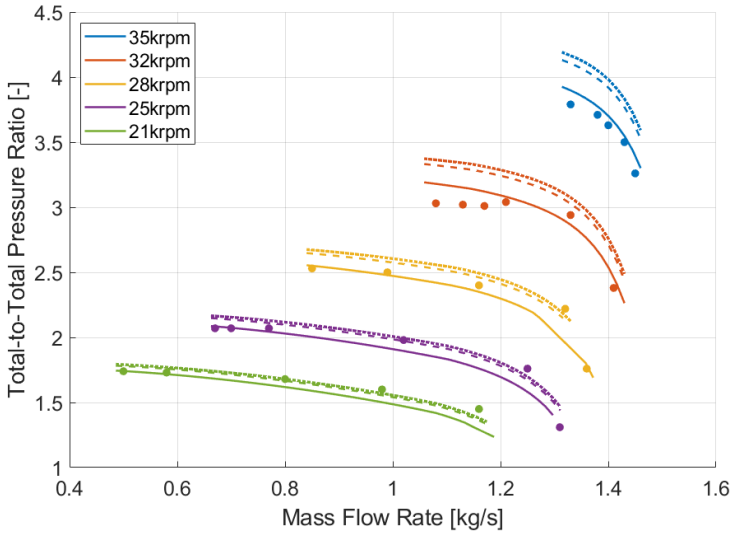

Figure 4.1: Operating map for the Radiver compressor from the reduced-order model. Dot markers represent experimental results [1]. Slip models: solid - Qiu, dashed - von Backstrom, dotted - Wiesner.

Figures 4.1 and 4.2 show each model's accuracy. Looking at Figure 4.1, it is evident that the Wiesner model starts facing difficulties with increased compressor speeds. This results in an average percentage

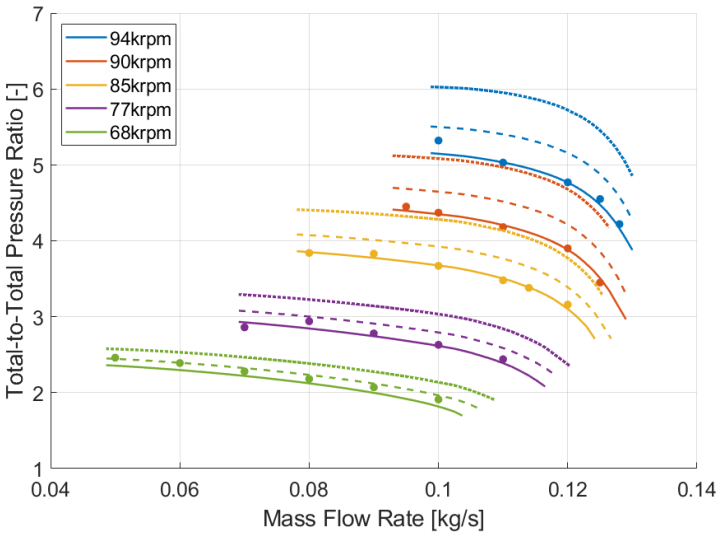

Figure 4.2: Operating map for the IRIS compressor from the reduced-order model. Dot markers represent CFD results [5]. Slip models: solid - Qiu, dashed - von Backstrom, dotted - Wiesner.

error of 10% at the highest speedline, significantly higher than the Qiu model's 2% average error. This becomes even more evident in Figure 4.2, as the IRIS compressor runs at overall much higher speeds. At the highest speedline, the Wiesner model exhibits a percentage error of 19% while the Qiu model is only 1%.

The von Backstrom model fares better than Wiesner but trends further away as speeds increase. It achieved an average percentage error of 8% and 6% at the highest speedlines of the Radiver and IRIS compressors, respectively. The Qiu compressor provides the most reliable estimates for both compressors, enabling high-accuracy predictions at lower and higher speeds. These initial figures immediately show that the choice of SFM has a tangible impact on compressor performance predictions. Table 4.1 presents a summary of the accuracy of each SFM.

Table 4.1: A table summarising the average error percentages of each SFM for the Radiver and IRIS compressors.

	Slip Factor Model Accuracy		
Compressor	Wiesner	von Backstrom	Qiu
Radiver	6%	5%	3%
IRIS	15%	5%	1%
Average	10%	5%	2%

Slip Factor Models

The subsequent results can help explain the trends in the pressure ratio plots. Figure 4.3 presents the slip factor estimations obtained from the three models in question for the Radiver and IRIS compressors. Figure 4.4 provides a closer look at the Qiu model estimates for each compressor. Recalling the slip factor definition, it is a nondimensional measure of the angle created between the blade metal angle at the impeller exit and the mean flow angle. This can be calculated using Equation 4.1. However, this information is unavailable during the design process and must be computed using slip factor models that estimate the effect. The formulas used by each model are collected in Table 4.2.

$$\sigma = 1 - \frac{\Delta V_{2t}}{U_2} \tag{4.1}$$

Table 4.2: A table collecting the formulas of the three slip factor models used in the reduced-order model.

Model Name	Formula	Remarks
Wiesner [6]	$1 - \frac{\sqrt{\cos \beta_{2,blade}}}{Z^{0.7}}$	Based on blade metal angle and number of blades.
von Backstrom [7]	$1 - \frac{1}{1+F\left(\frac{c}{s_e}\right)}$	Based on the blade solidity and blade angles
Qiu [19]	$1 - \frac{F\pi \cos \beta_{2b}}{Z} - \frac{Fs_2\phi_2}{4 \cos \beta_{2b}} \left(\frac{d\beta}{dm}\right)_2$	Along with geometrical terms, also based on the flow coefficient phi

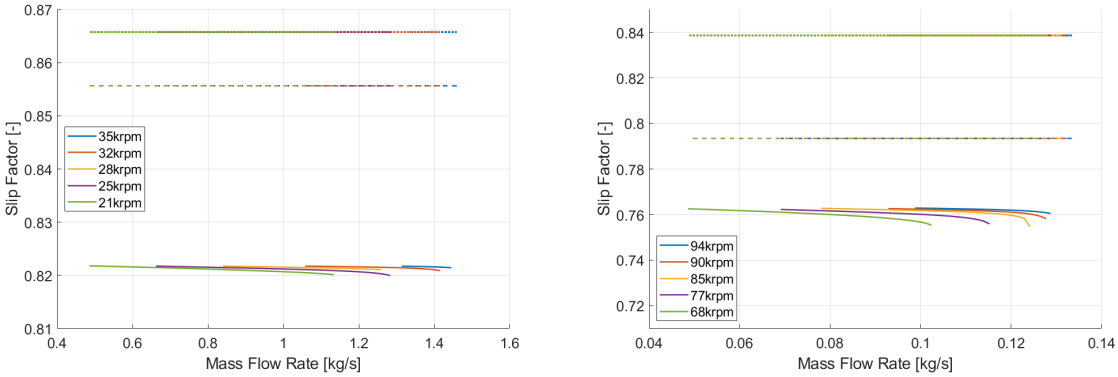

(a) Radiver (b) IRIS

Figure 4.3: Slip factor estimations obtained from the reduced-order model. Slip models: solid - Qiu, dashed - von Backstrom, dotted - Wiesner.

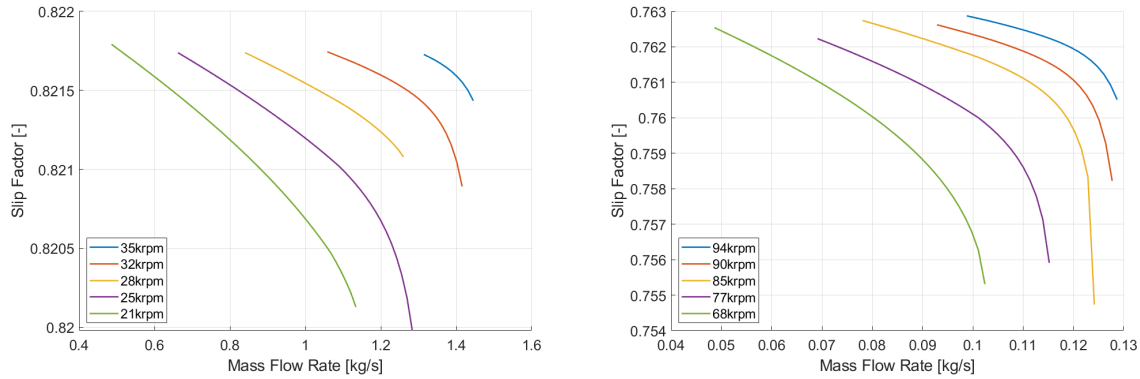

(a) Radiver (b) IRIS

Figure 4.4: Slip factor estimations for the Radiver and IRIS compressors obtained from the reduced-order model using the Qiu slip model.

Two conclusions can be drawn from Figures 4.3 and 4.4. First, the von Backstrom and Wiesner models are constant for all speedlines and mass flow rates. This is expected as these models are based entirely on compressor geometry, so for each compressor, the slip estimation is the same at different operating conditions. In contrast, the Qiu slip model is variable depending on both compressor speeds and mass flow rates. This is also evident from the model equations presented in Table 4.2.

The second aspect is the average value of the slip factor that each model obtained. The Qiu model provides a much lower overall estimate of the slip factor than the other two. With slip factor as defined in Equation 4.1, a lower slip factor value means that the ratio of velocities is larger, which means the

difference between the flow and blade angles at the impeller exit is larger. This finally leads to a lower pressure ratio estimate, which is the more accurate result as evidenced by Figure 4.1 and Figure 4.2.

To measure the performance of the Qiu model in more detail, the compressor performance maps were plotted to compare the prediction accuracy with experimental and CFD results for the Radiver and IRIS compressors, respectively.

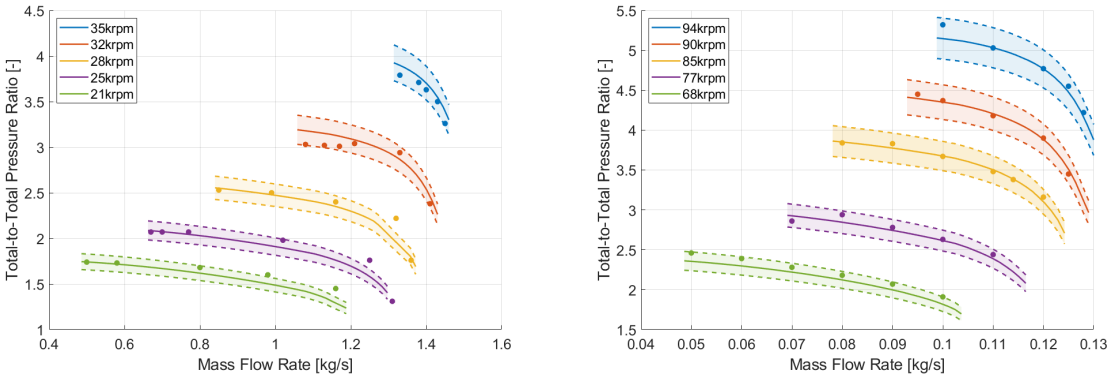

(a) Radiver. Dot markers represent experimental results [1]

(b) IRIS. Dot markers represent CFD results [5].

Figure 4.5: Operating maps for the Radiver and IRIS compressors from the reduced-order model. Solid lines represent the reduced-order model predictions using the Qiu slip model. Dashed lines are ±5% uncertainty bands about the ROM predictions.

Figure 4.5 shows that almost all data points in both cases are within the 5% bands of the reduced-order results, even at high speeds. This indicates that the Qiu model offers robust capabilities and is valid for different compressors, geometries, and flow conditions.

Efficiency Estimates

It is also worth examining the efficiency results obtained from the reduced-order model. For the Radiver compressor, only the 80% speedline (28 krpm) efficiency was reported and will be used for comparison. The design speedline of 100% (85 krpm) will be used for the IRIS compressor.

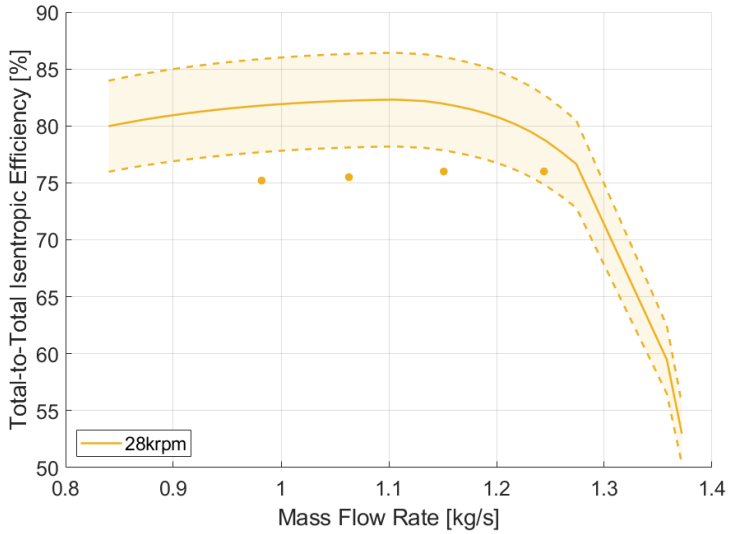

Figure 4.6: Total-to-total isentropic efficiency estimation for the Radiver compressor at 28 krpm obtained from the reduced-order model using the Qiu slip model. Dot markers represent experimental results [1]

Figure 4.6 shows the efficiency as obtained from the ROM for the Radiver compressor. The model has slightly overestimated the machine's efficiency overall while the general trend is captured well. One possible explanation is related to how the efficiency was calculated in the experimental test rig and what regions of the compressor were considered [1]. In this case, the only efficiency reported in

the literature for the vaneless case (the one in question in this study) was that of the impeller, diffuser, and collector, which is generally lower than that for only the impeller and diffuser, which is the one estimated in the reduced order model.

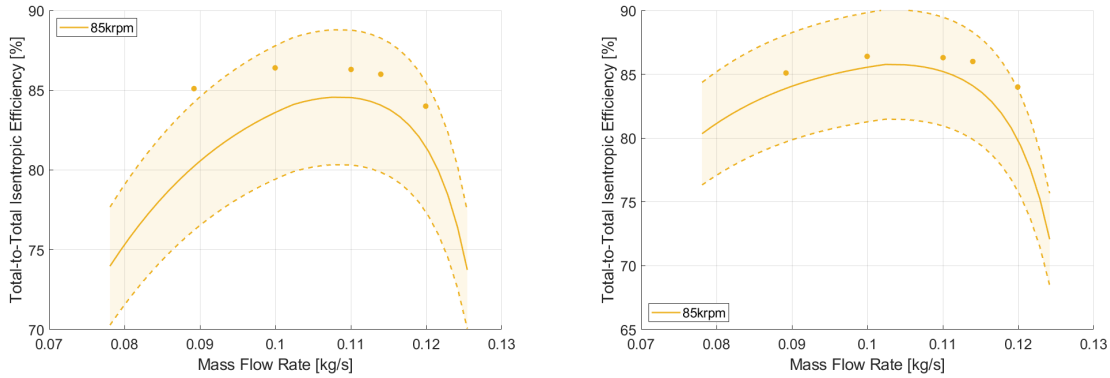

(a) Wiesner slip model. (b) Qiu slip model.

Figure 4.7: Total-to-total isentropic efficiency estimates obtained from the reduced-order model for the IRIS compressor at 85krpm using two different slip models. Dot markers represent CFD results [5].

Figure 4.7 presents the efficiency estimate for the IRIS compressor at the 100% speedline. The slip model does indeed affect the efficiency estimation, as nothing else was changed between these two calculations. However, the Wiesner model, which was off by quite a margin in its pressure ratio estimates, performs adequately in its efficiency predictions. It was stated in Section 1.2 that slip is an inviscid effect that should not cause losses. While true, the choice of slip model directly affects the velocity triangles at the impeller exit, which has a noticeable effect on compressor efficiency.

In this test case, while the Wiesner model performs well, it is clear that the Qiu model captures the trend of the efficiency range more accurately, especially close to the edges of the distribution. This can be attributed to the Qiu model's inclusion of a flow coefficient term and the blade turning rate, which allows the model to more accurately predict performance in non-zero sweep impellers such as this one.

Further Validation

The model was also validated on other test cases, including the Eckardt series of impellers [24] [25], and the EPFL Schiffmann compressor [26]. Figure 4.8 shows the operating maps of the Eckardt O and Schiffmann compressors. Additional validation plots can be found in Appendix C.

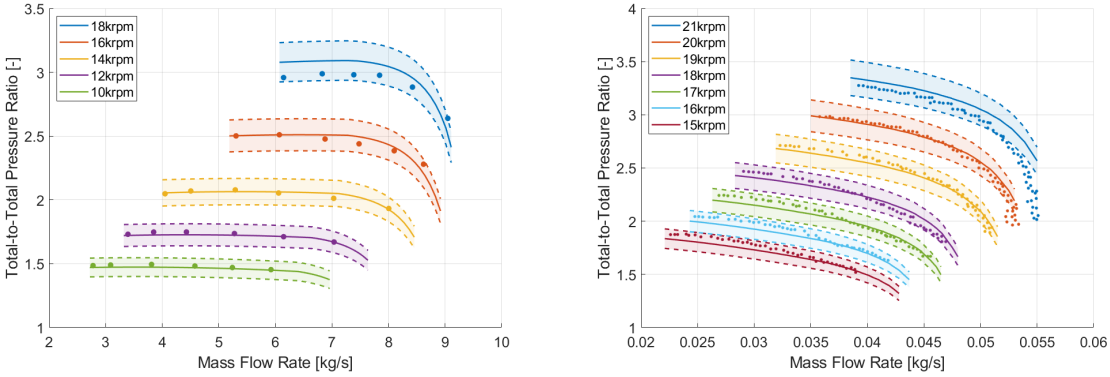

(a) Eckardt O (b) Schiffmann

Figure 4.8: Operating map for the Eckardt O and Schiffmann compressors from the reduced-order model. Solid lines represent the reduced-order model predictions using the Qiu slip model. Dashed lines are ±5% uncertainty bands about the ROM predictions. Dots represent experimental results.

The results plotted in Figure 4.8 show good agreement of the ROM using the Qiu slip model with experimental results for these compressors. This demonstrates the ROM accuracy in predicting the

performance of compressors of various sizes and speeds.

4.2. CFD Simulation Results

Two test cases were chosen for the CFD simulations: IRIS and Radiver. The details of these test cases and how they were simulated are described in Section 3.2. This section will present the results of those simulations.

CFD Flow Field

When simulating the compressors using CFD, there are two primary goals. First, we look to determine the overall compressor performance in terms of pressure ratios and efficiencies. The second aspect is the flow field, especially around the impeller exit. Knowledge of the velocities at the impeller exit allows the calculation of the slip factor directly. Figure 4.9 shows the streamlines through the blade passage of the Radiver compressor at the design point, $N = 28,541\ RPM,\ m = 1kg/s$. Figure 4.10 presents the same view for the IRIS compressor at its design point, $N = 85,748\ RPM,\ m = 0.114kg/s$

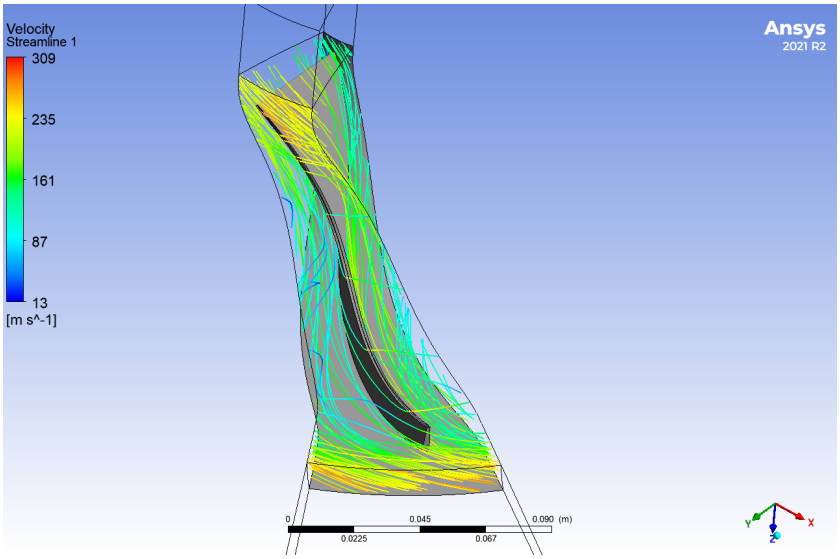

Figure 4.9: Velocity streamlines through the blade passage of the Radiver compressor at 28,541 RPM and 1 kg/s.

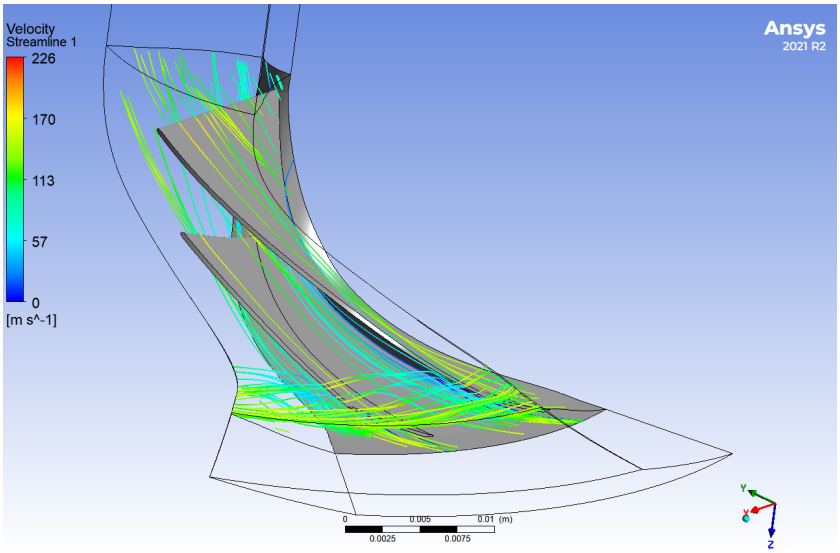

Figure 4.10: Velocity streamlines through the blade passage of the IRIS compressor at 85,748 RPM and 0.114 kg/s.

It is impossible to directly compare the two compressor designs based solely on the flow field images. However, we can focus on the impeller exit, the primary region of study for the slip effect. An interesting observation can be made about the differences between the two machines by examining the velocity contours of both compressors at the impeller exit at their respective design points.

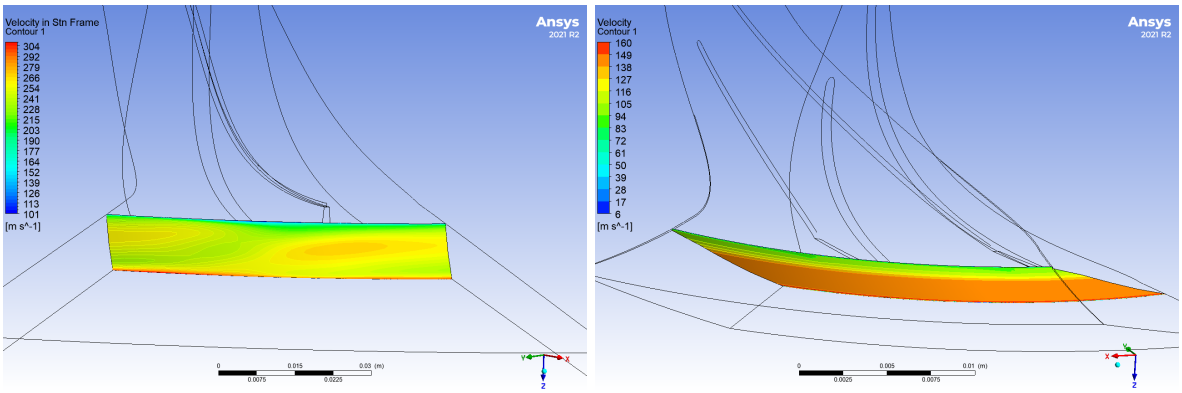

(a) Radiver (b) IRIS

Figure 4.11: Velocity contours at the impeller exit of the Radiver and IRIS compressors. Radiver conditions: 28,541 RPM and 1 kg/s. IRIS conditions: 85,748 RPM and 0.114 kg/s.

Figure 4.11 illustrates the effect of one significant difference between the two designs, the splitter blade. The Radiver compressor contour displays ”hot spots” in the blade’s wake, while the IRIS compressor’s velocity exiting the impeller is more uniform in the blade-to-blade plane. This can be directly attributed to the splitter blade smoothing out the velocity profile at the impeller exit. While this study, and most others, use average velocities through the impeller exit to compute slip as described in Section 4.2, the effect of these velocity distributions on slip is worth investigating.

Another indicator to consider for almost all CFD simulations is the Mach distribution. Figures 4.12 and 4.13 show the Mach number distributions for the Radiver and IRIS compressor in the blade-to-blade plane at half-span. Here, it is noted that the IRIS compressor has a much higher maximum Mach number near the trailing edge of the main blade. This is expected due to the IRIS compressor’s higher rotation speed and pressure ratio than the Radiver.

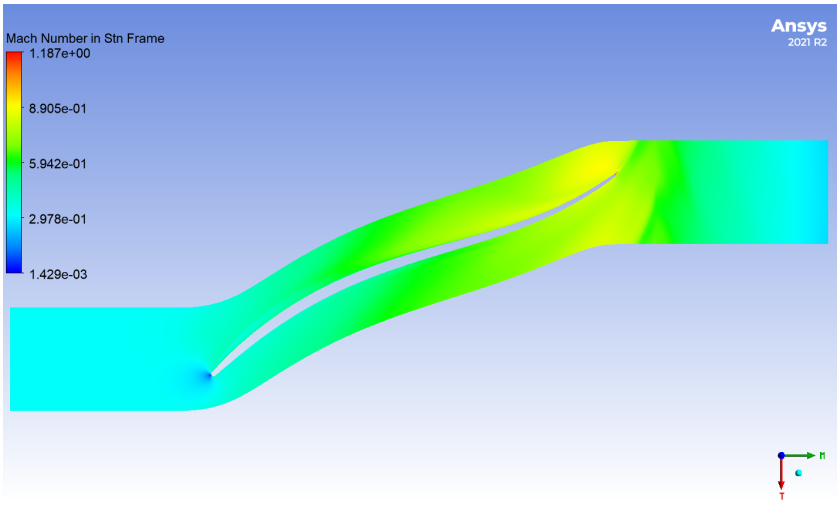

Figure 4.12: Mach number distribution in the blade-to-blade plane at half-span for the Radiver compressor at 28,541 RPM and 1 kg/s.

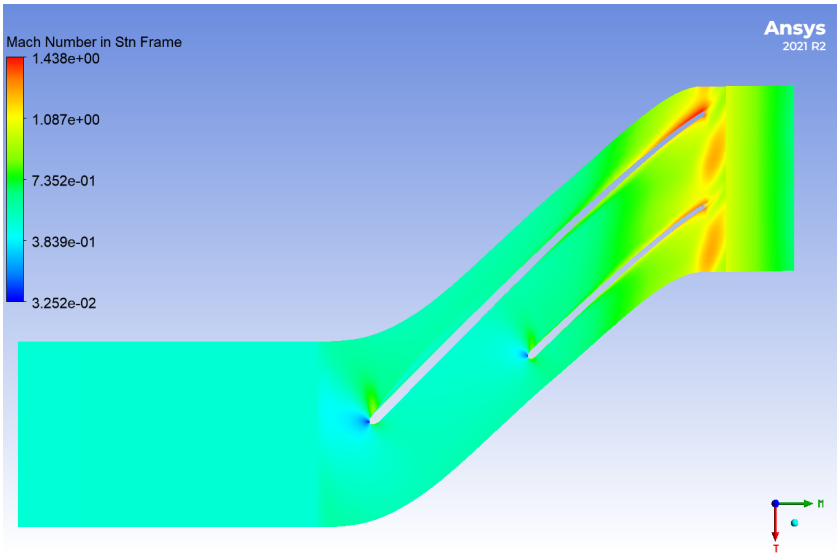

Figure 4.13: Mach number distribution in the blade-to-blade plane at half-span for the IRIS compressor at 85,748 RPM and 0.114 kg/s.

Similar plots at all other speedlines for the Radiver and IRIS compressors can be found in Appendix C.

Pressure Ratio

The first area of comparison is the pressure ratio, and Figure 4.14 shows the CFD results compared to the reduced-order model and experimental values for the Radiver compressor.

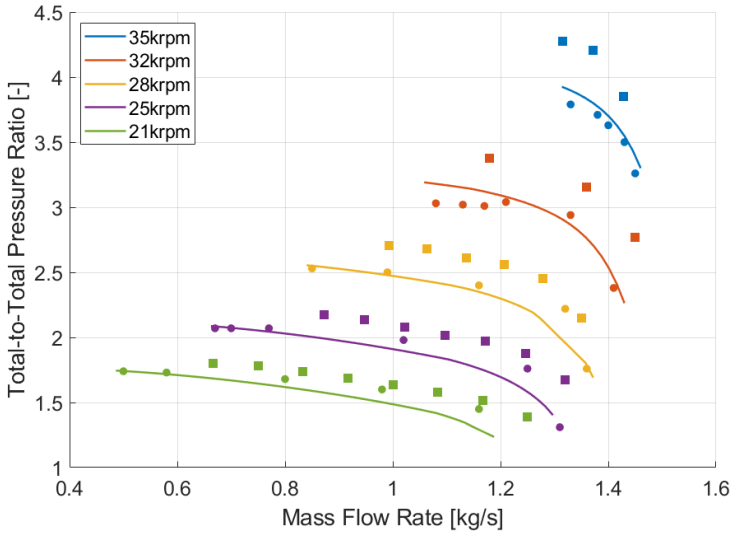

Figure 4.14: Operating map for the Radiver compressor. Solid lines represent reduced-order model results. Square markers represent CFD results. Dot markers represent experimental results [1].

The CFD simulations generally overestimated the pressure ratio, especially at higher speeds. On average, the CFD results had a percentage error of around 8%, while the ROM results using the Qiu model had an average error of 3%. The reasons for the discrepancy can be many, as CFD simulations can be more difficult when attempting to recreate an existing machine rather than a novel design.

The main obstacles lie in recreating the geometry. While essential data like the blade passage coordinates were available, other vital parameters, such as the hub and shroud or inlet and outlet details, had to be approximated from non-exact sources. These slight imperfections in a relatively small machine meant the final results were off considerably more than intended. These effects were more

pronounced at higher speeds where minor geometrical differences become amplified. The difference is further compounded by the fact that the ROM uses only the global geometry of the machine. It does not require the entire 3D geometry as CFD simulations do. This makes the ROM an ideal choice for cases where the compressor geometry is not fully available.

Along with the geometry, error sources can include convergence effects, where it becomes more difficult to obtain low convergence residuals the more complex a problem is. This was especially evident when studying the IRIS compressor but also affected the Radiver.

Slip Factor

To eliminate other influences on the results, the slip factor for each compressor was calculated using the velocity triangles obtained from Ansys CFD-post. The main required component was the average velocity across the impeller exit V_2. The rotational velocity component U_2 is known through the radius and compressor rotational speed. Once the velocities were obtained, the fundamental slip relation in Equation 4.8 was used to calculate the slip factor. This depends on the difference between the actual velocity triangle (obtained from CFD) and the theoretical triangle calculated from the impeller geometry. Equations 4.2 - 4.8 describe how these values were computed based on the diagram in Figure 4.15. The same process was used for both compressors at all points.

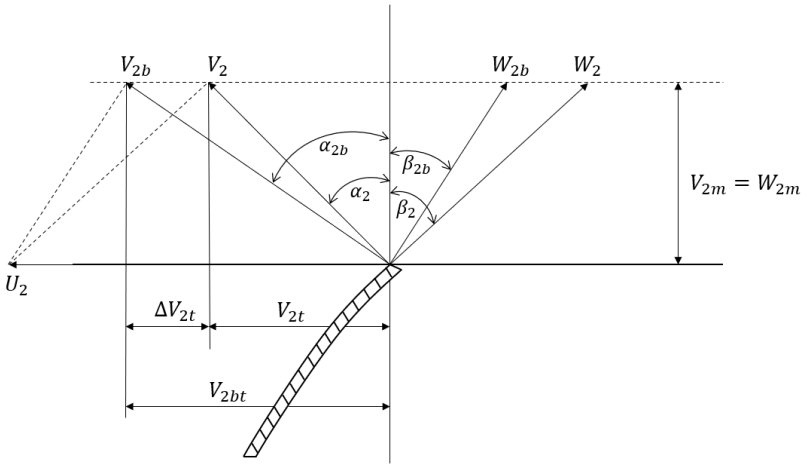

Figure 4.15: A diagram of the exit velocity triangles for a centrifugal compressor showing the slip effect.

V_2 and V_{2t} were obtained from CFD-post as average velocity and average circumferential velocity, respectively. β_{2b} is known from the compressor geometry. U_2 is determined from the rotation speed N and tip radius R_2

$$V_{2t} = V_2 \sin\alpha_2 \rightarrow \alpha_2 = \sin^{-1}\frac{V_{2t}}{V_2} \tag{4.2}$$

$$V_{2m} = V_2 \cos\alpha_2 \tag{4.3}$$

$$V_{2bt} = U_2 + W_{2bt} \tag{4.4}$$

$$W_{2b}\cos\beta_{2b} = V_{2m} \rightarrow W_{2b} = \frac{V_{2m}}{\cos\beta_{2b}} \tag{4.5}$$

$$W_{2bt} = W_{2b}\sin\beta_{2b} \tag{4.6}$$

$$\therefore V_{2bt} = U_2 + \frac{V_{2m}}{\cos\beta_{2b}}\sin\beta_{2b} = U_2 + V_{2m}\tan\beta_{2b} \tag{4.7}$$

$$\sigma = 1 - \frac{V_{2bt} - V_{2t}}{U_2} \tag{4.8}$$

Using these equations, along with the velocities obtained from CFD simulations and the compressor's geometry, it is possible to determine the slip factor distribution for each compressor. This also allows us to construct the velocity triangles at the impeller exit. Shown in Figures 4.16 and 4.17.

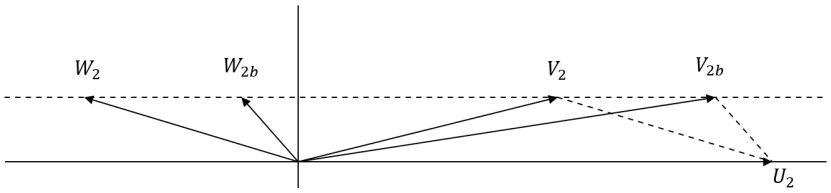

Figure 4.16: Impeller exit velocity diagram for the Radiver compressor at 28,541 RPM and 1 kg/s.

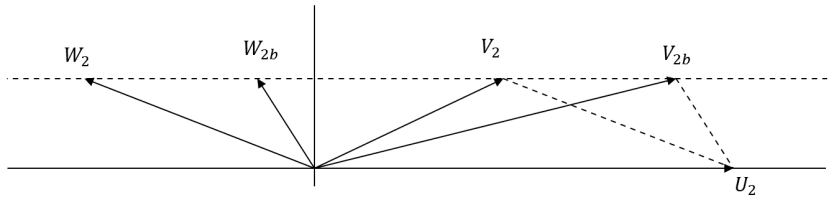

Figure 4.17: Impeller exit velocity diagram for the IRIS compressor at 85,748 RPM and 0.114 kg/s.

Figure 4.18 presents the CFD estimations for the slip factor. There are two observable effects in this figure. The first of which is the wide range of slip factor values that are shown for both compressors. The variance with speed and mass flow is significantly larger than in the Qiu SFM results. This is one indicator for the inaccuracy of estimating slip using CFD, as it is evident from the previous results in this study that compressor geometry is the dominant term in determining the slip factor. The second observation is the average slip factor value for each compressor which is considerably lower than the Qiu SFM predictions. The rotational velocity component U_2 is the same in all cases as it depends on rotational speed N and tip radius R_2. This points to the difference in velocity ΔV_{2t} being the main driver for the discrepancy, with the CFD simulations exhibiting a much larger velocity delta than the Qiu SFM.

While the ROM has separate calculations for slip and losses, it is impossible to isolate the slip effect in CFD simulations completely. The velocity triangle computations are influenced by numerous viscous losses that do not impact the actual slip factor. These losses may contribute to the differences observed in Figure 4.18.

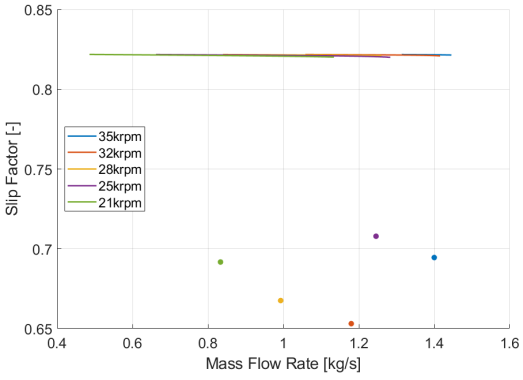

(a) Radiver. Dot markers represent CFD results.

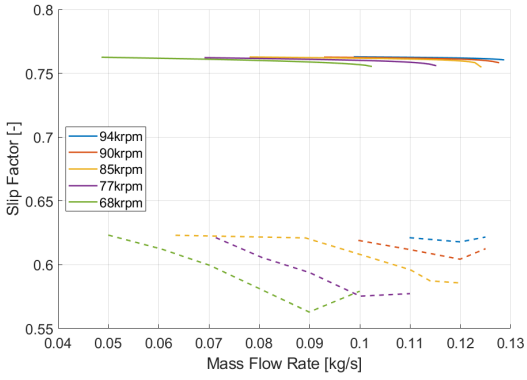

(b) IRIS. Dashed lines represent CFD results.

Figure 4.18: Slip factor estimations for the Radiver and IRIS compressors obtained from the reduced-order model using the Qiu slip model compared to CFD simulation results.

Efficiency

The final aspect of the CFD simulations that was studied were the efficiency calculations. Figure 4.19 shows the efficiency of the Radiver compressor at the 80% speedline, including experimental, reduced-order model, and CFD results.

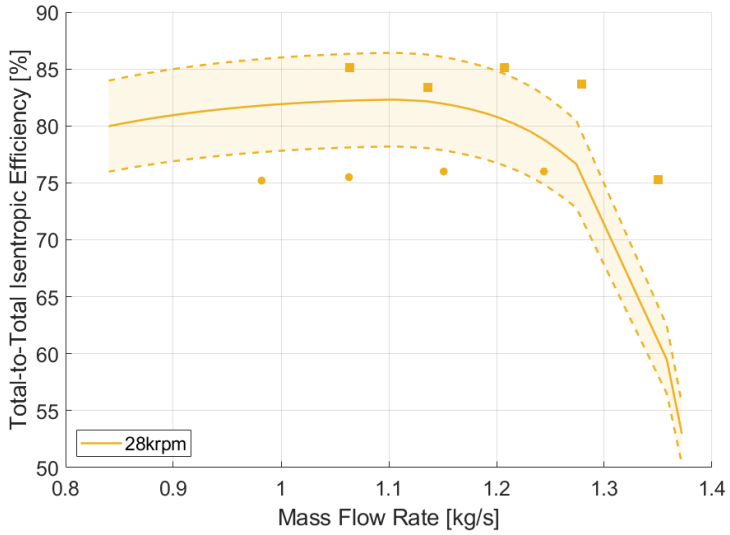

Figure 4.19: Total-to-total isentropic efficiency estimates for the Radiver compressor at 28krpm. Solid lines represent reduced-order model results. Square markers represent CFD results. Dot markers represent experimental results [1].

Figure 4.19 shows relatively good agreement between all three results sources. However, the reduced-order model and, to a larger extent, the CFD simulations have overestimated the compressor's efficiency. The discrepancy may be attributed to the methodology used to calculate efficiency in the literature regarding the Radiver compressor. The efficiency calculation in the original study was based on the efficiency of the impeller, diffuser, and collector. However, this project's reduced-order model or CFD simulations did not consider the collector.

5

Conclusions

For this project, the accuracy of three slip factor models has been assessed, namely, the models proposed by Wiesner, von Backstrom, and Qiu. To determine the accuracy of the models in comparison to experimental results, the slip factor was computed for the IRIS, Radiver, Eckardt, and Schiffmann compressors. These evaluations were performed through an in-house reduced-order model. In addition, CFD simulations were conducted on the IRIS and Radiver cases.

The following conclusions are drawn from the results of this study:

- Slip factor models significantly impact compressor performance predictions during the preliminary design phase. At higher speeds, there can be a difference of up to 20% in the results obtained using different slip factor models.
- The Qiu model showed the highest level of accuracy among the slip factor models tested, particularly at higher compressor speeds. It achieved an average error percentage of 2%.
- The Qiu model's "turning" component allows it to adjust to speed and flow rate changes, setting it apart from other models like von Backstrom and Wiesner, which are constant with changing flow conditions.
- The reduced-order model can accurately predict compressor performance with fewer inputs and is much faster than CFD, making it the ideal choice for slip factor estimation and reducing avenues for errors. CFD simulations on the Radiver compressor had an average percentage error of 8% while the reduced order model using the Qiu slip factor model for the same machine was at only 3%.

6

Recommendations

Based on the outcomes of this study, the following steps are recommended to address:

- Quantifying the effect of compressor speed and mass flow rate on slip estimations. This research has shown that these factors significantly impact slip factor estimations. However, many slip factor models do not consider them. This is especially important considering the recent developments in high-speed compressors going up to and above 200 krpm.
- Validating the reduced-order model and CFD results for the IRIS compressor using the experimental test rig. Pressure ratio and efficiency measurements should be compared with the results presented in this work. This can lead to further improvements in the reduced-order model.
- Exploring the effect of splitter blades on slip estimations. All slip factor models used in this study rely on the number of blades in some form. Also, comparisons of the IRIS and Radiver compressors have shown significant differences in their flow fields at the impeller exit, which are attributed to the presence of splitter blades in the IRIS compressor. An in-depth study on equal machines studying the effect of splitter blades can inform further developments in slip factor modelling.

Bibliography

[1] K. U. Ziegler, H. E. Gallus, and R. Niehuis, *A study on impeller-diffuser interaction—part i: Influence on the performance,* Journal of Turbomachinery **125**, 173 (2003).

[2] K. U. Ziegler, H. E. Gallus, and R. Niehuis, *A study on impeller-diffuser interaction—part ii: Detailed flow analysis,* Journal of Turbomachinery **125**, 183 (2003).

[3] K. U. Ziegler, *Experimentelle untersuchung der laufrad-diffusor-interaktion in einem radialverdichter variabler geometrie* (Shaker, 2003).

[4] A. Giuffre, F. Ascione, C. De Servi, and M. Pini, *Data-Driven Modeling of High-Speed Centrifugal Compressors for Aircraft Environmental Control System* (2022).

[5] A. Giuffre, P. Colonna, and M. Pini, *The effect of size and working fluid on the multi-objective design of high-speed centrifugal compressors,* International Journal of Refrigeration **143**, 43 (2022).

[6] F. J. Wiesner, *A review of slip factors for centrifugal impellers,* Journal of Engineering for Power **89**, 558 (1967).

[7] T. W. von Backström, *A unified correlation for slip factor in centrifugal impellers,* J. Turbomach **128**, 1 (2006).

[8] C. de Servi, *Iris: Inverse organic rankine cycle integrated system,* .

[9] H. M. Harrison, F. Lou, and N. L. Key, *Investigation of slip models for high-speed centrifugal compressors,* Journal of Propulsion and Power **37**, 3 (2021).

[10] A. Giuffre', P. Colonna, and M. Pini, *Design optimization of a high-speed twin-stage compressor for next-gen aircraft environmental control system,* Journal of Engineering for Gas Turbines and Power **145** (2022), 10.1115/1.4056022.

[11] C. Zwyssig, J. W. Kolar, and S. D. Round, *Megaspeed drive systems: Pushing beyond 1 million r/min,* IEEE/ASME Transactions on mechatronics **14**, 564 (2009).

[12] M. Casey, D. Krähenbühl, and C. Zwyssig, *The design of ultra-high-speed miniature centrifugal compressors,* 10th European Conference on Turbomachinery Fluid Dynamics and Thermodynamics, ETC 2013 , 506 (2014).

[13] D. Rusch and M. Casey, *The design space boundaries for high flow capacity centrifugal compressors,* Journal of turbomachinery **135**, 031035 (2013).

[14] F. Ascione, C. M. De Servi, O. Meijer, V. Pommé, and P. Colonna, *Assessment of an inverse organic rankine cycle system for the ecs of a large rotorcraft adopting a high-speed centrifugal compressor and a low gwp refrigerant,* in *Proceedings of the 6th International Seminar on ORC Power Systems*.

[15] C. E. Brennen, *Hydrodynamics of pumps,* (1994).

[16] A. Stodola, *Steam and gas turbines: with a supplement on the prospects of the thermal prime mover*, Vol. 2 (McGraw-Hill, 1927).

[17] A. Busemann, *Das förderhöhenverhältnis radialer kreiselpumpen mit logarithmisch□spiraligen schaufeln,* ZAMM□Journal of Applied Mathematics and Mechanics/Zeitschrift für Angewandte Mathematik und Mechanik **8**, 372 (1928).

[18] J. Stanitz, *Some theoretical aerodynamic investigations of impellers in radial-and mixed-flow centrifugal compressors,* Transactions of the American Society of Mechanical Engineers **74**, 473 (1952).

[19] X. Qiu and et al., *Analysis and validation of a unified slip factor model for impellers at design and off-design conditions,* Journal of Turbomachinery **133**, 041018 (2011).

[20] A. Whitfield, *Slip factor of a centrifugal compressor and its variation with flow rate,* Proceedings of the Institution of Mechanical Engineers **188**, 415 (1974).

[21] M. Waesker, T. Goetz, B. Bülten, and N. Kienzle, *Analysis of slip factors in CFD calculations – Assessment of literature models* (2021).

[22] C. Stuart, S. Spence, D. Filsinger, A. Starke, and S. I. Kim, *A three-zone modeling approach for centrifugal compressor slip factor prediction,* Journal of Turbomachinery **141** (2019).

[23] E. W. Lemmon, I. H. Bell, M. Huber, and M. McLinden, *Nist standard reference database 23: reference fluid thermodynamic and transport properties-refprop, version 10.0, national institute of standards and technology,* Standard Reference Data Program, Gaithersburg (2018).

[24] D. Eckardt, *Investigation of the jet-wake flow of a highly loaded centrifugal compressor impeller*, Report (1978).

[25] D. Japikse, *A critical evaluation of three centrifugal compressors with pedigree data sets: Part 5—studies in component performance,* (1987).

[26] J. Schiffmann and D. Favrat, *Design, experimental investigation and multi-objective optimization of a small-scale radial compressor for heat pump applications,* Energy **35**, 436 (2010).

A

TurboSim Code Extract

```
        """
        compute the slip factor based on the prescribed slip model
        """
        if self.flag_slip == 'backstrom':
            self.sigma = 1 - 1 / (1 + self.F0 * np.mean(self.solidity) * np.sqrt(np.cos(self.
                                                    beta_blade[1, :])))

        elif self.flag_slip == 'wiesner':
            self.sigma = 1 - (np.sqrt(np.cos(self.beta_blade[1, :])) / (self.Neff ** 0.7))

        elif self.flag_slip == 'qiu':
            shape = 1 - (2 * np.sin(np.pi / self.Neff) * np.sin((np.pi / self.Neff) + self.
                                                    beta_blade[1, :]) *
                         np.cos(self.beta_blade[1, :])) - (self.t_te / (self.pitch * np.cos(
                                                    self.beta_blade[1, :]
                                                    )))

            # if x_mid, y_mid, blade_to_blade are still zeros, use simplified expression
            if sum(self.x_mid) == 0:
                self.sigma = 1 - ((shape * np.pi * np.cos(self.beta_blade[1, :])) / self.Neff
                                                    )
            else:
                end = np.size(self.x_mid)
                a = np.array([self.x_mid[end - 1 - int(end / 2)], self.y_mid[end - 1 - int(
                                                    end / 2)]])
                b = np.array([self.x_mid[end - 2 - int(end / 2)], self.y_mid[end - 2 - int(
                                                    end / 2)]])
                dist = np.linalg.norm(a - b)
                blade_turning = self.blade_to_blade.beta_blade[:, int(end / 2) - 1] - \
                    self.blade_to_blade.beta_blade[:, int(end / 2) - 2]
                turning = blade_turning / dist
                self.sigma = 1 - ((shape * np.pi * np.cos(self.beta_blade[1, :])) / self.Neff
                                                    ) - \
                    (shape * self.pitch * self.Vm[1, :] / self.U[1, :] / (4 * np.cos(self.
                                                        beta_blade[1, :]))) *
                                                        turning

        else:
            raise NotImplementedError("The available choices for slip model are 'backstrom',
                                                    'wiesner', or 'qiu'")
```

B

CFD Parametrisation

Table of Design Points

	A	B	C	D	E	F	G	H	I	J	K	L
1	Name	Update Order	P4 - MFlow	P5 - Speed	P9 - Mass Flow	P10 - Percent Speed	P13 - TimeS...	P6 - PR	P8 - Eff	P12 - MFlow	Ret...	Retained Data
2	Units		kg s^-1	radian s^-1	kg s^-1		s radian^-1			kg s^-1		
9	DP 19 (Current)	7	0.9929	2988.8	0.9929	80	3.3458E-05	2.7053	83.062	0.9929	☑	✓
10	DP 41	8	1	2241.6	1	60	4.4611E-05	1.6348	81.326	1	☐	
11	DP 31	9	1.0222	2615.2	1.0222	70	3.8238E-05	2.0756	83.061	1.0222	☐	
12	DP 20	10	1.0643	2988.8	1.0643	80	3.3458E-05	2.6811	85.137	1.0643	☐	
13	DP 42	11	1.0833	2241.6	1.0833	60	4.4611E-05	1.5792	79.269	1.0833	☐	
14	DP 32	12	1.0967	2615.2	1.0967	70	3.8238E-05	2.0183	82.706	1.0967	☐	
15	DP 21	13	1.1357	2988.8	1.1357	80	3.3458E-05	2.6114	83.411	1.1357	☐	
16	DP 43	14	1.1667	2241.6	1.1667	60	4.4611E-05	1.5153	78.049	1.1667	☐	
17	DP 33	15	1.1711	2615.2	1.1711	70	3.8238E-05	⚡	⚡	⚡	☐	
18	DP 15	16	1.18	3362.4	1.18	90	2.9741E-05	⚡	⚡	⚡	☐	
19	DP 22	17	1.2071	2988.8	1.2071	80	3.3458E-05	⚡	⚡	⚡	☐	
20	DP 34	18	1.2456	2615.2	1.2456	70	3.8238E-05	⚡	⚡	⚡	☐	
21	DP 44	19	1.25	2241.6	1.25	60	4.4611E-05	⚡	⚡	⚡	☐	
22	DP 16	20	1.27	3362.4	1.27	90	2.9741E-05	⚡	⚡	⚡	☐	
23	DP 23	21	1.2786	2988.8	1.2786	80	3.3458E-05	⚡	⚡	⚡	☐	
24	DP 10	22	1.316	3736	1.316	100	2.6767E-05	⚡	⚡	⚡	☐	
25	DP 35	23	1.32	2615.2	1.32	70	3.8238E-05	⚡	⚡	⚡	☐	
26	DP 24	24	1.35	2988.8	1.35	80	3.3458E-05	⚡	⚡	⚡	☐	
27	DP 17	25	1.36	3362.4	1.36	90	2.9741E-05	⚡	⚡	⚡	☐	
28	DP 11	26	1.372	3736	1.372	100	2.6767E-05	⚡	⚡	⚡	☐	
29	DP 4	27	1.4	3736	1.4	100	2.6767E-05	⚡	⚡	⚡	☐	
30	DP 12	28	1.428	3736	1.428	100	2.6767E-05	⚡	⚡	⚡	☐	
31	DP 18	29	1.45	3362.4	1.45	90	2.9741E-05	⚡	⚡	⚡	☐	
32	DP 13	30	1.484	3736	1.484	100	2.6767E-05	⚡	⚡	⚡	☐	
33	DP 14	31	1.54	3736	1.54	100	2.6767E-05	⚡	⚡	⚡	☐	
*											☐	

Figure B.1: Screenshot of the parameter view in Ansys Workbench used in this study.

C

Additional Results

C.1. ROM Results

Reduced-order model results in this section were obtained using the Qiu slip model.

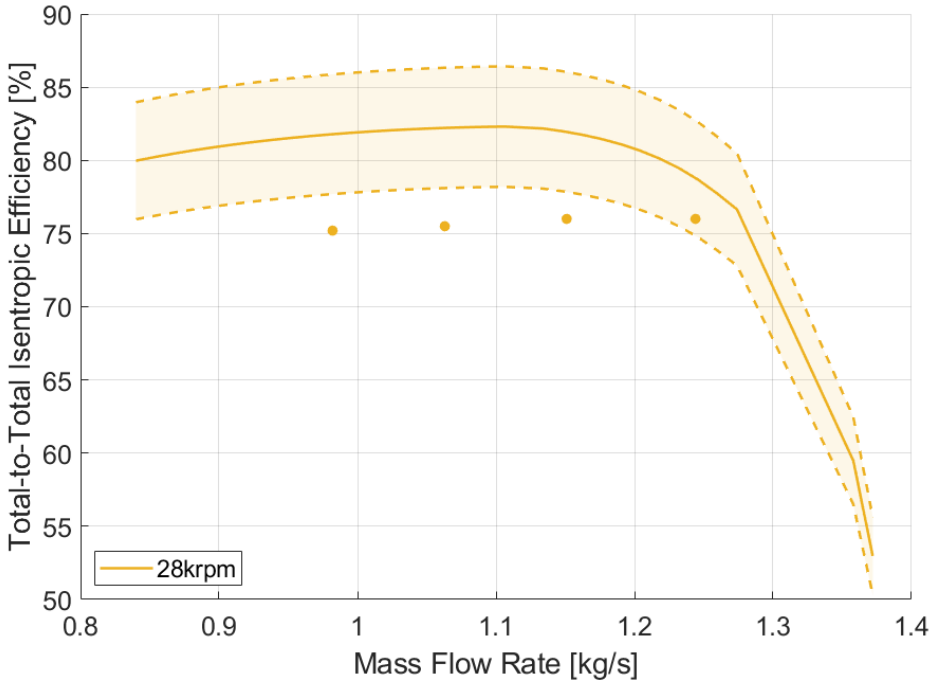

Figure C.1: Total-to-total isentropic efficiency estimates for the MTU compressor at 28krpm. The solid line represents reduced-order model results. Dot markers represent experimental results [1].

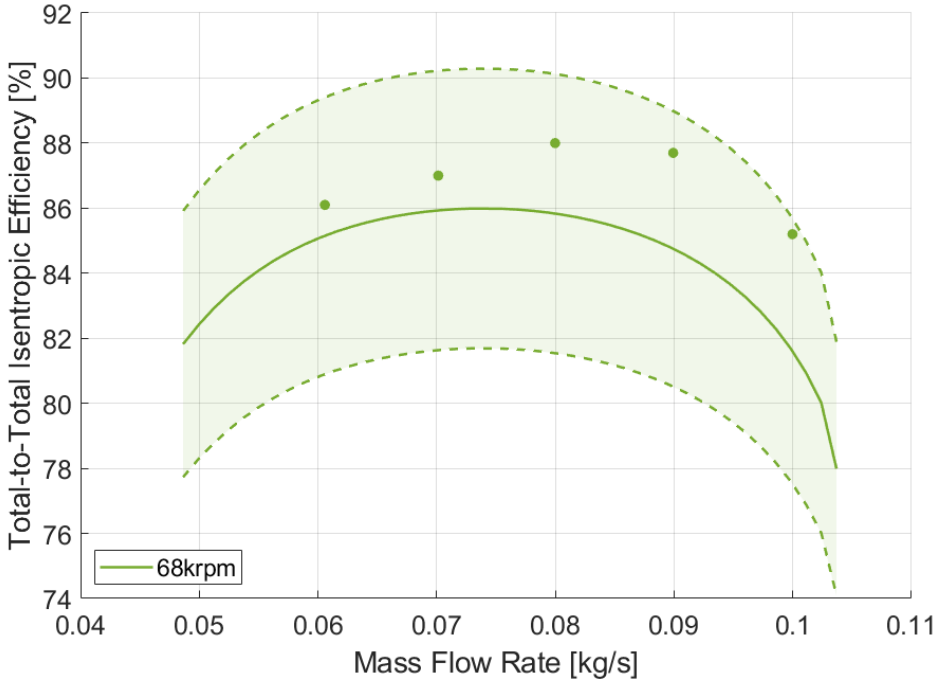

Figure C.2: Total-to-total isentropic efficiency estimates for the IRIS compressor at 68krpm. The solid line represents reduced-order model results. Dot markers represent CFD results [5].

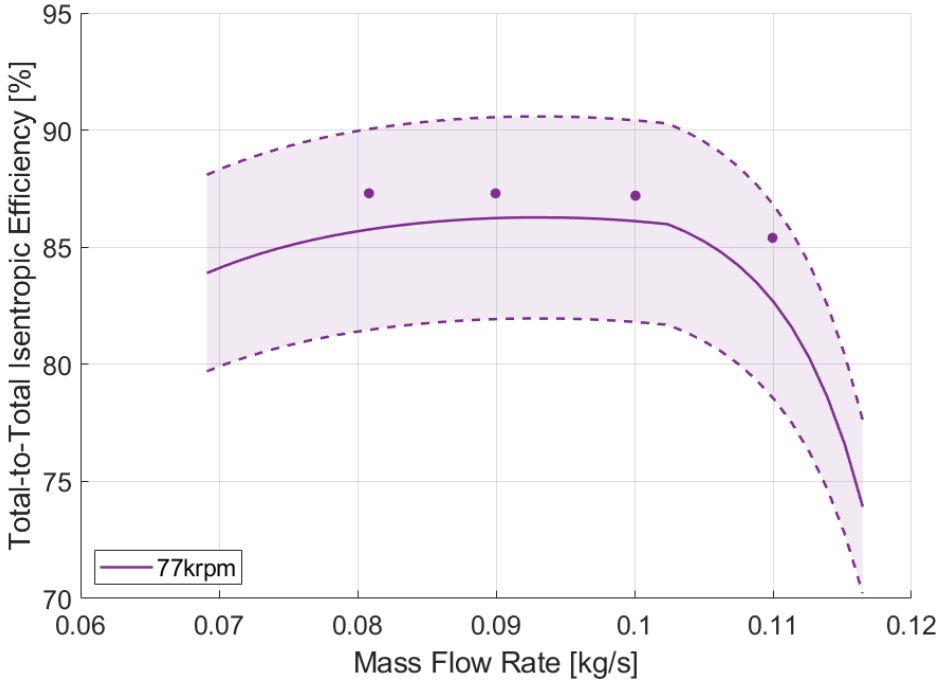

Figure C.3: Total-to-total isentropic efficiency estimates for the IRIS compressor at 77krpm. The solid line represents reduced-order model results. Dot markers represent CFD results [5].

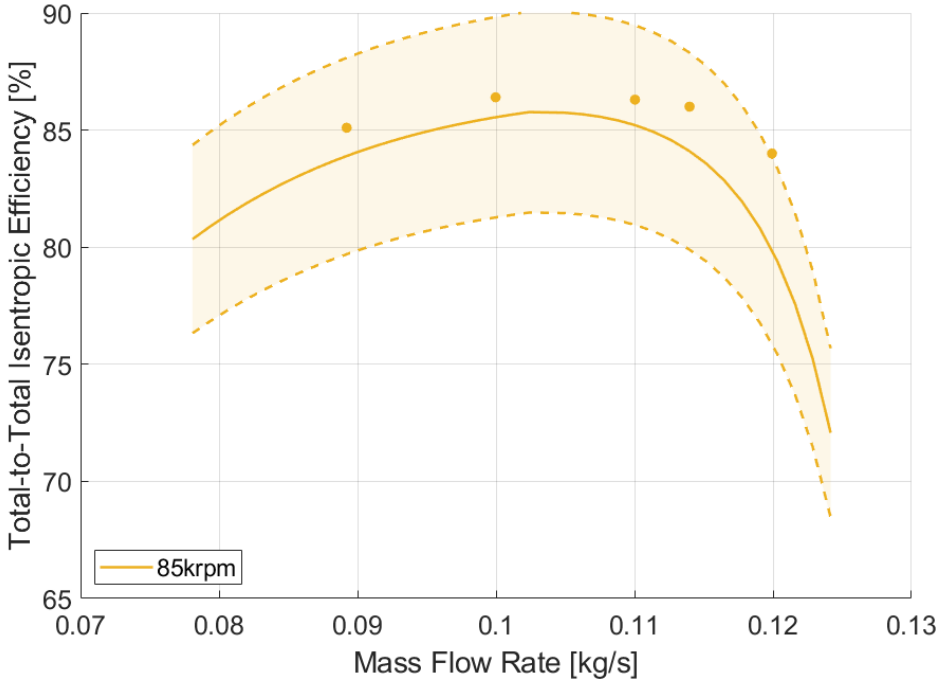

Figure C.4: Total-to-total isentropic efficiency estimates for the IRIS compressor at 85krpm. The solid line represents reduced-order model results. Dot markers represent CFD results [5].

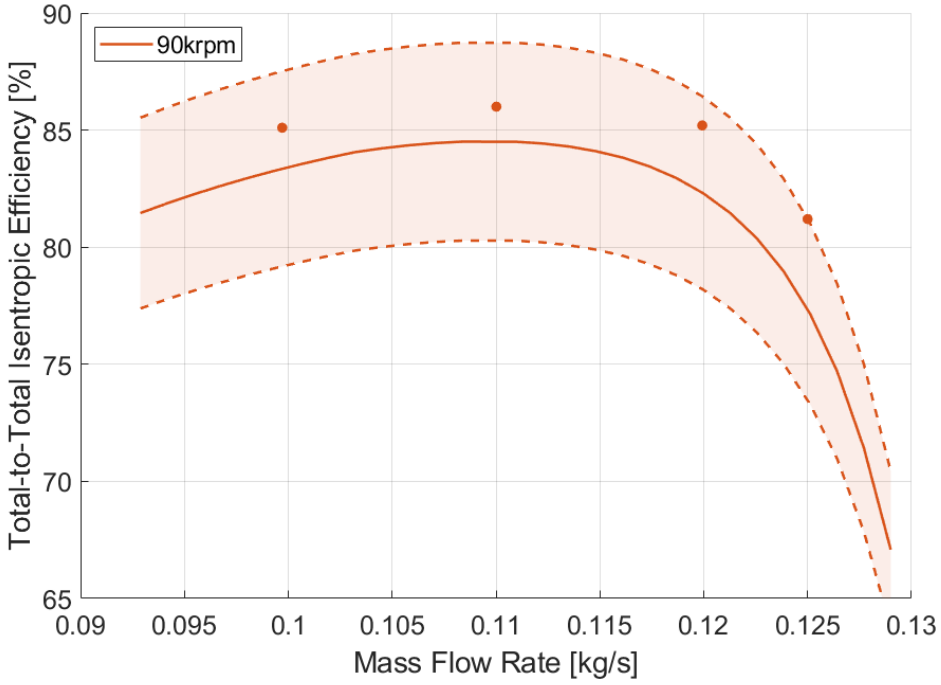

Figure C.5: Total-to-total isentropic efficiency estimates for the IRIS compressor at 90krpm. The solid line represents reduced-order model results. Dot markers represent CFD results [5].

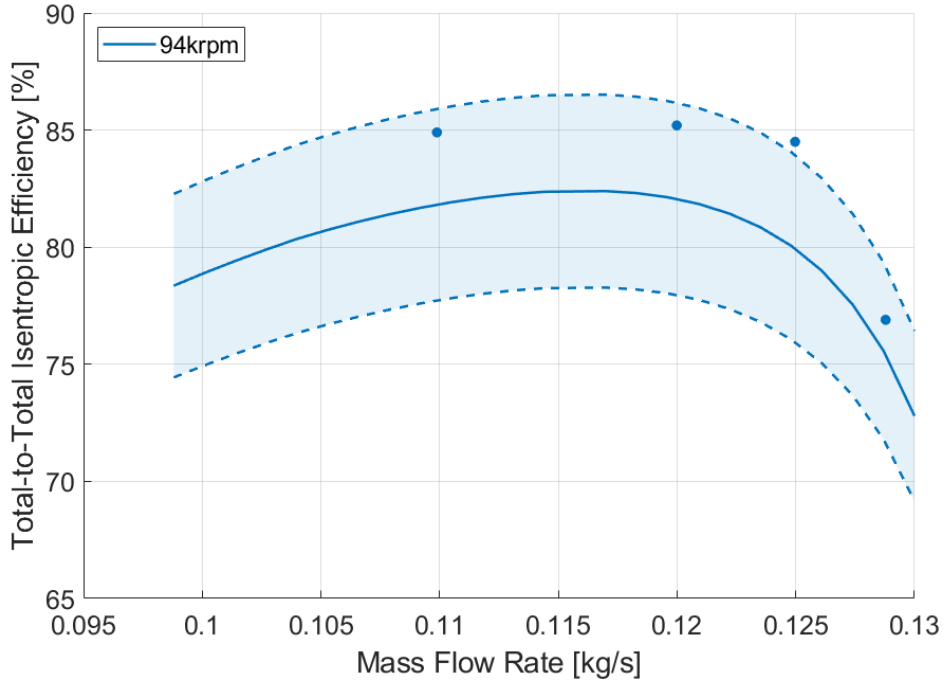

Figure C.6: Total-to-total isentropic efficiency estimates for the IRIS compressor at 94krpm. The solid line represents reduced-order model results. Dot markers represent CFD results [5].

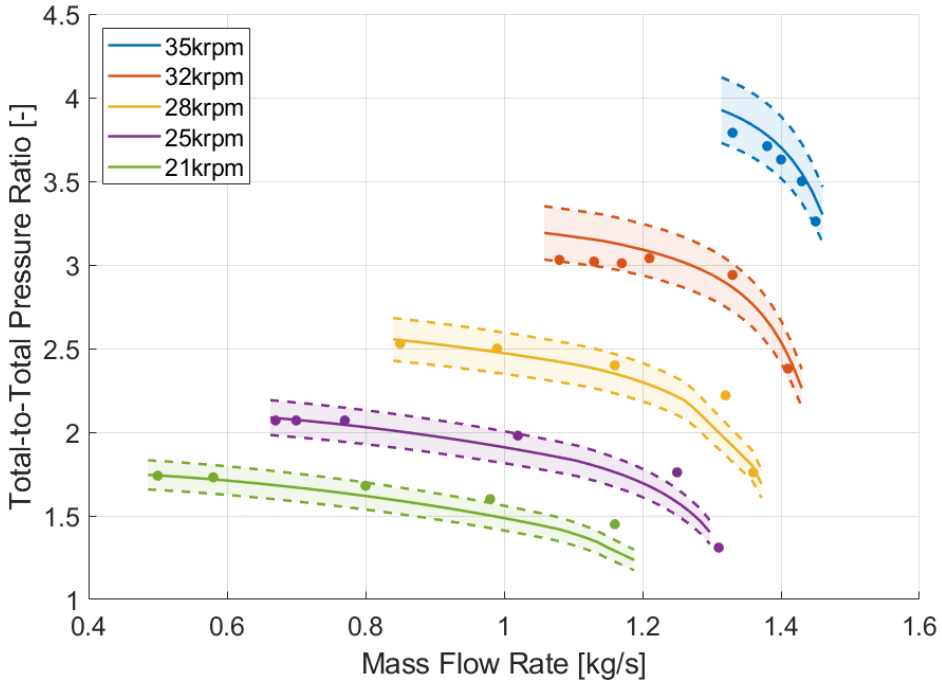

Figure C.7: Operating map for the Radiver compressor. The solid line represents reduced-order model results. Dot markers represent experimental results [1].

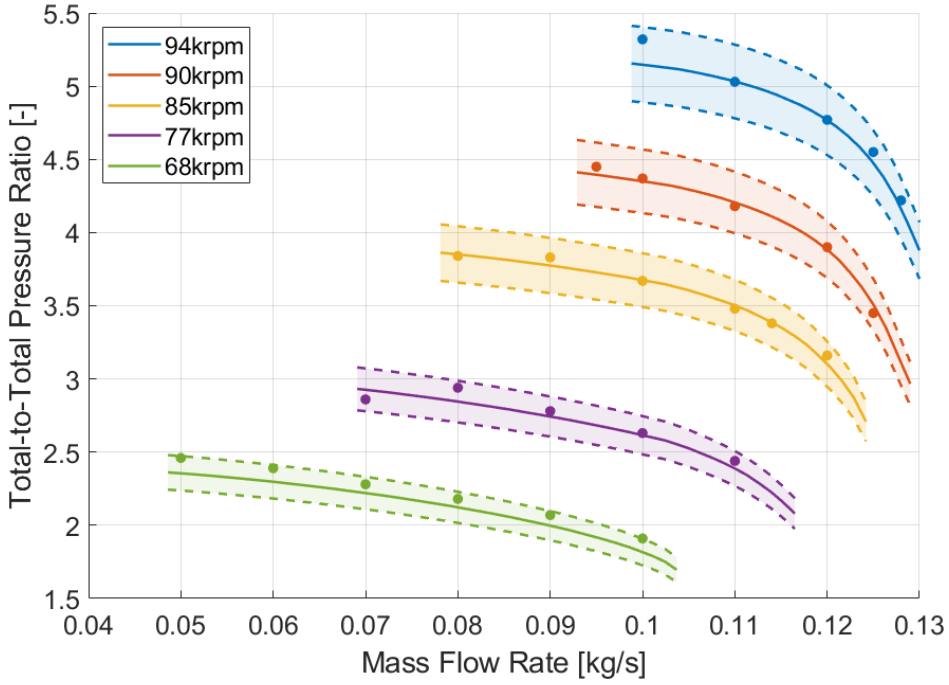

Figure C.8: Operating map for the IRIS compressor. The solid line represents reduced-order model results. Dot markers represent CFD results [5].

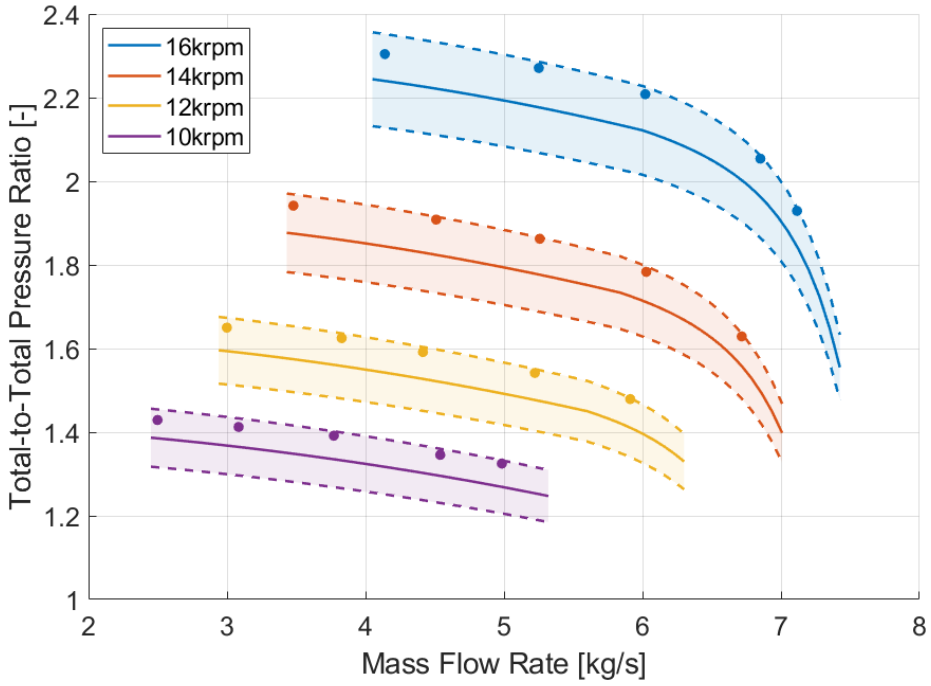

Figure C.9: Operating map for the Eckardt A compressor. The solid line represents reduced-order model results. Dot markers represent Experimental results [24].

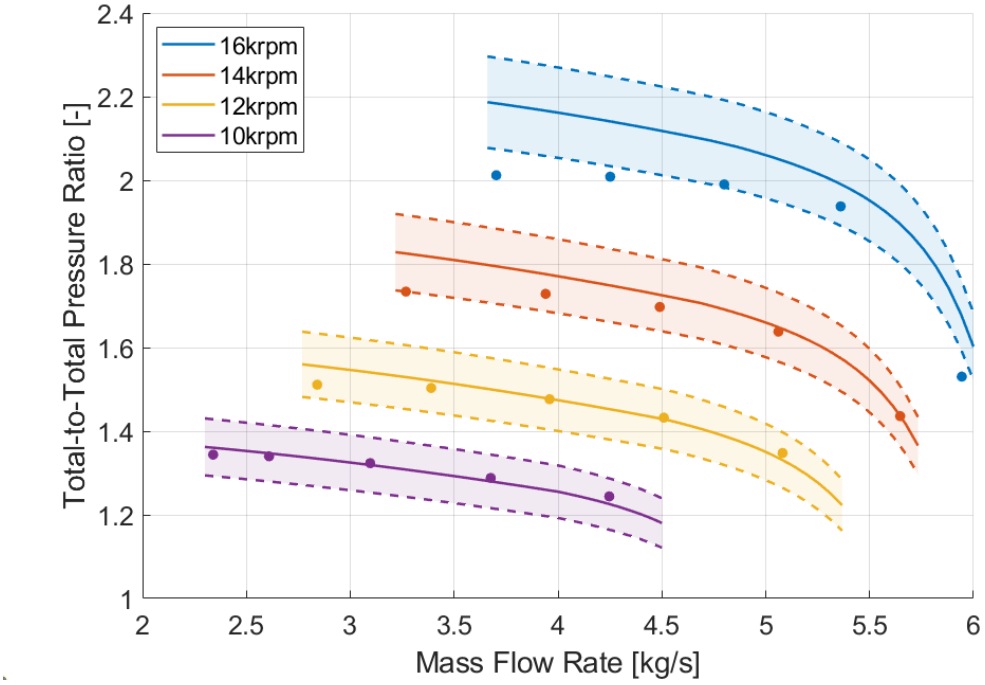

Figure C.10: Operating map for the Eckardt B compressor. The solid line represents reduced-order model results. Dot markers represent Experimental results [24].

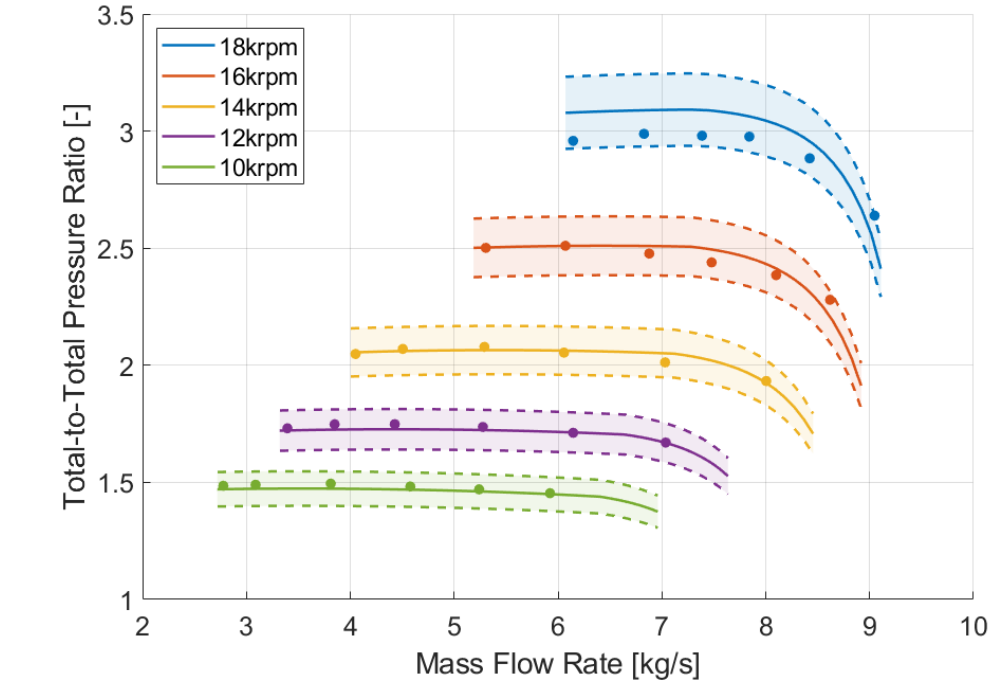

Figure C.11: Operating map for the Eckardt O compressor. The solid line represents reduced-order model results. Dot markers represent Experimental results [24].

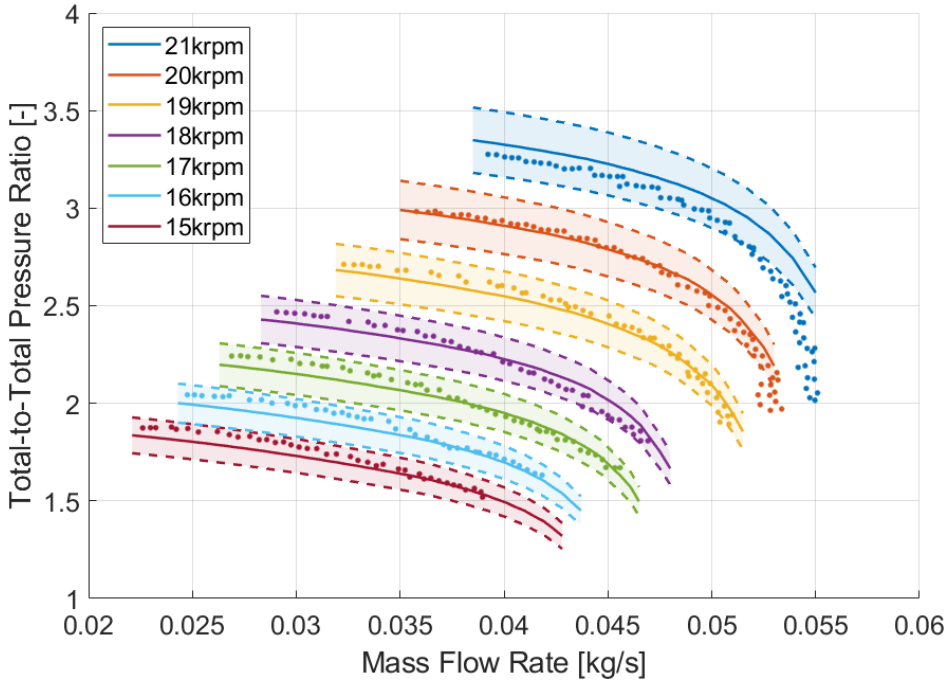

Figure C.12: Operating map for the Schiffmann compressor. The solid line represents reduced-order model results. Dot markers represent Experimental results [26].

C.2. Slip Model Comparisons

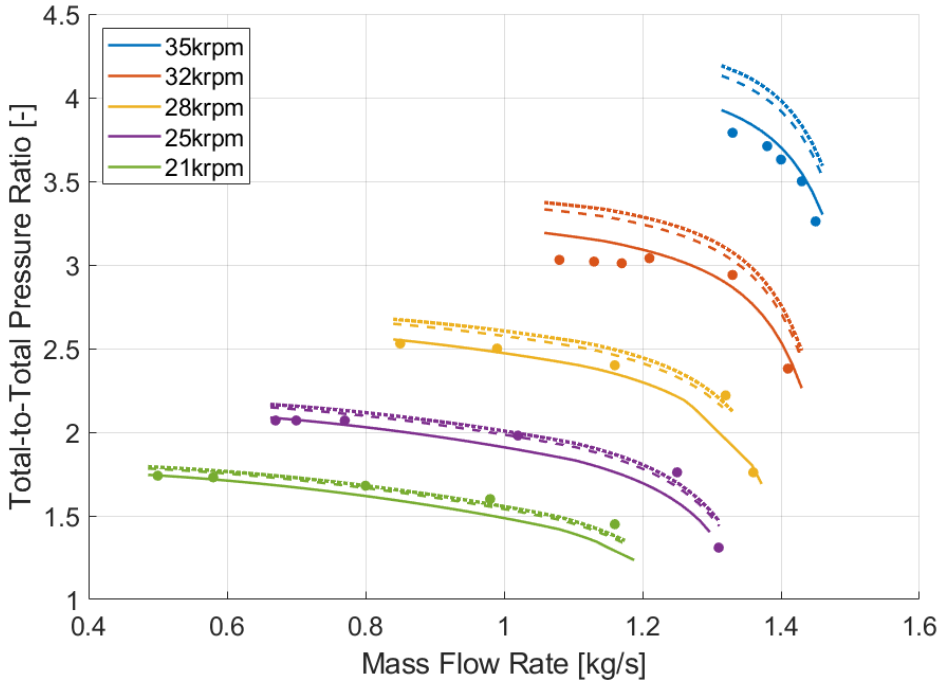

Figure C.13: Operating map for the Radiver compressor. The solid line represents reduced-order model results. Dot markers represent experimental results [1]. Slip models: solid - Qiu, dashed - von Backstrom, dotted - Wiesner.

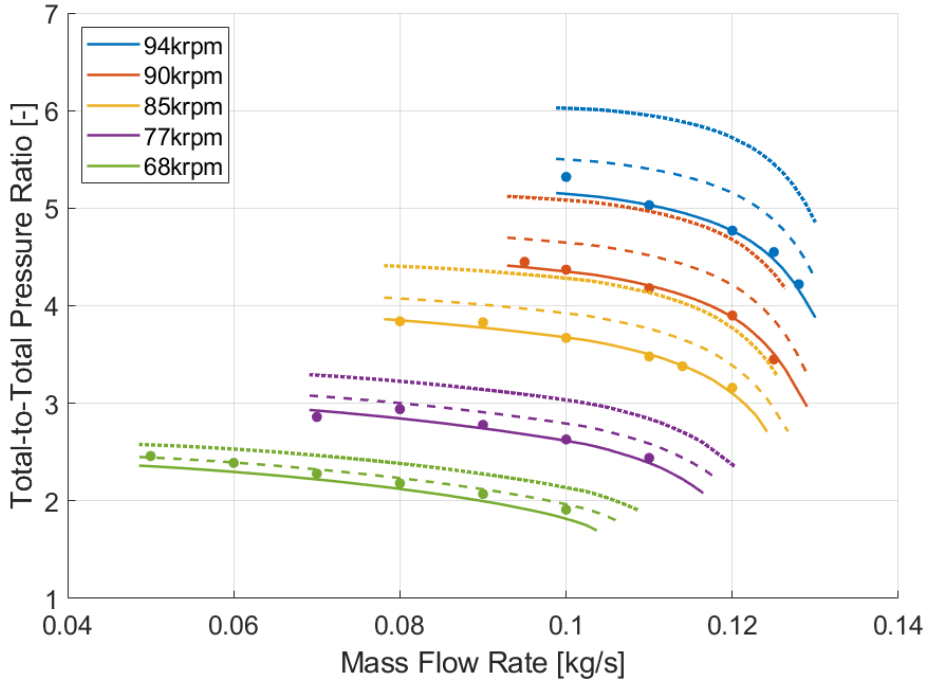

Figure C.14: Operating map for the IRIS compressor. The solid line represents reduced-order model results. Dot markers represent CFD results [5]. Slip models: solid - Qiu, dashed - von Backstrom, dotted - Wiesner.

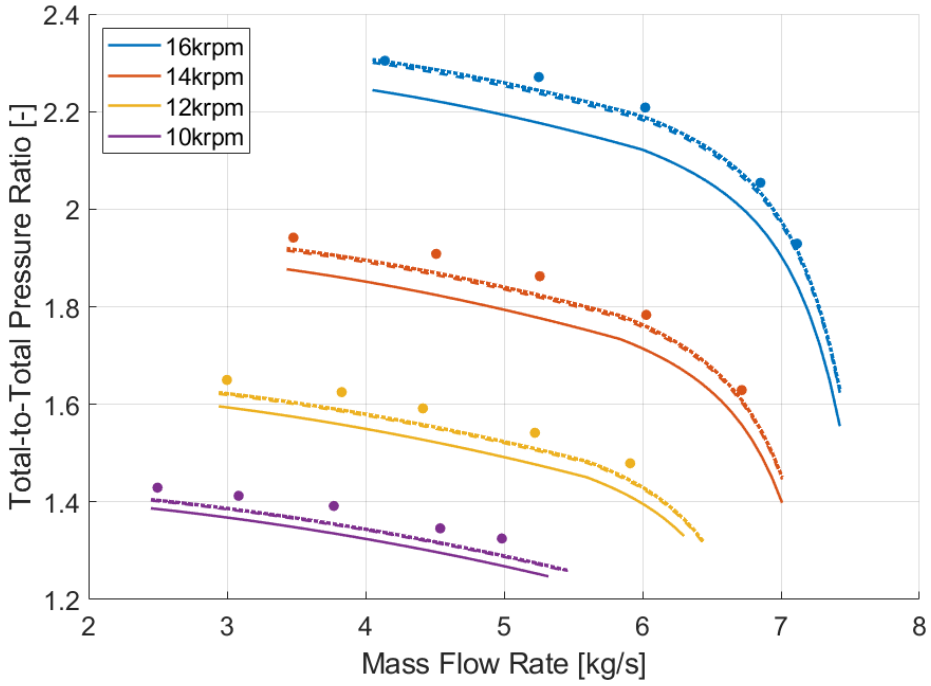

Figure C.15: Operating map for the Eckardt A compressor. The solid line represents reduced-order model results. Dot markers represent Experimental results [24][25]. Slip models: solid - Qiu, dashed - von Backstrom, dotted - Wiesner.

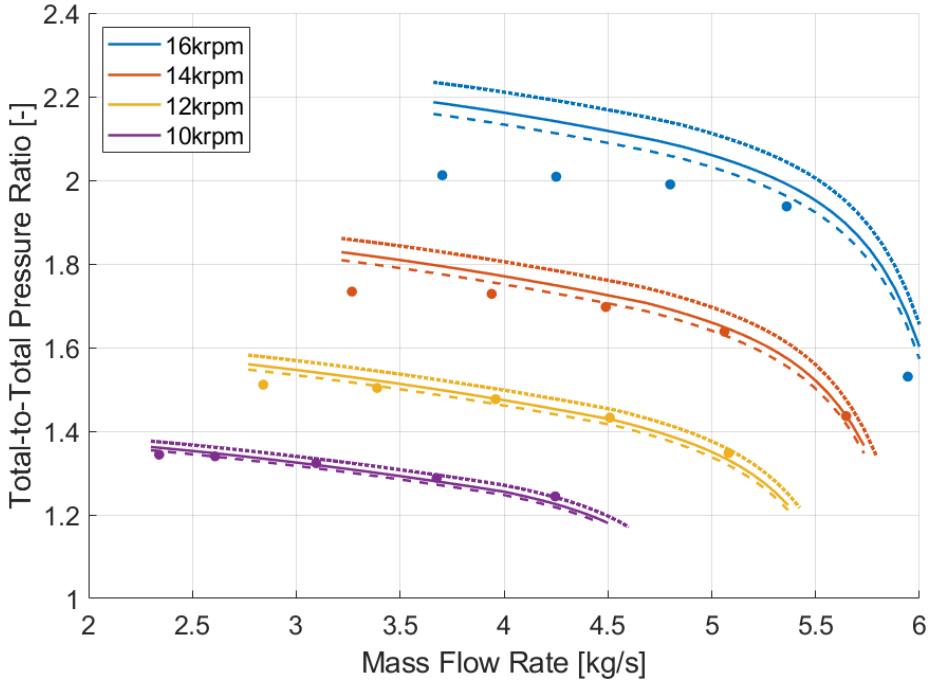

Figure C.16: Operating map for the Eckardt B compressor. The solid line represents reduced-order model results. Dot markers represent Experimental results [24][25]. Slip models: solid - Qiu, dashed - von Backstrom, dotted - Wiesner.

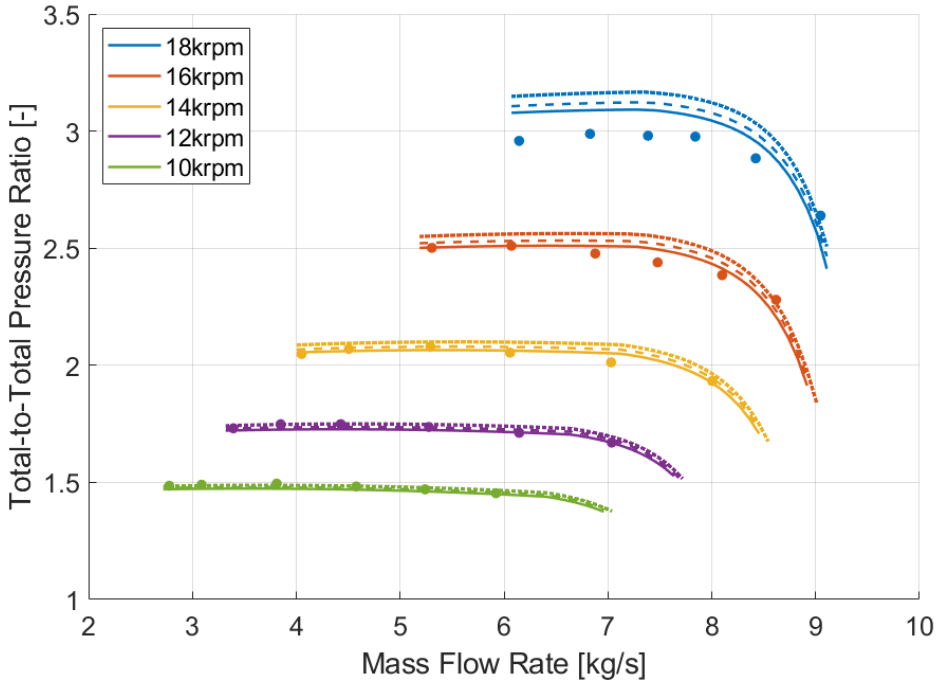

Figure C.17: Operating map for the Eckardt O compressor. The solid line represents reduced-order model results. Dot markers represent Experimental results [24][25]. Slip models: solid - Qiu, dashed - von Backstrom, dotted - Wiesner.

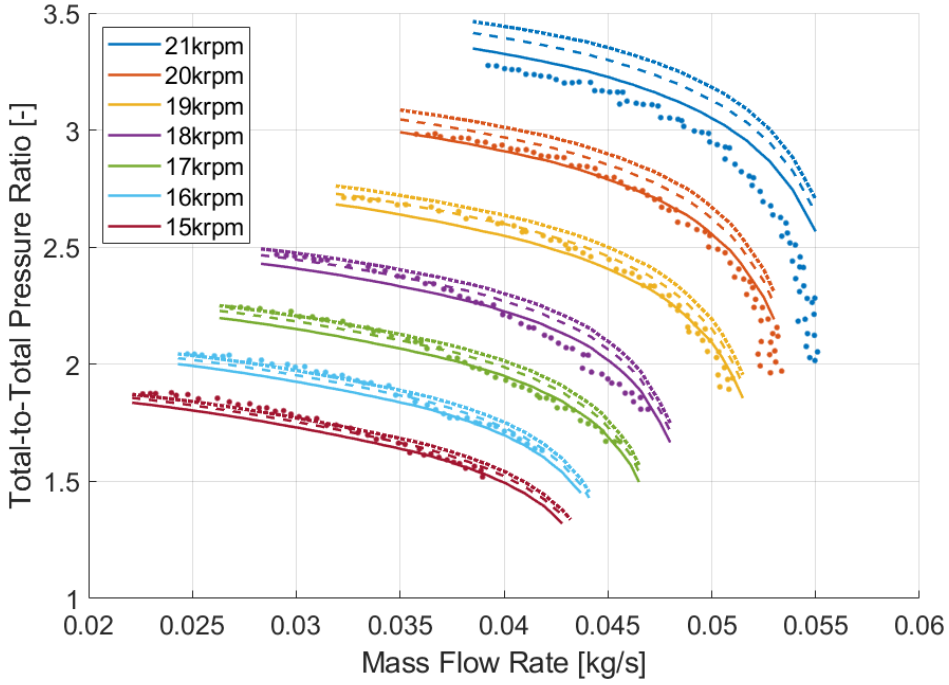

Figure C.18: Operating map for the Schiffmann compressor. The solid line represents reduced-order model results. Dot markers represent Experimental results [26]. Slip models: solid - Qiu, dashed - von Backstrom, dotted - Wiesner.

C.3. CFD Simulation Results

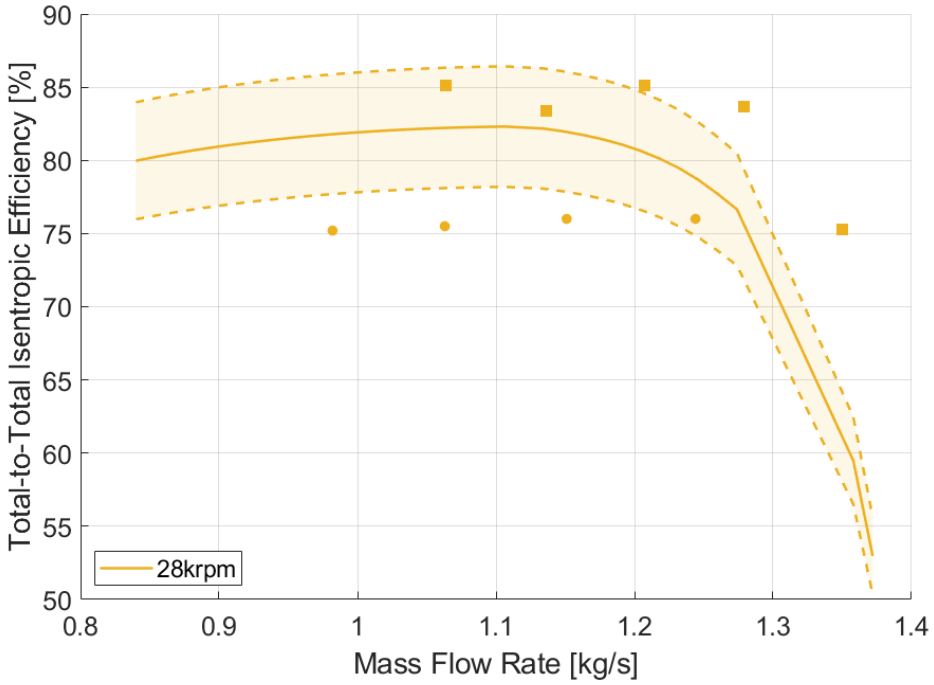

Figure C.19: Operating map for the Radiver compressor. The solid line represents reduced-order model results. Dot markers represent experimental results [1]. Square markers represent CFD results.

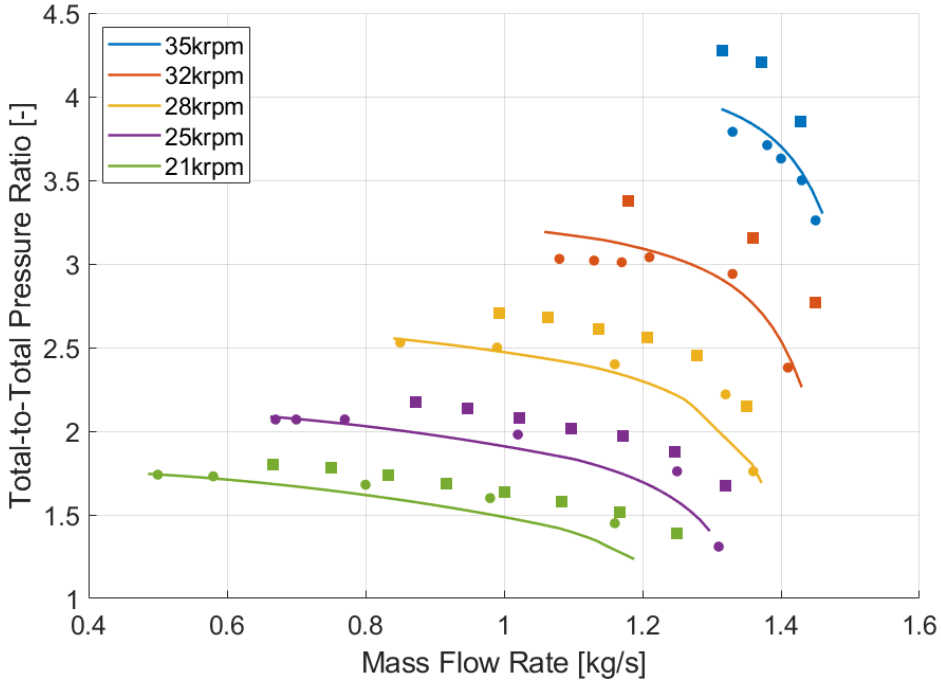

Figure C.20: Operating map for the Radiver compressor. The solid line represents reduced-order model results. Dot markers represent experimental results [1]. Square markers represent CFD results.

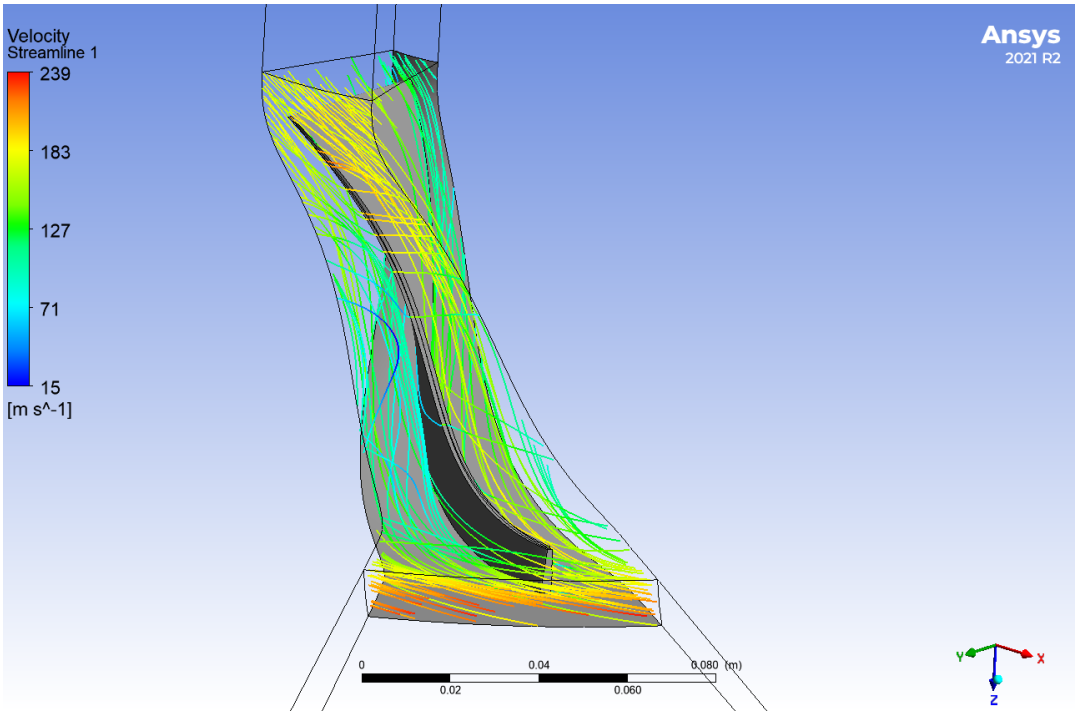

Figure C.21: Velocity streamlines through the blade passage of the Radiver compressor at 21,406 RPM and 0.83 kg/s.

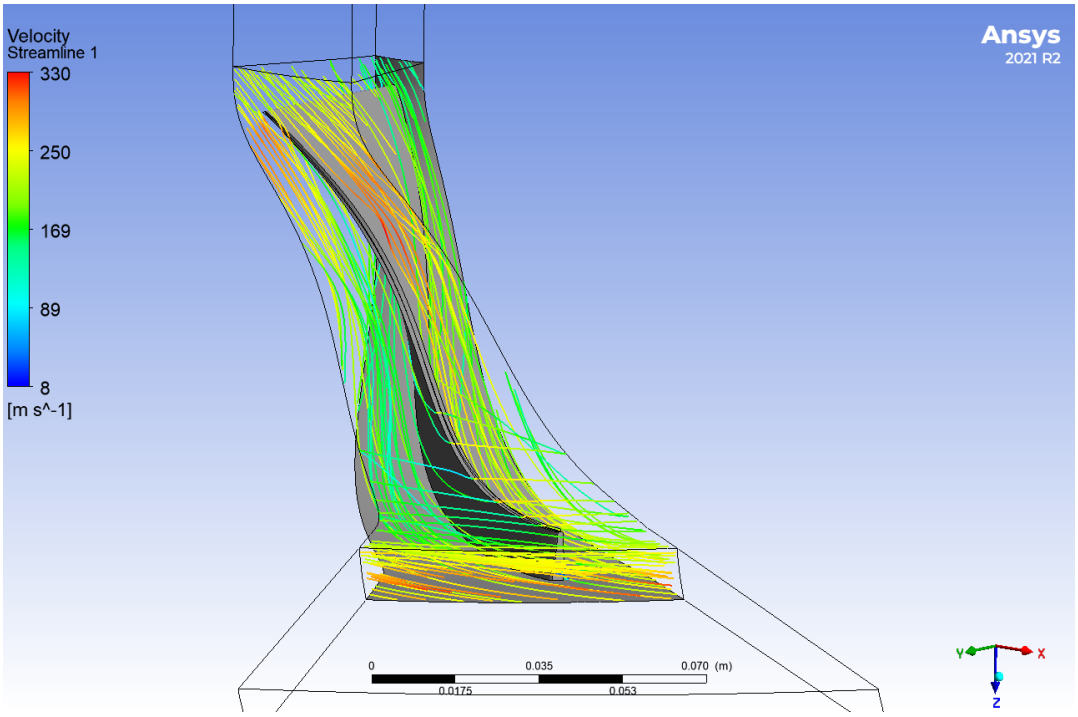

Figure C.22: Velocity streamlines through the blade passage of the Radiver compressor at 24,973 RPM and 1.25 kg/s.

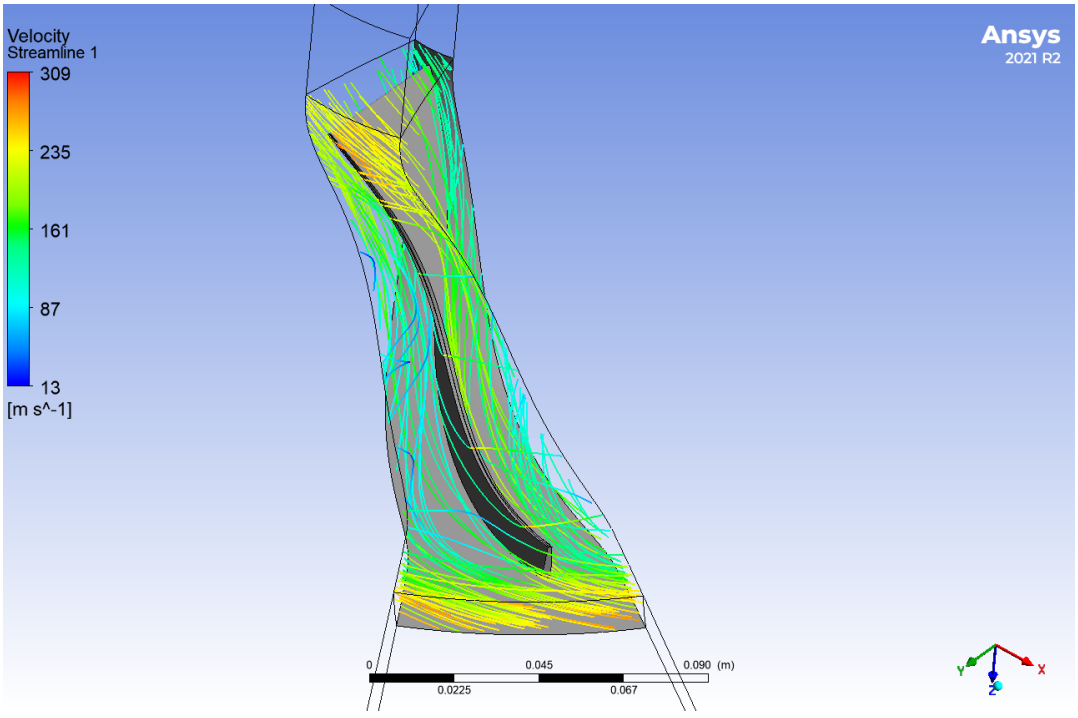

Figure C.23: Velocity streamlines through the blade passage of the Radiver compressor at 28,541 RPM and 1 kg/s.

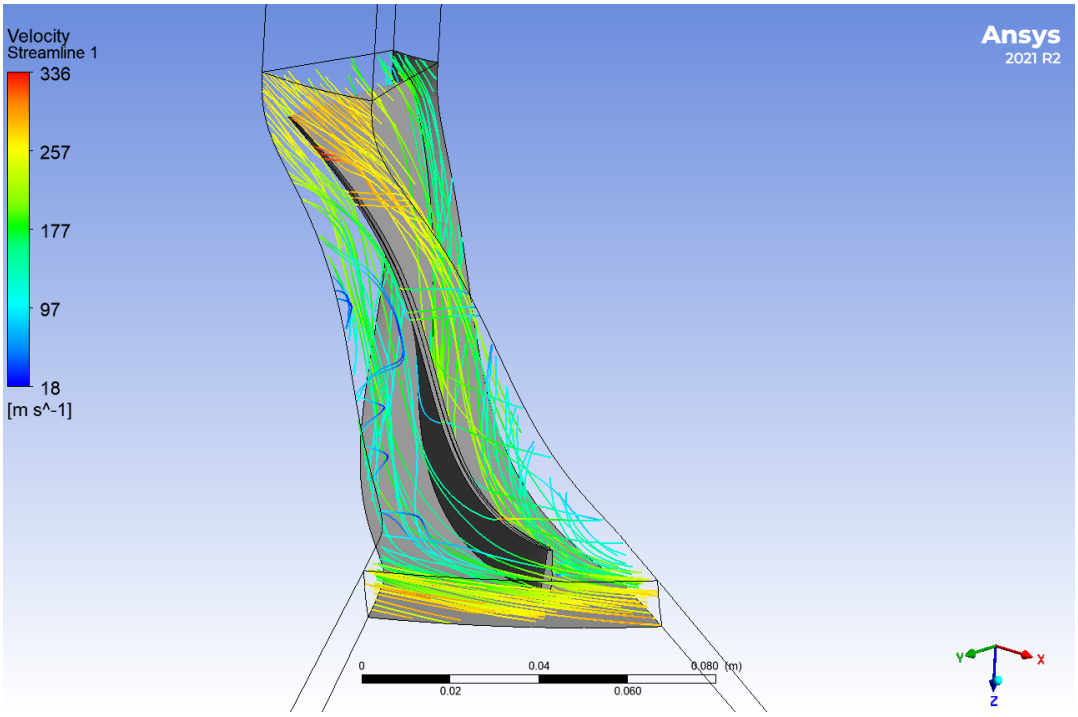

Figure C.24: Velocity streamlines through the blade passage of the Radiver compressor at 32,108 RPM and 1.18 kg/s.

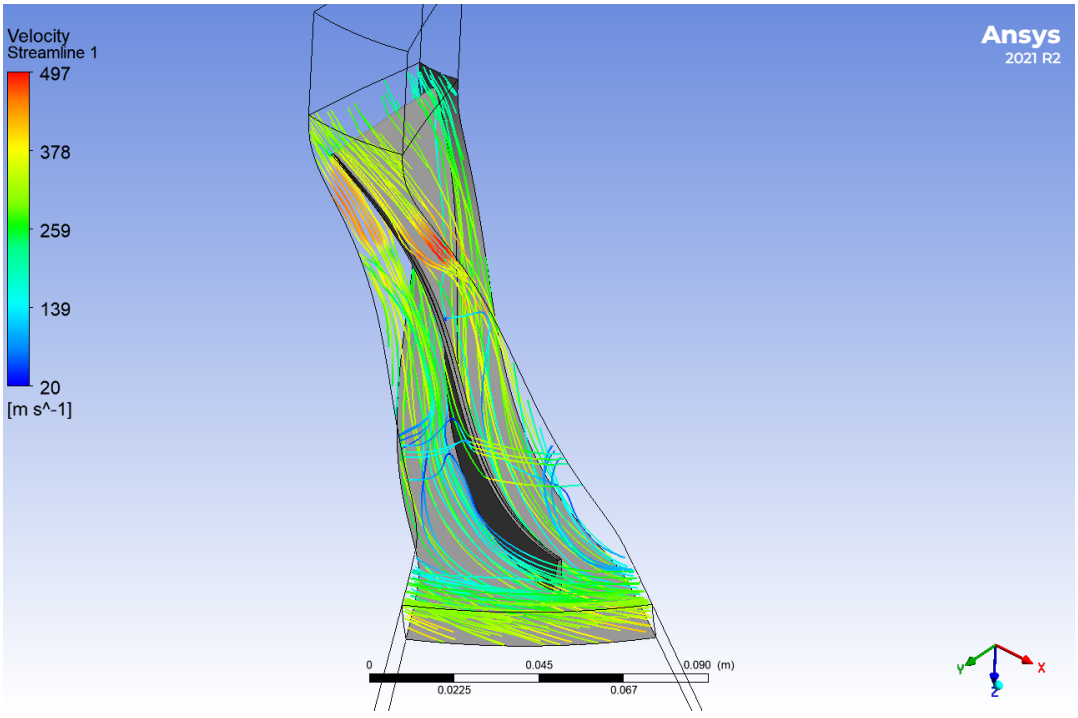

Figure C.25: Velocity streamlines through the blade passage of the Radiver compressor at 35,676 RPM and 1.4 kg/s.

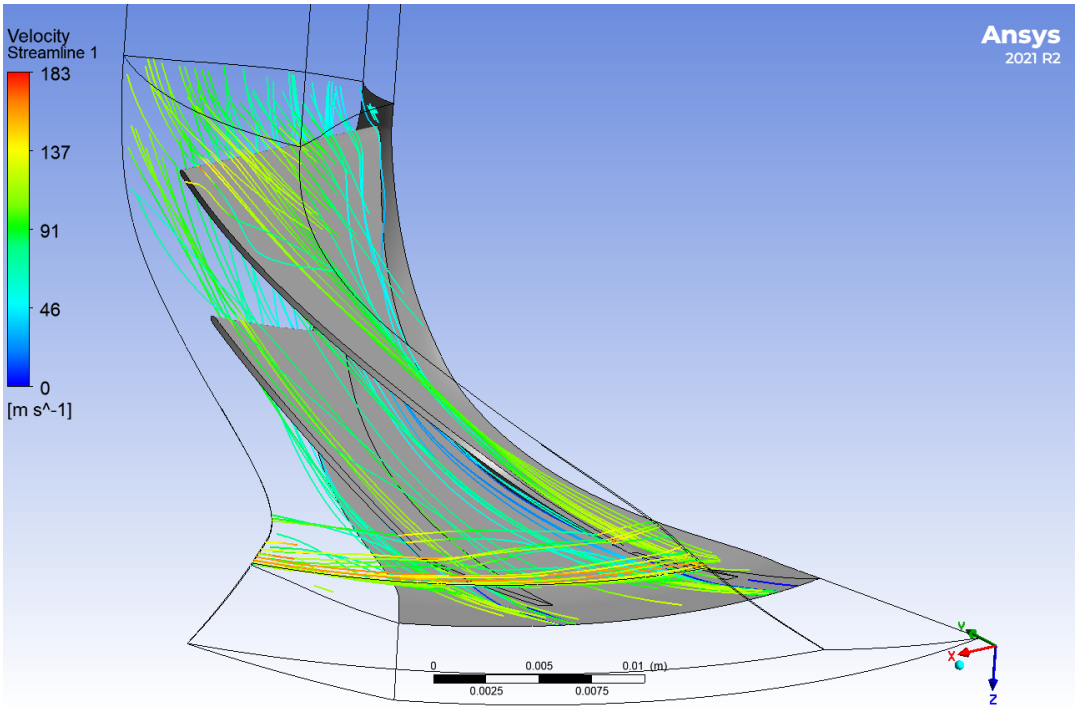

Figure C.26: Velocity streamlines through the blade passage of the IRIS compressor at 68,598 RPM and 0.08 kg/s.

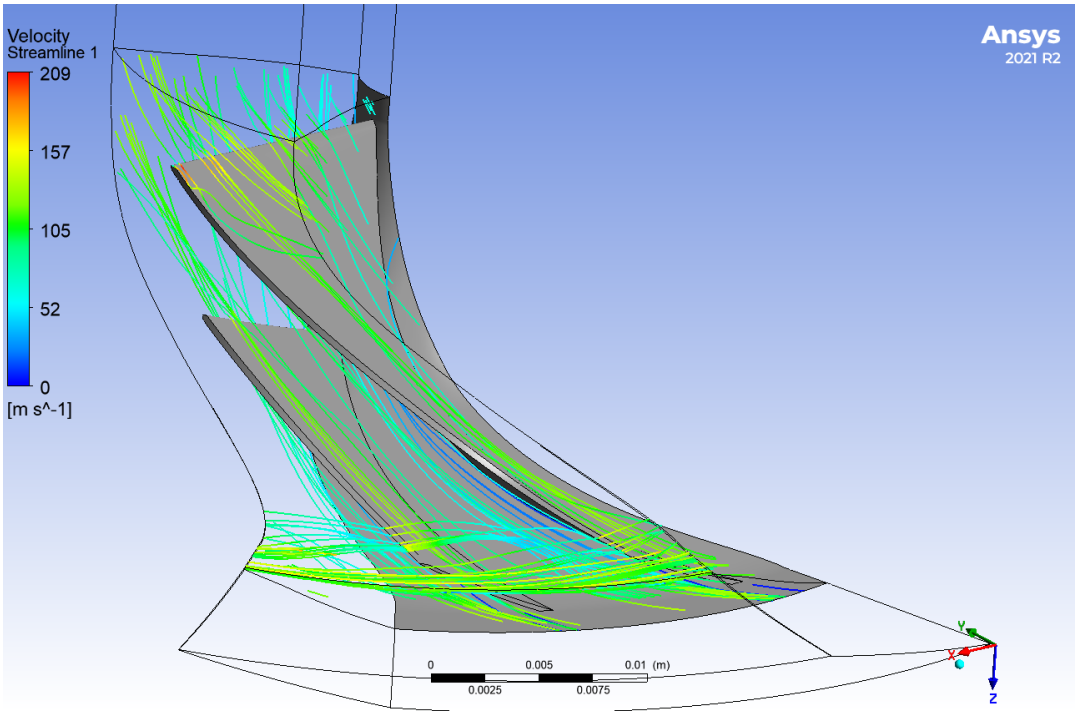

Figure C.27: Velocity streamlines through the blade passage of the IRIS compressor at 77,173 RPM and 0.09 kg/s.

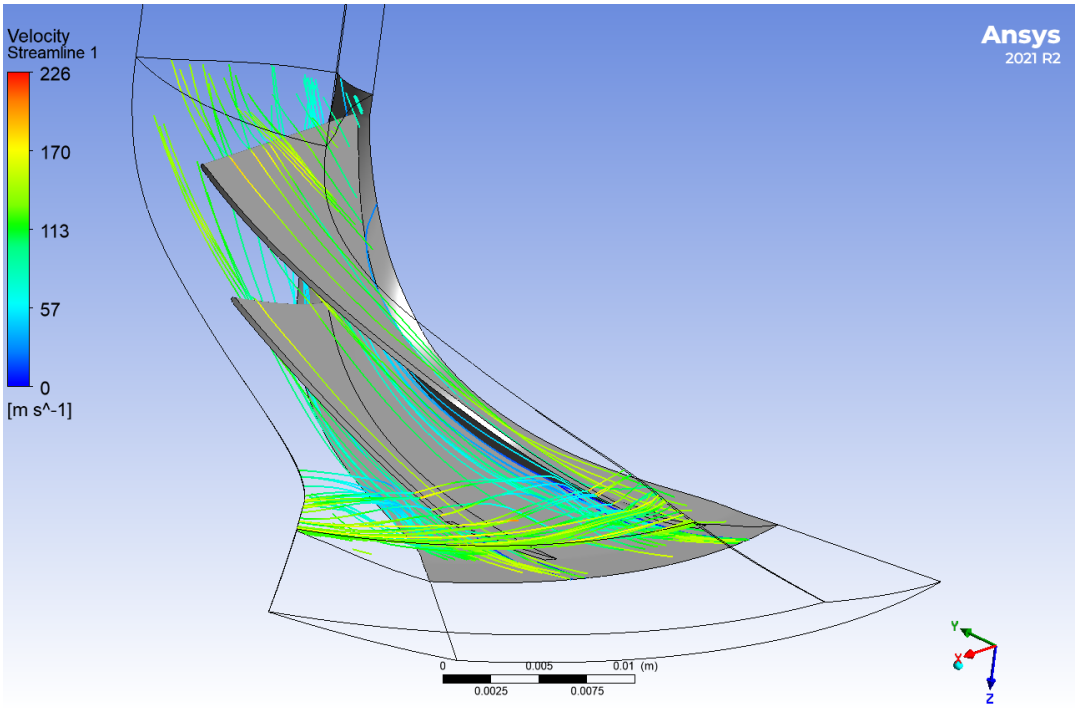

Figure C.28: Velocity streamlines through the blade passage of the IRIS compressor at 85,748 RPM and 0.114 kg/s.

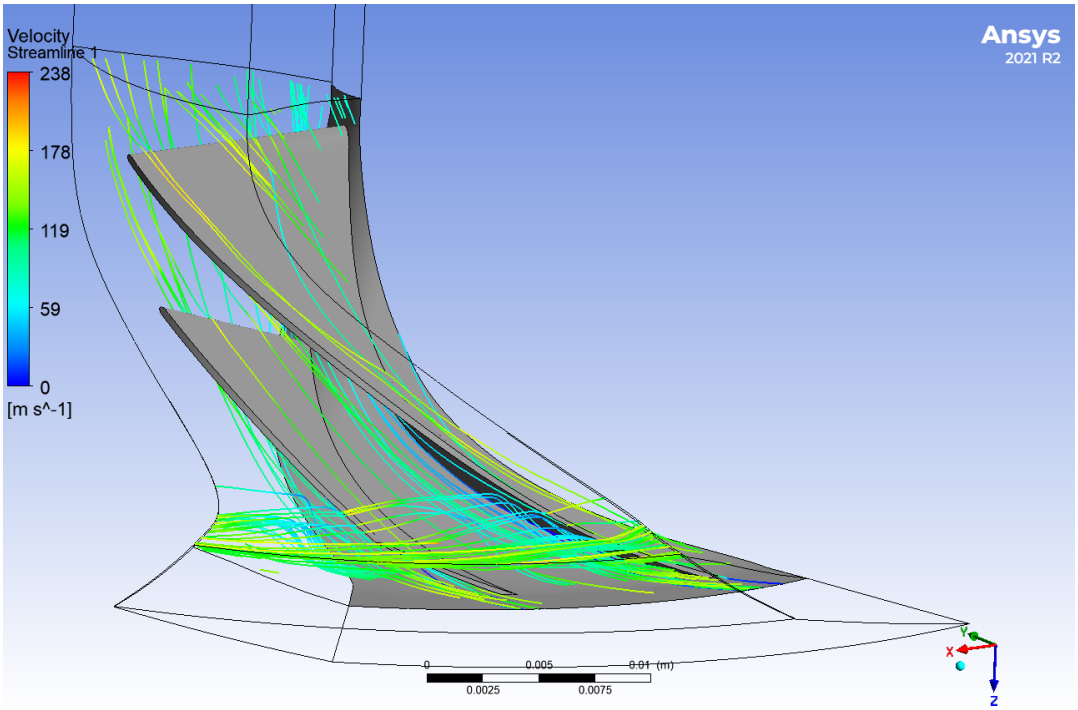

Figure C.29: Velocity streamlines through the blade passage of the IRIS compressor at 90,035 RPM and 0.12 kg/s.

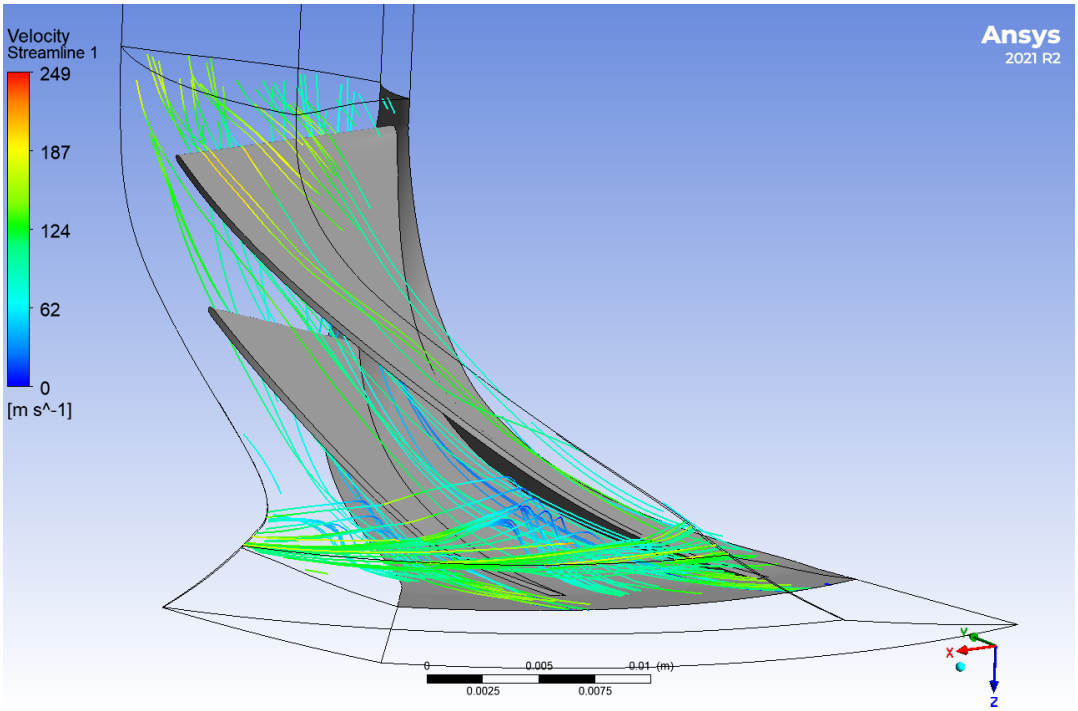

Figure C.30: Velocity streamlines through the blade passage of the IRIS compressor at 94,323 RPM and 0.11 kg/s.

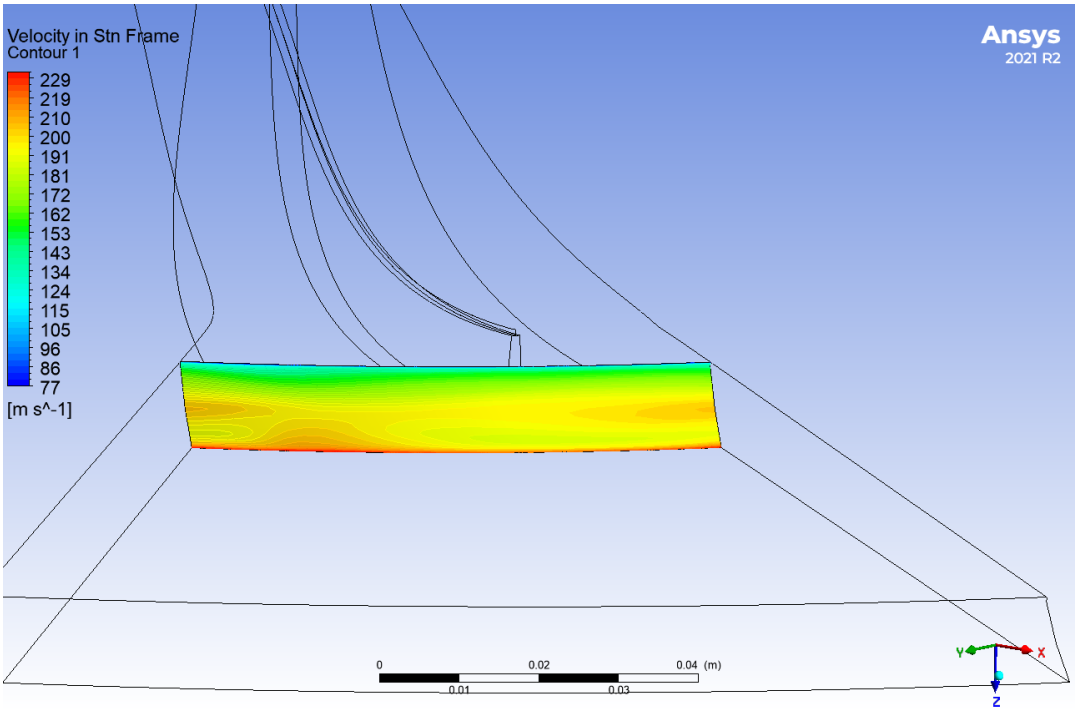

Figure C.31: Velocity contours at the impeller exit of the Radiver compressor at 21,406 RPM and 0.83 kg/s.

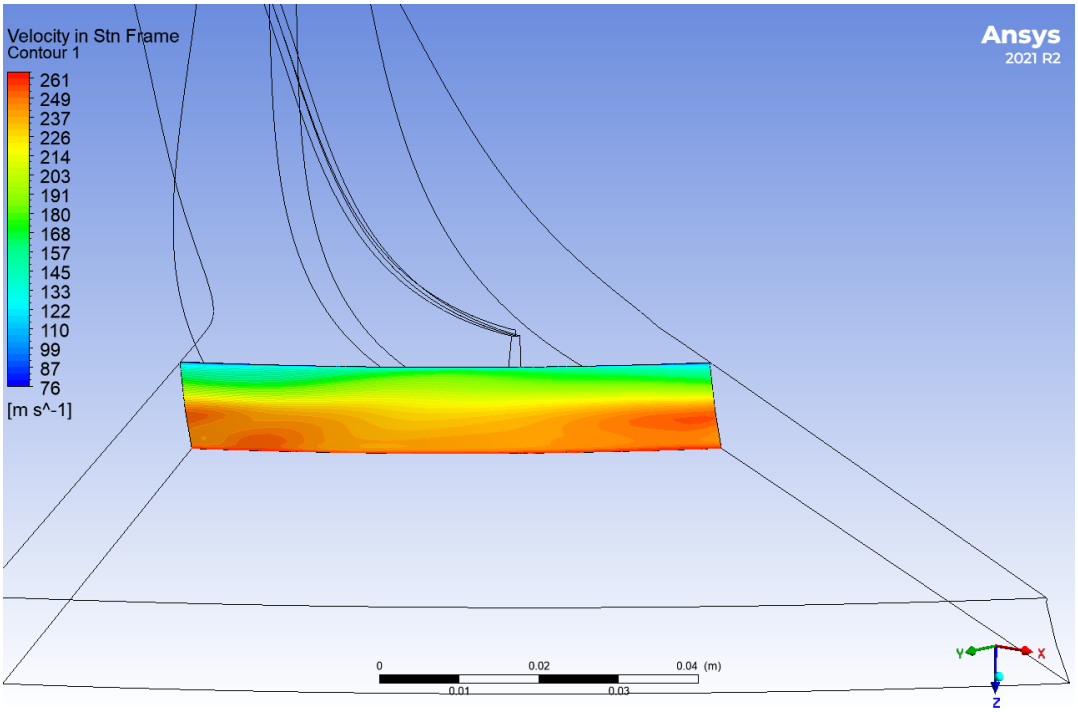

Figure C.32: Velocity contours at the impeller exit of the Radiver compressor at 24,973 RPM and 1.25 kg/s.

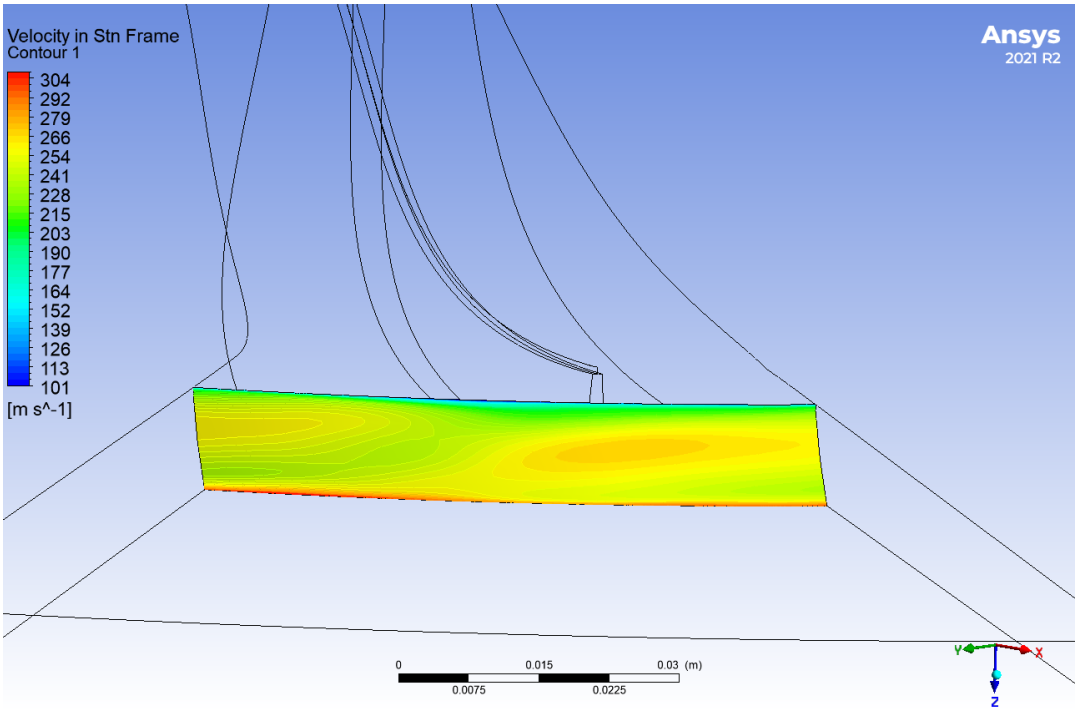

Figure C.33: Velocity contours at the impeller exit of the Radiver compressor at 28,541 RPM and 1 kg/s.

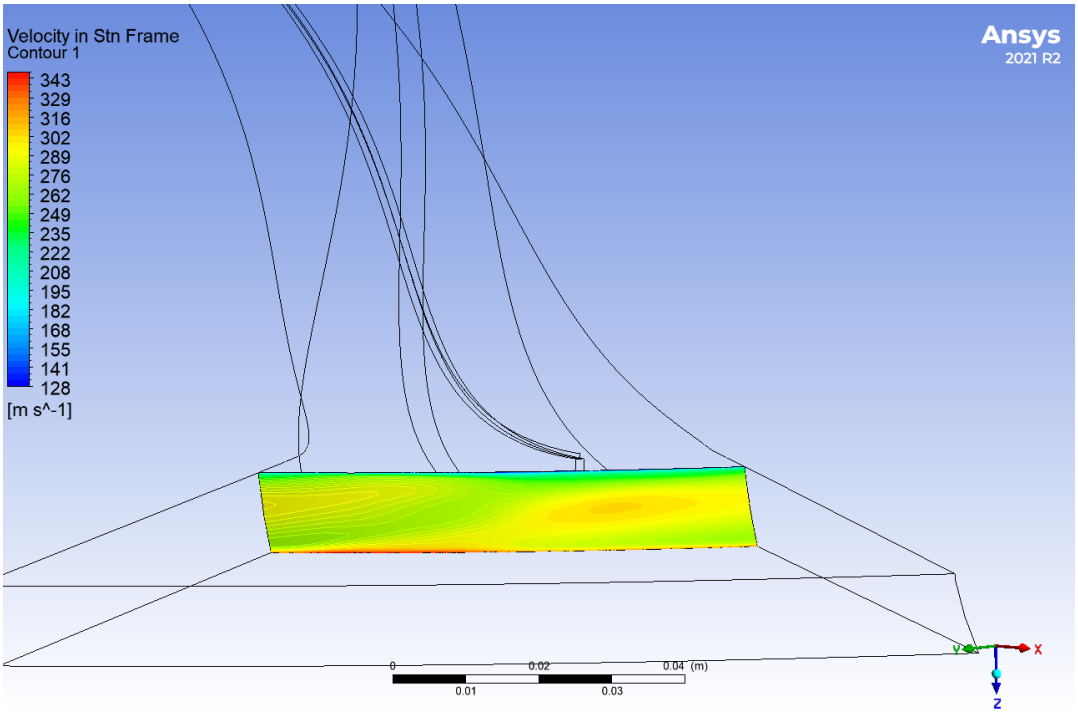

Figure C.34: Velocity contours at the impeller exit of the Radiver compressor at 32,108 RPM and 1.18 kg/s.

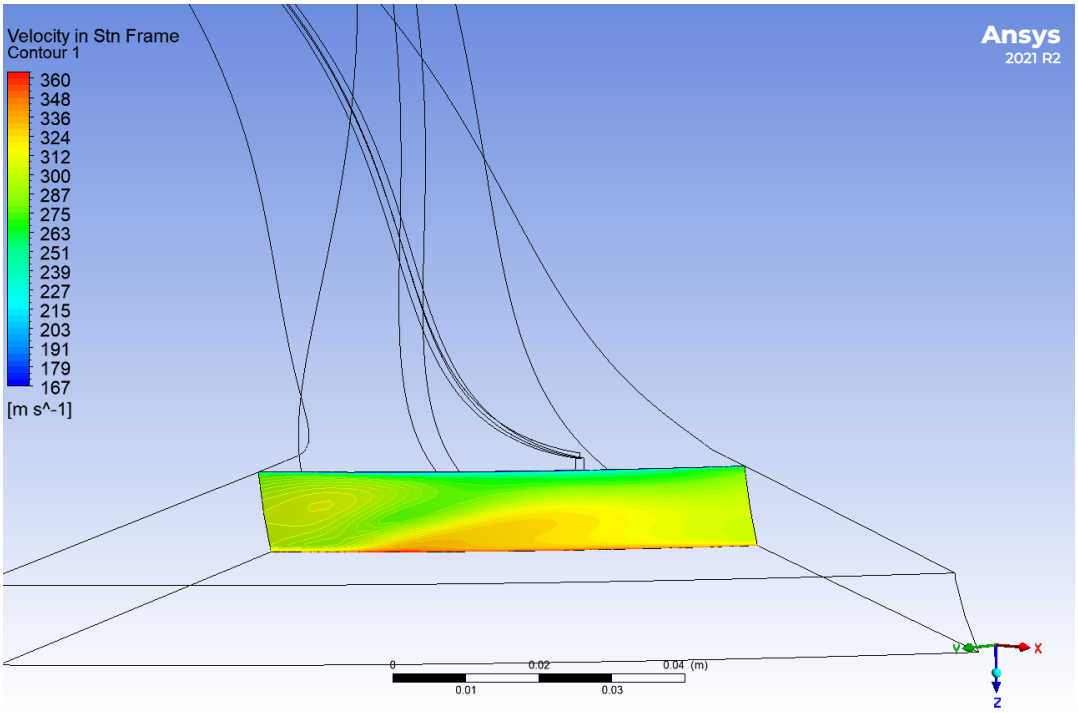

Figure C.35: Velocity contours at the impeller exit of the Radiver compressor at 35,676 RPM and 1.4 kg/s.

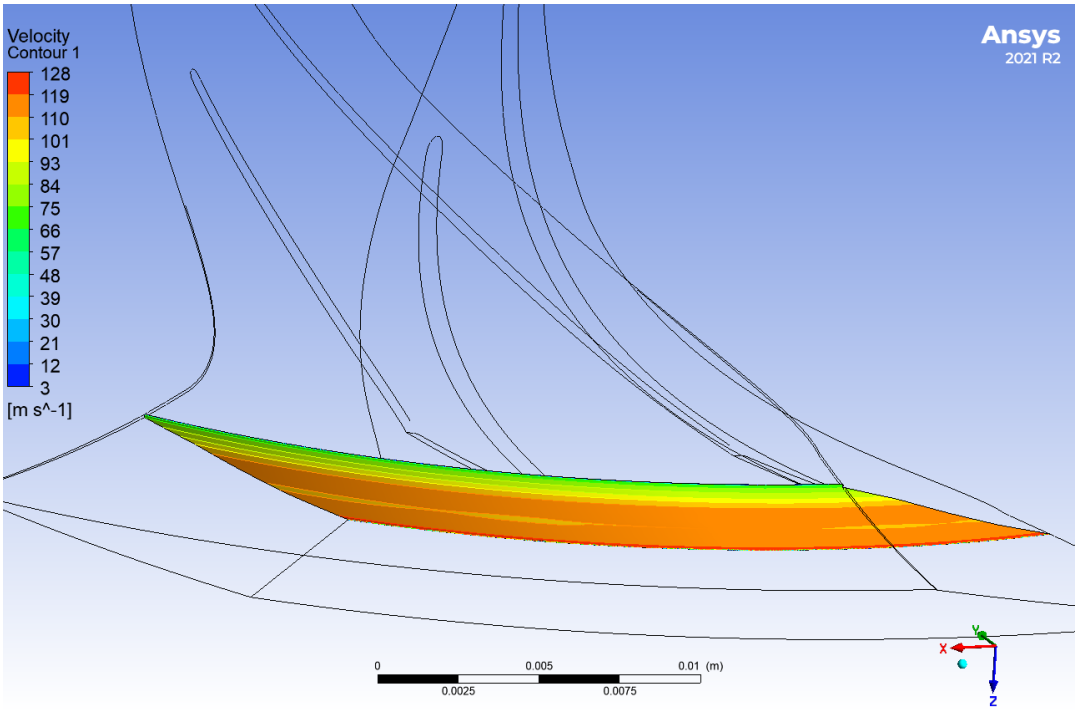

Figure C.36: Velocity contours at the impeller exit of the IRIS compressor at 68,598 RPM and 0.08 kg/s.

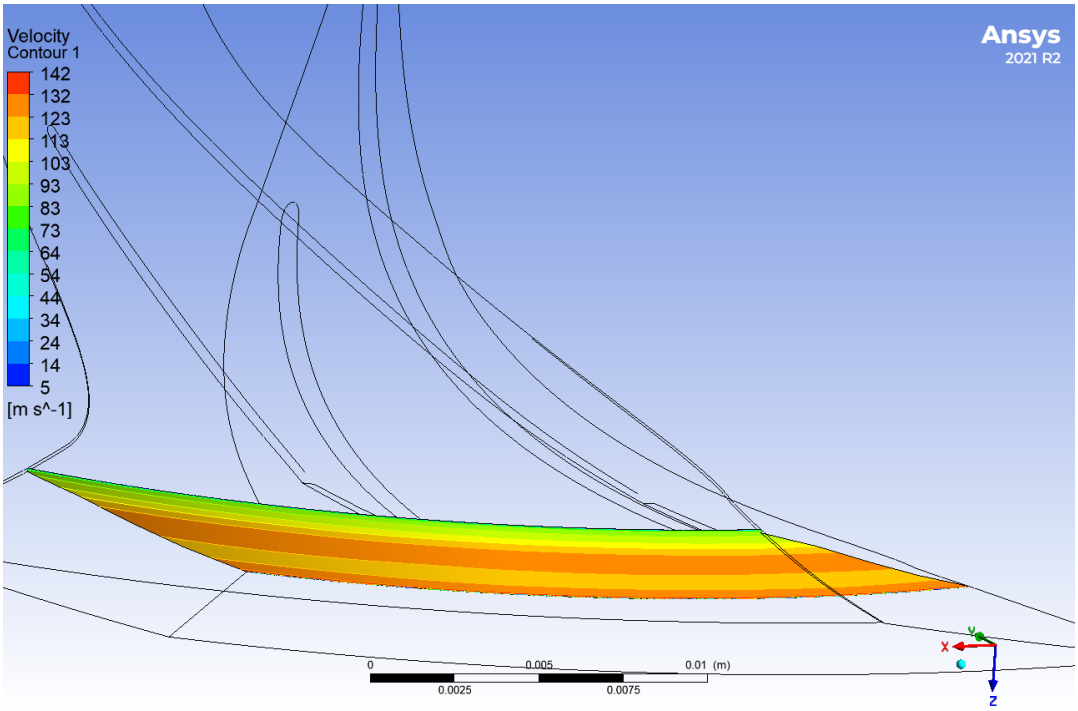

Figure C.37: Velocity contours at the impeller exit of the IRIS compressor at 77,173 RPM and 0.09 kg/s.

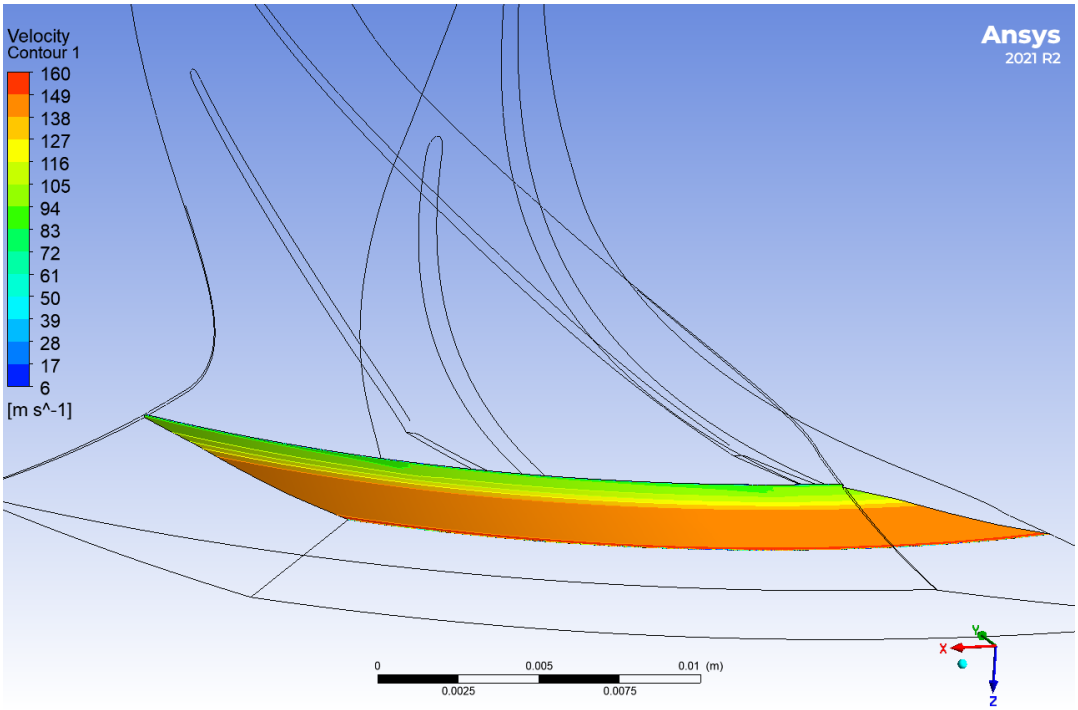

Figure C.38: Velocity contours at the impeller exit of the IRIS compressor at 85,748 RPM and 0.114 kg/s.

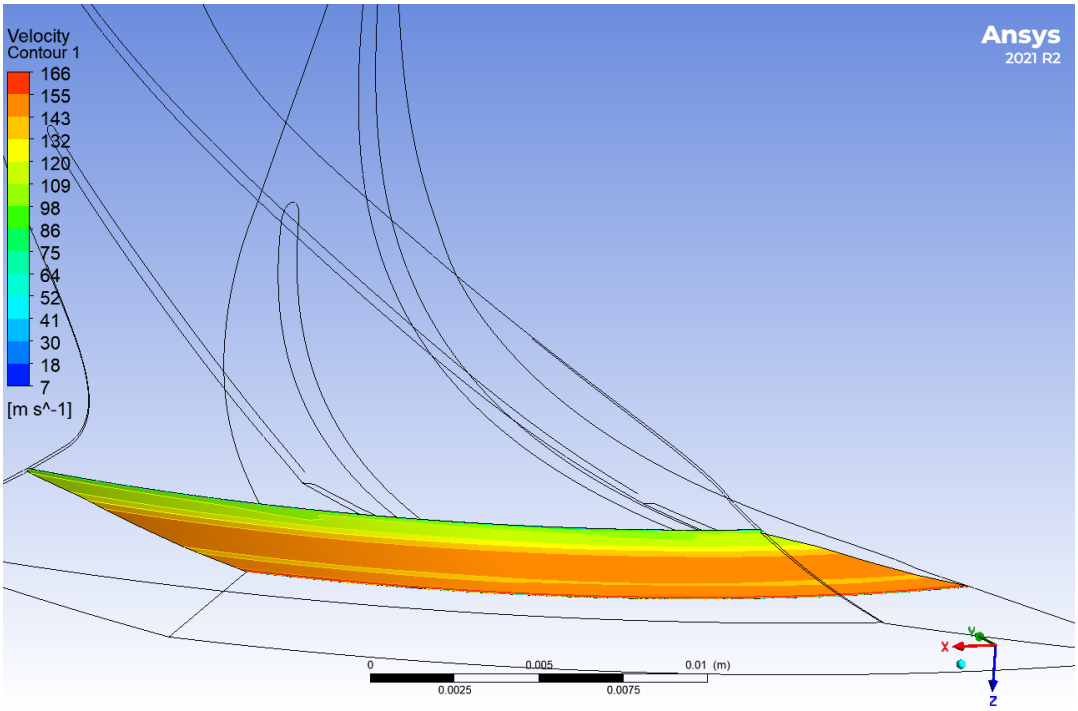

Figure C.39: Velocity contours at the impeller exit of the IRIS compressor at 90,035 RPM and 0.12 kg/s.

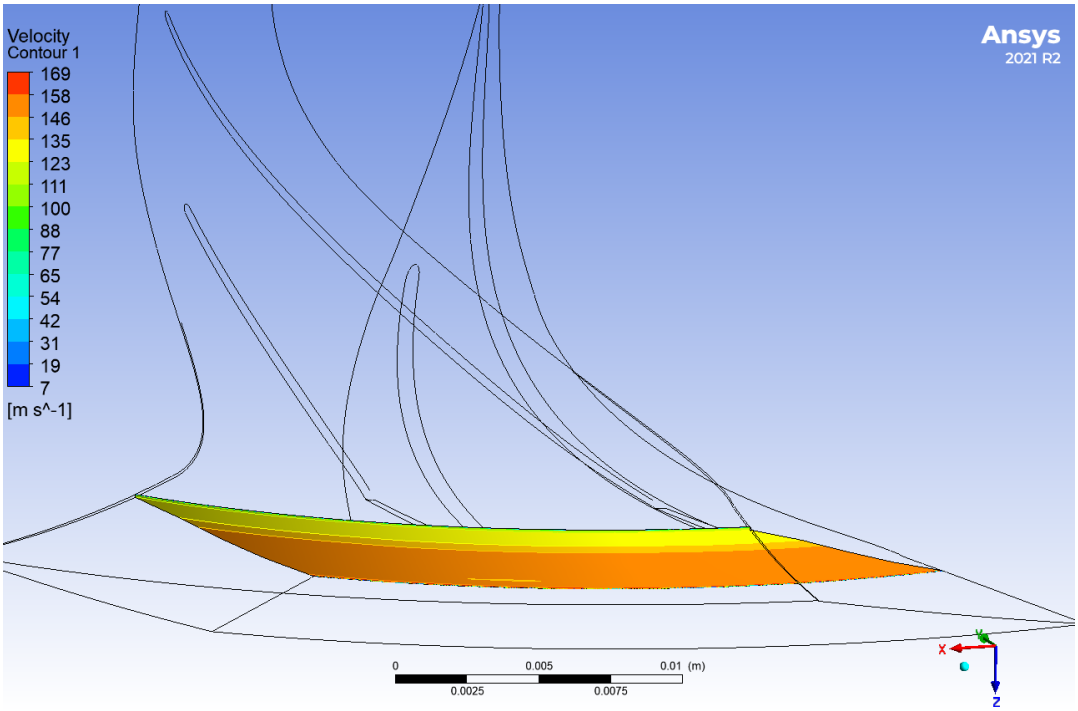

Figure C.40: Velocity contours at the impeller exit of the IRIS compressor at 94,323 RPM and 0.11 kg/s.

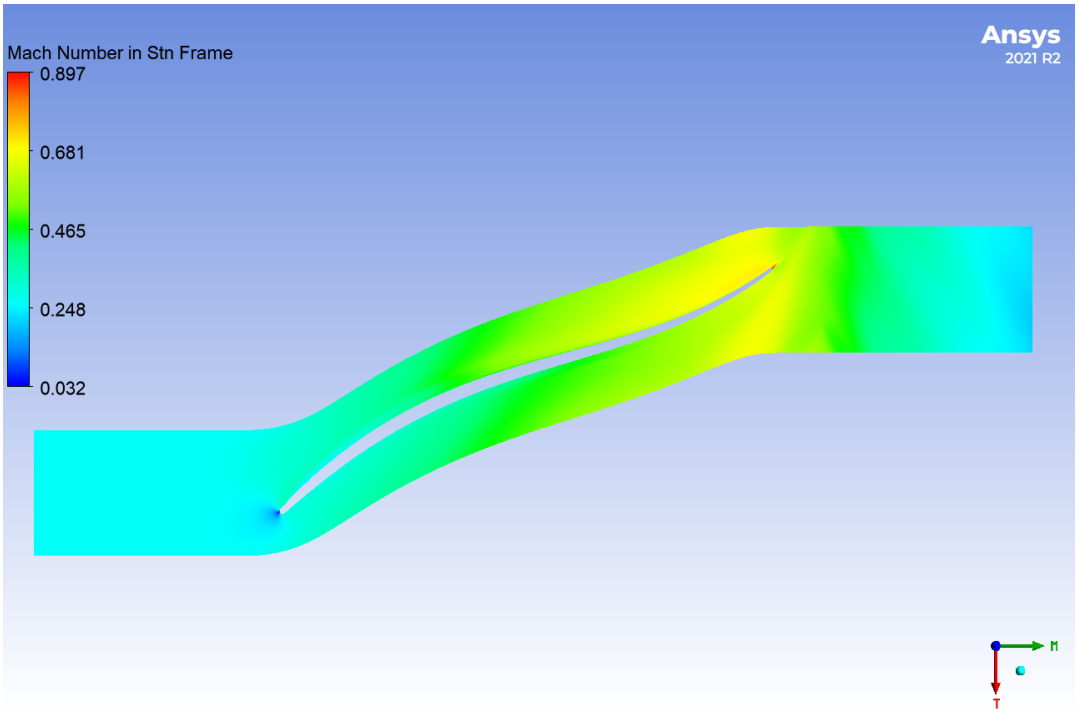

Figure C.41: Mach number distribution in the blade-to-blade plane at half-span for the Radiver compressor at 21,406 RPM and 0.83 kg/s.

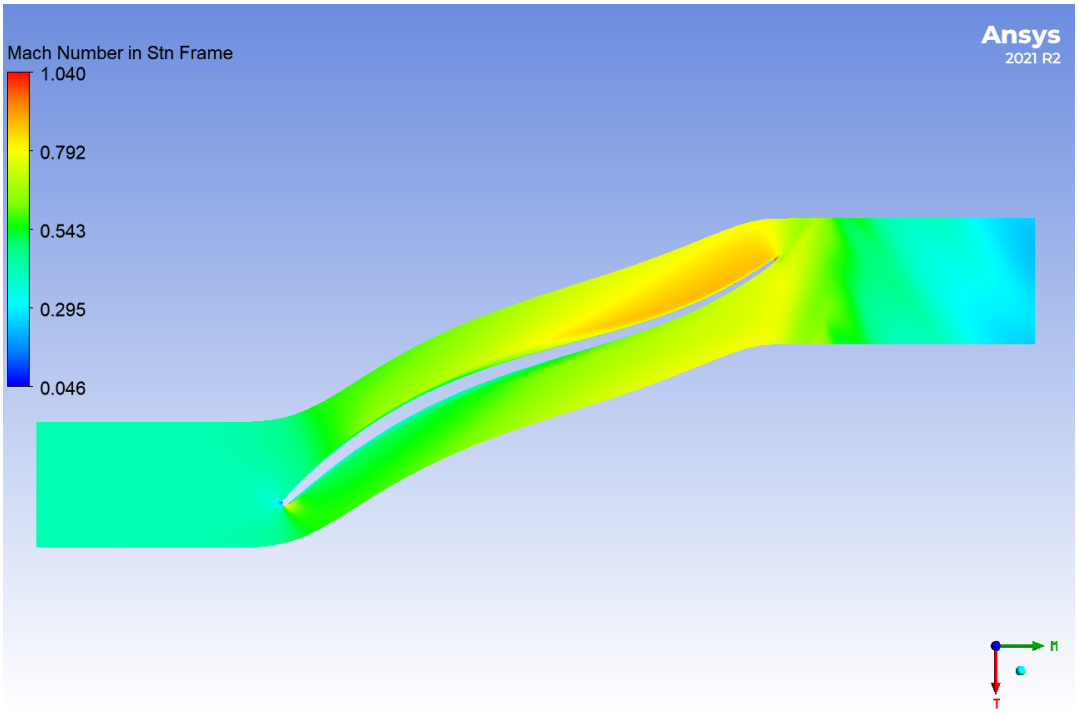

Figure C.42: Mach number distribution in the blade-to-blade plane at half-span for the Radiver compressor at 24,973 RPM and 1.25 kg/s.

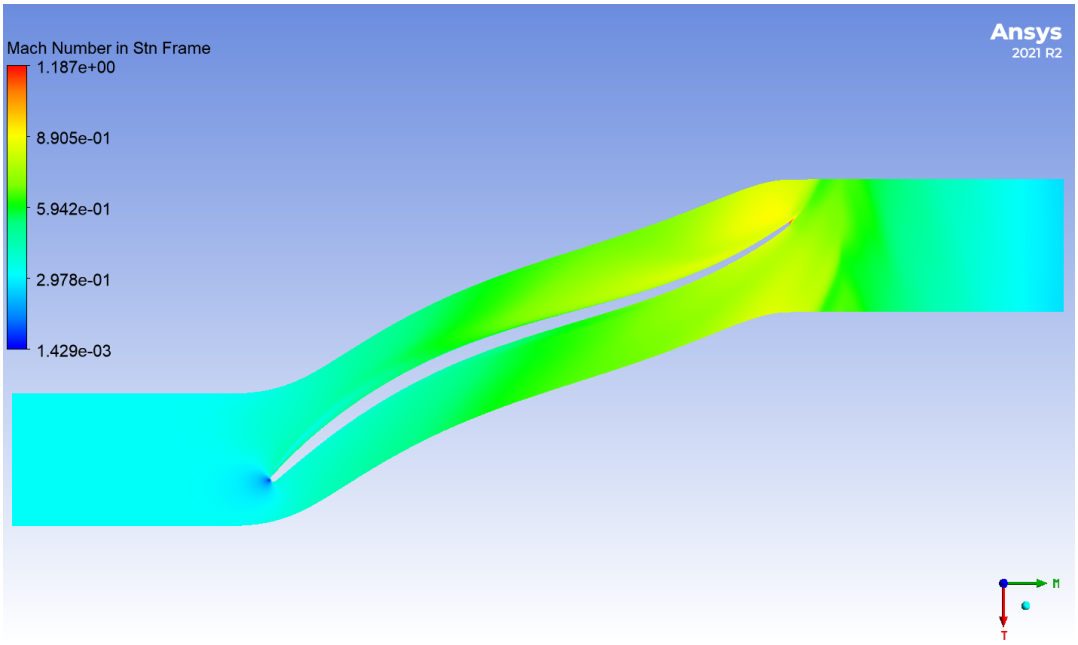

Figure C.43: Mach number distribution in the blade-to-blade plane at half-span for the Radiver compressor at 28,541 RPM and 1 kg/s.

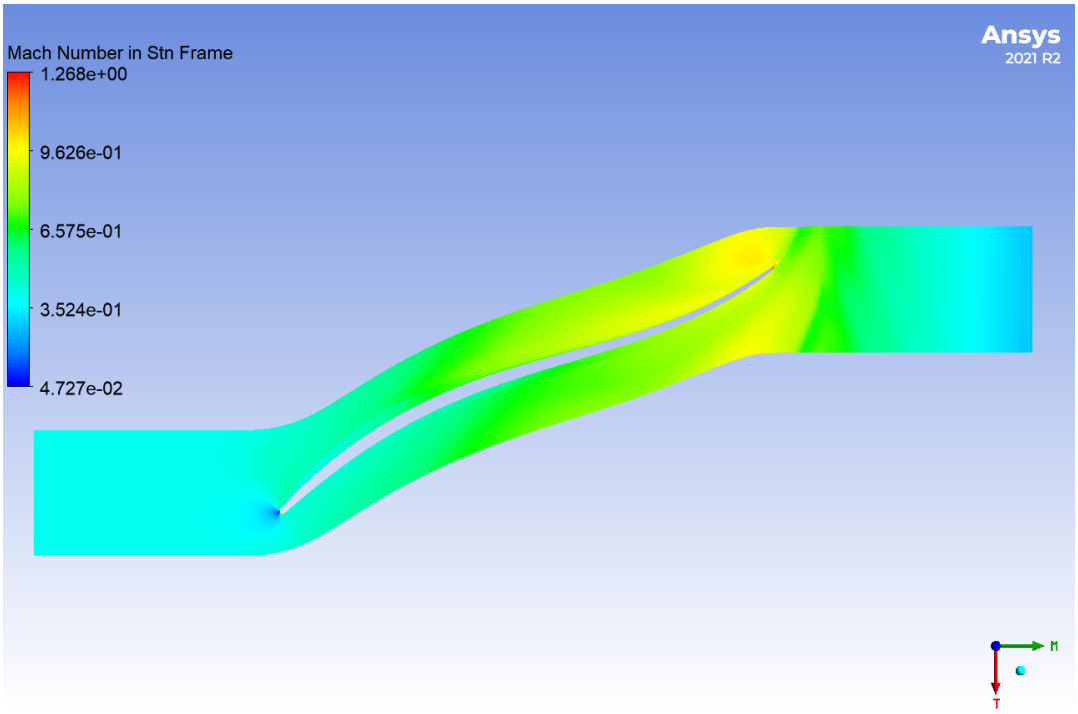

Figure C.44: Mach number distribution in the blade-to-blade plane at half-span for the Radiver compressor at 32,108 RPM and 1.18 kg/s.

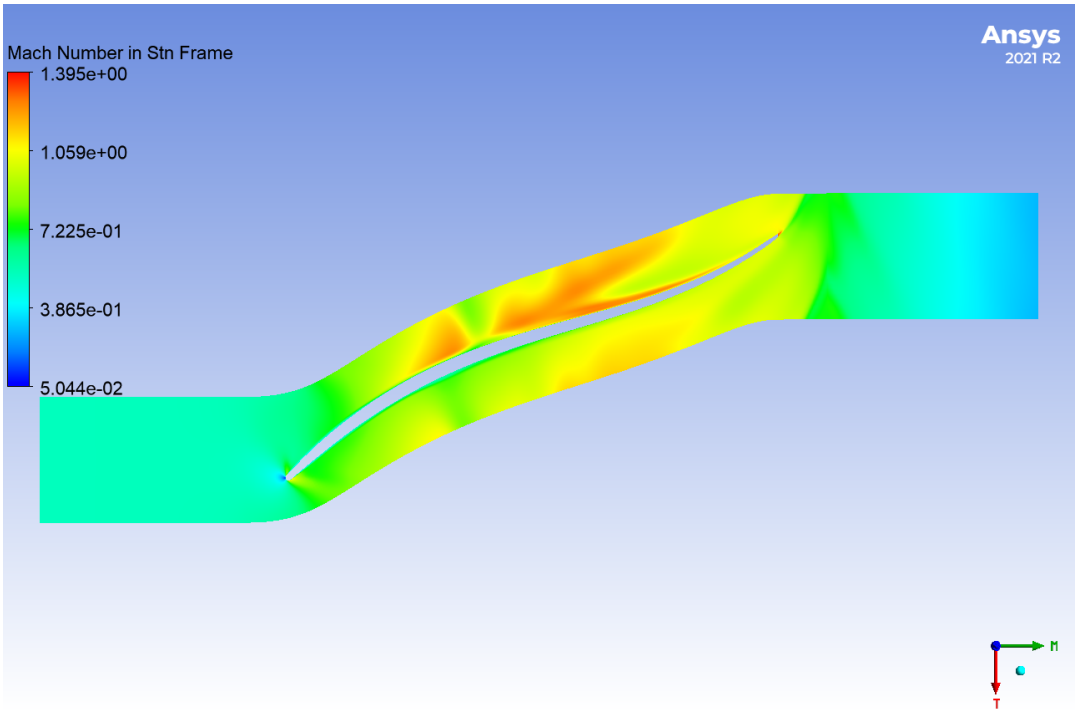

Figure C.45: Mach number distribution in the blade-to-blade plane at half-span for the Radiver compressor at 35,676 RPM and 1.4 kg/s.

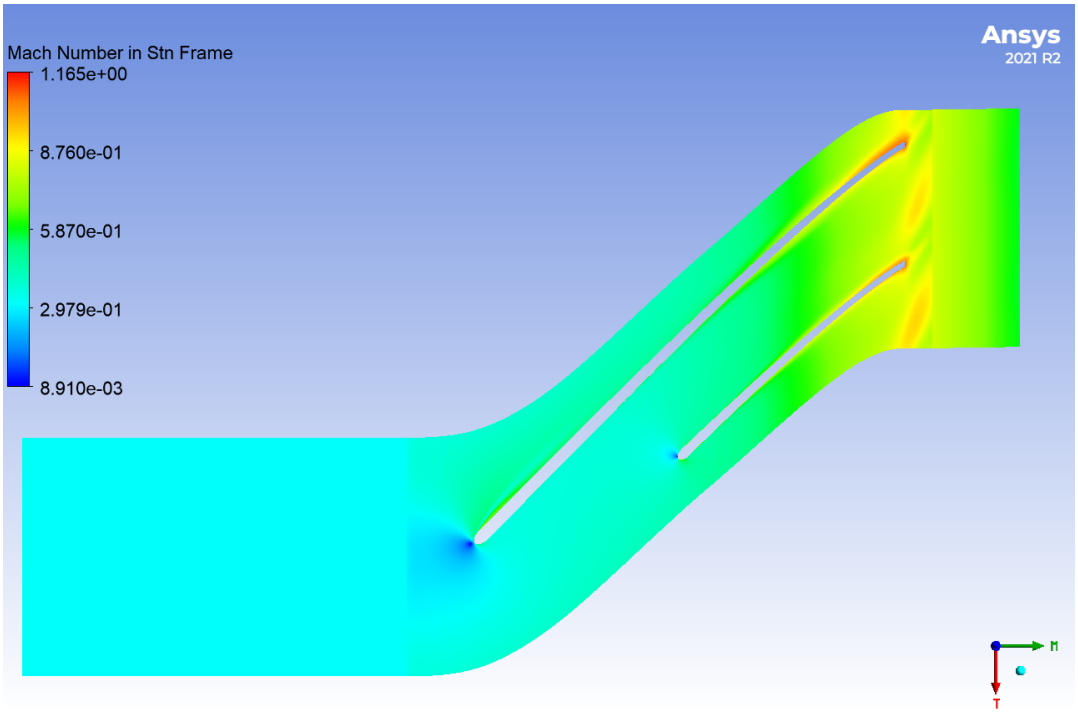

Figure C.46: Mach number distribution in the blade-to-blade plane at half-span for the IRIS compressor at 68,598 RPM and 0.08 kg/s.

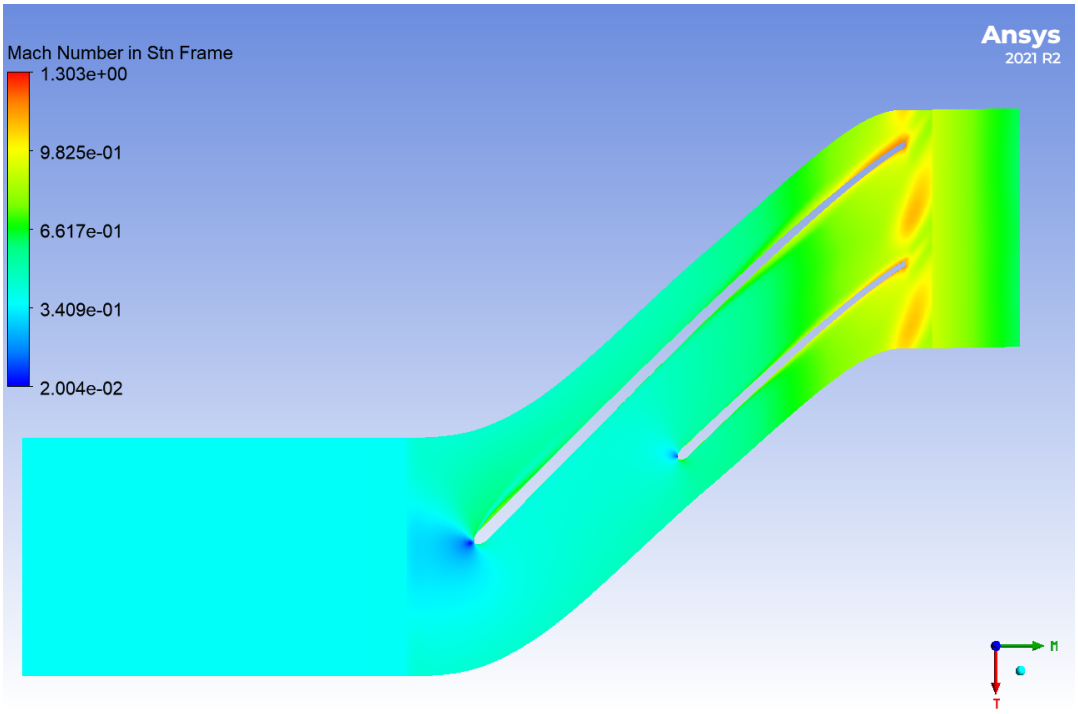

Figure C.47: Mach number distribution in the blade-to-blade plane at half-span for the IRIS compressor at 77,173 RPM and 0.09 kg/s.

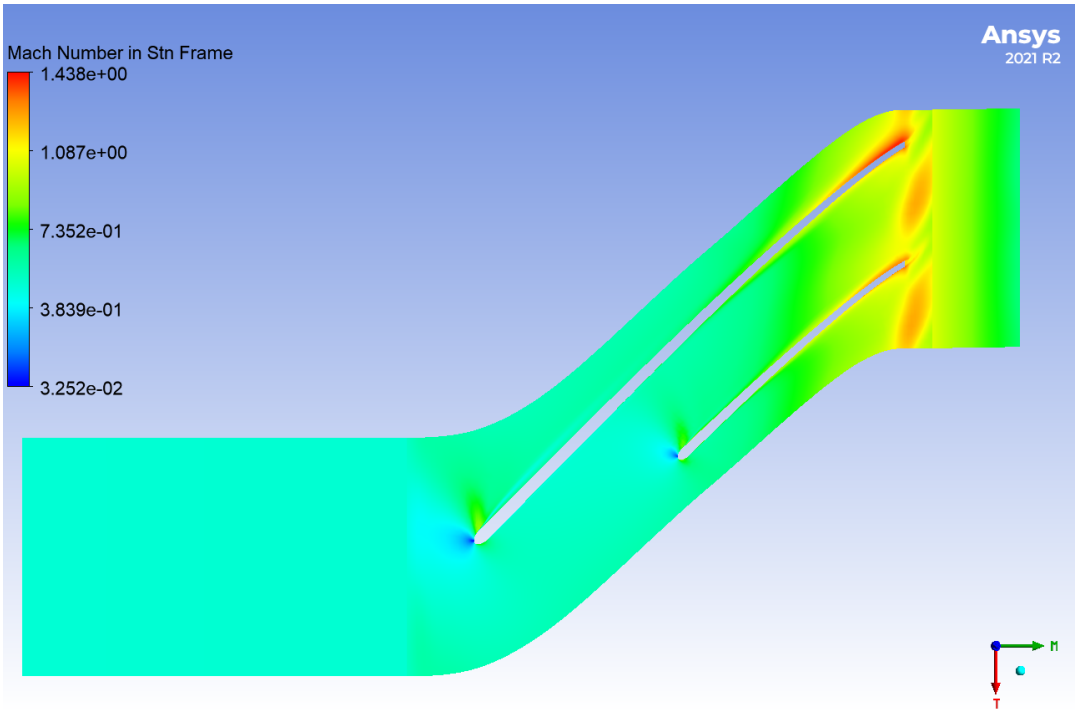

Figure C.48: Mach number distribution in the blade-to-blade plane at half-span for the IRIS compressor at 85,748 RPM and 0.114 kg/s.

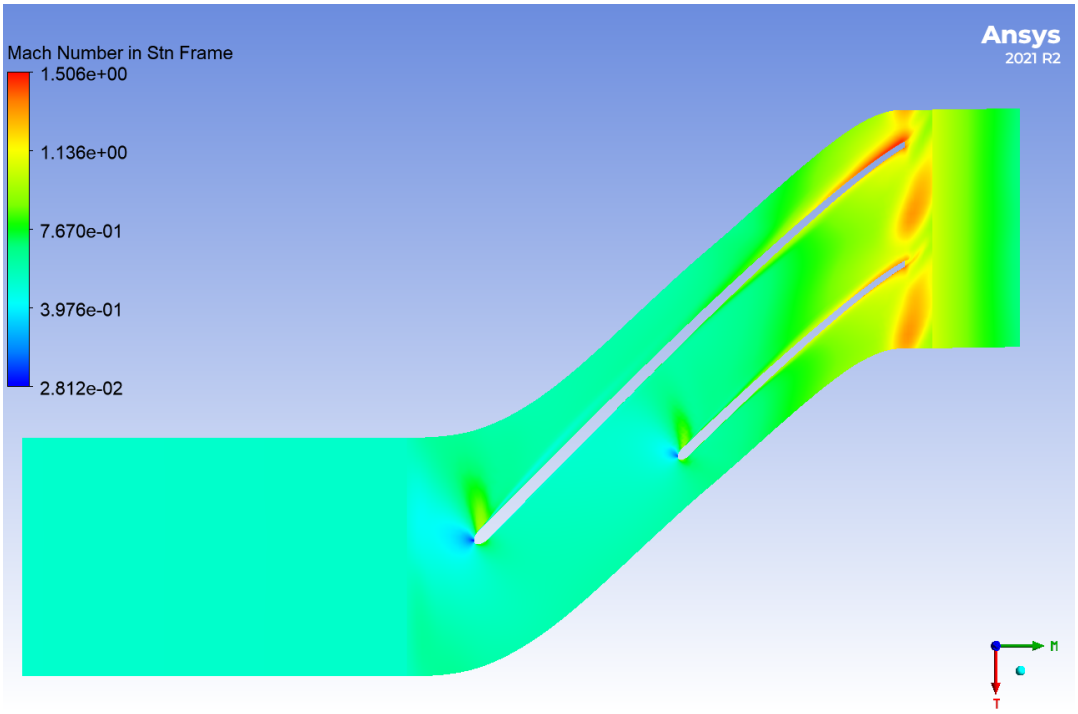

Figure C.49: Mach number distribution in the blade-to-blade plane at half-span for the IRIS compressor at 90,035 RPM and 0.12 kg/s.

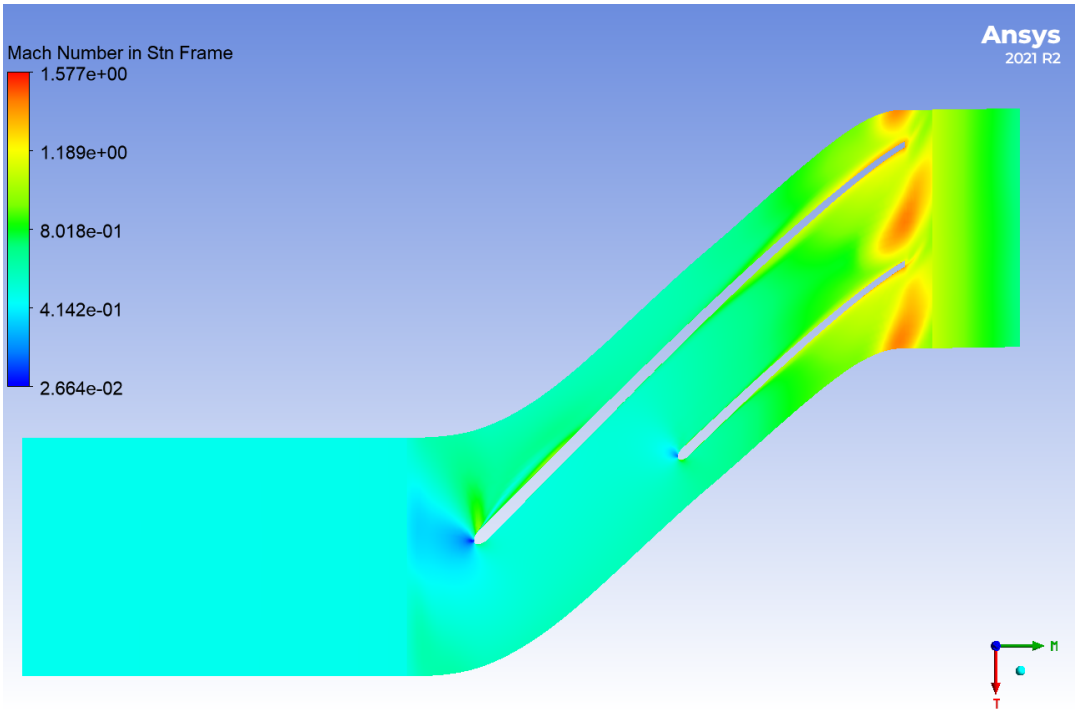

Figure C.50: Mach number distribution in the blade-to-blade plane at half-span for the IRIS compressor at 94,323 RPM and 0.11 kg/s.